# X-ray snapshots of elements: instrumentation and application to inhomogeneous system and chemical diffusion

Wenyang Zhao

February 2020

# X-ray snapshots of elements: instrumentation and application to inhomogeneous system and chemical diffusion

Wenyang Zhao
Doctoral Program in Materials Science and Engineering

Submitted to the Graduate School of
Pure and Applied Sciences
in Partial Fulfillment of the Requirements
for the Degree of Doctor of Philosophy in
Engineering

at the
University of Tsukuba

## Abstract

The significance of chemical element analysis can never be overstated: Chemical elements constitute all ordinary matters in the world; the composition of chemical elements is the primary feature of materials; the spatial distribution is the major characteristic of inhomogeneous systems; the diffusion of chemical elements is related to the principle of chemical reactions and many physiology activities; the inhomogeneity at interfaces controls the functions of many heterostructure materials. Consequently, elemental imaging techniques with additional functions such as low limit of detection, temporal resolution, or interface sensitivity play indispensable roles in a wide range of fields.

The major work in this thesis is to develop such multi-functional X-ray elemental imaging techniques. All techniques apply the measurement scheme of full-field X-ray fluorescence imaging. The scheme utilizes a wide X-ray beam to illuminate a large field on the sample, an optical component to guide fluorescence X-rays, and a 2D detector to capture energy-dispersive X-ray fluorescence images. On this basis, three innovations make the techniques in this thesis different from other existing techniques. First, commercially-available visible-light camera sensors are utilized as 2D X-ray energy-dispersive detectors. In the measurement, visible-light cameras capture snapshots quickly in X-rays. Energy-dispersive X-ray images are obtained by accumulating thousands of snapshots and processing the snapshots with dedicated algorithms. This unique operation has greatly reduced the cost of instruments and made them available to most researchers, engineers, and industry workers. Second, other X-ray analysis methods are connected to the imaging techniques for an improved signal-to-background ratio in trace-element imaging or for the sensitivity to buried interfaces in nanolayers. Third, this thesis emphasizes the realtime observation of changing samples rather than stable samples. A corresponding multi-element X-ray movie imaging technique is established to visualize the process of chemical diffusion and it may explain the mechanism of chemical reactions. To sum up, in this thesis, X-ray element imaging techniques based on capturing and processing visible-light camera snapshots are developed. The instruments are constructed in a compact and low-cost way. Multiple functions are introduced for chemical diffusion, trace elements, buried interfaces in nanolayers. For these reasons, the X-ray imaging techniques in this thesis have a vast potential. They will be applied to a wide range of fields in materials science.

## Content


Abstract ........ I

Content ........ II

List of Figures ........ IV

List of Tables ........ VII

List of Equations ........ VIII

Chapter 1. Introduction ........ 1

Chapter 2. Instrumentation: Full-field X-ray fluorescence imaging with camera snapshots ........ 3

2.1. 2D energy-dispersive Detectors ........ 3

2.1.1. Visible-light sCMOS camera ........ 3

2.1.2. Conventional CCD camera ........ 8

2.2. X-ray optics for full-field XRF imaging ........ 11

2.2.1. Micro pinhole ........ 12

2.2.2. Collimator plate ........ 14

2.3. Spatial resolution and time resolution ........ 16

2.4. X-ray sources ........ 17

2.5. Other elemental imaging techniques ........ 18

Chapter 3. Trace-element imaging with a size-expanded polarized synchrotron beam ........ 19

3.1. Introduction ........ 19

3.2. Experiment ........ 19

3.3. Results ........ 21

3.4. Significance in antiscattering XRF analysis for large-area samples ........ 26

3.5. Extension to trace-element chemical-state imaging ........ 34

3.6. Summary ........ 36

Chapter 4. X-ray fluorescence movie imaging for visualizing chemical diffusion ........ 37

4.1. Gradual chemical diffusion in a chemical garden ........ 37

4.1.1. Introduction of chemical garden ........ 37

4.1.2. Experiment ........ 39

4.1.3. Results and discussion ........ 40

4.1.4. Conclusion ........ 44

4.2. Rapid growth of zinc dendrites in electrodeposition ........ 44

4.2.1. Introduction to dendrite growth in electrodeposition ........ 44

4.2.2. Experiment ........ 45

4.2.3. Results and discussion ........45
Chapter 5. X-ray standing wave imaging for visualizing interface inhomogeneity ........48
5.1. Introduction: From XSW analysis to XSW imaging ........48
5.2. Development of the XSW imaging technique ........49
5.2.1. Experiment ........49
5.2.2. Results and discussion ........50
5.2.3. Conclusion ........62
5.3. Potential application to Langmuir-Blodgett films ........62
6. Underground survey of high-Z elements by high-energy X-ray fluorescence analysis ........64
7. Summary ........67
References ........69
List of publications ........74
Acknowledgements ........75

## List of Figures


Figure 2-1. Flow chart of the overall procedures for processing snapshots from the sCMOS camera..........6

Figure 2-2. Photos and X-ray fluorescence spectra of a ceramic plate obtained by the same sCMOS camera. (a) is the photo of the ceramic plate's front side and (b) is its spectra. The photos and the XRF spectra are obtained by the same sCMOS camera. From Ref[1]..........7

Figure 2-3. Flow chart of imaging processing of CCD camera snapshots..........10

Figure 2-4. XRF spectra analysis with the CCD camera. (a) and (b) are the spectra of a pond sediment sample, measured by CCD and SDD, respectively. (c) shows that the CCD camera is able to identify low-concentration Mn in a steel alloy. From Ref[2]. ..........11

Figure 2-5. 20-μm spatial resolution obtained in pinhole XRF imaging. (a) shows the photo of the test target; the observation area is marked by the dashed square. (b) shows the acquired XRF spectra. The imaging results of Ca in the substrate and Cr in black patterns are shown in (c) and (d), respectively; the Cr bars with 20-μm separation are clearly distinguished. From Ref[2]..........13

Figure 2-6. Full-field XRF imaging of a commercial resolution target sample. (a) An optical photograph of the resolution target. The black rectangular patterns are chromium coatings. The XRF imaging area is enclosed by the circle and the scale bar is 500 μm. (b) Full-field XRF spectra accumulated for 6 h. (c) An XRF image Cr K$\alpha$ and K$\beta$. From Ref[33]. ..........13

Figure 2-7. Schematic illustration of the full-field XRF imaging setup with a collimator plate. From Ref[35]. ..........15

Figure 2-8. Chromium imaging with using the collimator plate and the CCD camera. The verified spatial resolution is 20 μm..........16

Figure 3-1. Schematic illustration of the experimental setup. The width of the primary x-ray beam was expanded from 2 mm ($He$) to ~39 mm ($Hi$) in the direction perpendicular to the polarization with using an asymmetric-cut crystal. The reflection lattice plane was Si(220). The miscut angle α was 18°. The Bragg diffraction angle $\theta_B$ was 19.79°. From Ref[46]..........21

Figure 3-2. Full-field XRF imaging of a gabbroic rock from Mount Tsukuba. (a) Sample photo. (b), (c), and (d) are images of calcium, iron, and scattering x-rays, respectively. Every image has 1024 × 1024 pixels. (e), (f), (g), and (h) are the XRF spectra of the entire viewing area, Region A, Region B, and Region C, respectively. The scattering peak at ~9.5 keV is nearly invisible in all linear-scale spectra. From Ref[46]. ...22

Figure 3-3. Laboratory XRF spectra of the gabbroic rock. The scattering intensity, calcium fluorescence intensity, and iron fluorescence intensity are on the same order of magnitude. From Ref[46]. ..........23

Figure 3-4. X-ray fluorescence spectra of lithium borate pellet that includes 100 ppm chromium, iron, cobalt, and copper. (a) measured in synchrotron polarized experiment, and (b) measured in laboratory unpolarized experiment. Details of spectra were enlarged and attached to right side. From Ref[35]. ..........24

Figure 3-5. X-ray fluorescence spectra of CRM, NIST 81a, glass sand. Original material was mixed into cellulose matrix at mass fraction of 30%. (a) measured in synchrotron polarized experiment, and (b) measured in laboratory unpolarized experiment. Details of spectra were enlarged and attached to right side. From Ref[35]. ..........24

Figure 3-6. X-ray fluorescence spectra of CRM, NIST 1515, apple leaves. Original material was mixed into cellulose matrix at mass fraction of 30%. (a) measured in synchrotron polarized experiment, and (b) measured in laboratory unpolarized experiment. Details of spectra were enlarged and attached to right side. From Ref[35]. ..........25

Figure 3-7. X-ray fluorescence of CRM JSAC 0615. (a) measured in synchrotron polarized experiment, and (b) measured in laboratory unpolarized experiment. Details of spectra are enlarged and attached on the right. From Ref[35]. ..........26

Figure 3-8. Calculation of parallel components in primary X-ray beam. Polarization is parallel to capillary axis of collimator plate. From Ref[35]. ....................28

Figure 3-9. Calculation of perpendicular components in primary X-ray beam. Polarization is perpendicular to capillary axis of collimator plate. From Ref[35]. ....................30

Figure 3-10. Average scattering cross section $\sigma_{scat}$ with respect to DOP of primary X-rays and ratio of capillary radius $r$ to collimator plate thickness $t$. Scattering cross section is in units of $r_e^2$, where $r_e$ denotes classical electron radius and equals $2.82 \times 10^{-5}$ Å, and is normalized by effective solid angle $\Omega$ of capillaries. From Ref[35]. ....................32

Figure 3-11. Simulated XRF spectra. Sample was cellulose pellet that included 100 ppm iron. Model for (a) resembles laboratory unpolarized experiment in this work, and model for (b) resembles synchrotron polarized experiment. For ease of comparison, primary X-ray energy in two models was set the same at 9.53 keV, and detector sensor thickness was set the same at 500 µm. (c) summarizes ratio of scattering intensity to iron K-line intensity in all spectra. Spectra in (a) are labeled as DOP = 0. From Ref[35]. ....................33

Figure 3-12. (a) Photo of the gabbroic rock sample. (b) Black-and-white XRF image. It is connected from 141 thin strips. (c) and (d) are XAFS imaging scan of Strip I and II, respectively. (e), (f), and (g) are XAFS spectra of Region A, B, and C, respectively. From Ref[46]. ....................35

Figure 4-1. Schematic illustration of the Hele-Shaw cell and the XRF instruments. The dimension of the cell is 3 mm (H) × 1.5 mm (V) × 0.5 mm (thickness). From Ref[74]. ....................39

Figure 4-2. Optical microscopy photo of the final chemical garden structure after 15 hours reaction. The scale bar is 1 mm. The red dashed rectangle indicates the observation area of XRF movie, which is approximately 7 mm (H) × 4 mm (V). Region A indicates a typical tubular structure of white color and Region B indicates a typical structure of green color. From Ref[74]. ....................40

Figure 4-3. Tubular growth of in a similar chemical garden experiment, recorded by an optical microscopy ....................40

Figure 4-4. Full-field XRF spectra of the chemical garden. The XRF signals are accumulated in the whole 15 hours reaction. Spectra peaks of Ca and Fe can be identified. From Ref[74]. ....................41

Figure 4-6. Sequential time-resolved localized XRF spectra at Region C (a) and Region D (b) ....................43

Figure 4-7. XRF intensity change of Fe (a) and Ca (b) at two different regions. ....................43

Figure 4-8. Sequential movie frames of iron at the rapid tubular growth stage. From Ref[74]. ....................44

Figure 4-9. Schematic illustration of the experimental setup. From Ref[33] ....................45

Figure 4-10. XRF movie of zinc dendrites growth during electro-deposition. (a) Full-field XRF spectra. (b) Some key frames of the movie. The time resolution is 2 minutes. From Ref[33]. ....................46

Figure 5-1. (a) Conventional XSW analysis. It measures the full-field XRF intensity profile $Y(\theta)$ and analyzes the average depth distribution $\rho(z)$ of the impurity over the entire probing area. (b) XSW imaging technique. It measures $Y_{x,y}(\theta)$ independently at every $(x, y)$ point and reveals their respective impurity depth distribution $\rho_{x,y}(z)$. From Ref[104]. ....................49

Figure 5-2. XRR pattern of the nickel/carbon periodic multilayer. From Ref[104]. ....................52

Figure 5-3. Examples of the XSW imaging experiment data. (a) Full-field XRF spectra measured over the entire probing area. (b) An XRF image of Fe K$\alpha$ taken at $\Delta\theta = +0.02°$. From Ref[104]. ....................53

Figure 5-4. XRF intensity profile of Si K$\alpha,\beta$ from the silicon substrate. (a) Full-field profiles of the entire probing area, measured by either the Si-PIN detector or the pinhole-camera. The experimental profiles match well with the simulated profile whose vertical contrast has been reduced by half. (b) Micro-region profiles of C3, D4, E5, and F6, respectively. All of these micro-regions are along the diagonal of the image. From Ref[104] ....................54

Figure 5-5. Intensity profiles of X-ray Compton scattering. (a) Full-field profiles of the entire probing area, measured by the Si-PIN detector and the pinhole-camera, respectively. (b) Micro-region profiles of C3, D4, E5, and F6, respectively. The micro regions are on the diagonal of the image. From Ref[104]. ......................55

Figure 5-6. XRF intensity profiles of Fe K$\alpha$ from the iron impurity. (a) Full-field profiles of the entire probing area, measured by either the Si-PIN detector or the pinhole-camera. The experimental profiles match well with the simulated profile when the depth of the iron impurity is assumed to be at the center of each nickel layer ($Z = 7$ Å) and the vertical contrast has been reduced to 20% of the simulated profile by some experimental background. (b) Micro-region profiles of C3, D4, E5, and F6, respectively. All of these micro-regions are along the diagonal of the image. From Ref[104]. ..........................................................................55

Figure 5-7. The Fe K$\alpha$ intensity profiles of all 64 micro regions. All profiles are displayed using the same ticks on the axes. The ticks are shown at the upper right corner. From Ref[104]. ..........................................56

Figure 5-8. Simulation of the iron impurity depth distribution and the corresponding Fe K$\alpha$ intensity profile. (a) Model of the iron impurity depth distribution. (b) Simulated profiles. The shape of the profiles changes greatly as the depth $Z$ of the iron impurity moves from 0 Å to 49 Å. From Ref[104]. ....................................57

Figure 5-9. Illustration of how to convert an XRF intensity profile into a feature vector. (a) The simulated profile corresponds to the model in which the depth of the iron impurity is at the center of every nickel layer ($Z = 7$ Å). In this case, $S1 < 0$ and $S3 > 0$. (b) The simulated profile corresponds to the model in which the depth of the impurity is at the center of every carbon layer ($Z = 32$ Å). In this case, $S1 > 0$ and $S3 < 0$. From Ref[104]. ......................................................................................................................................58

Figure 5-10. Feature map for Fe K$\alpha$ intensity profiles. (a) The feature points corresponding to all the simulated profiles. In the simulation model, the center of the iron impurity in the depth direction moves from $Z = 0$ Å to $Z = 49$ Å. (b) The two feature points corresponding to the full-field intensity profiles of the entire probing area, measured by the pinhole-camera and the Si-PIN detector, respectively. (c) The four feature points corresponding to the micro-region profiles of C3, D4, E5, and F6, respectively. From Ref[104]. .........59

Figure 5-11. The feature points which correspond to all 64 micro-region Fe K$\alpha$ intensity profiles. The edge color of each feature point indicates the corresponding micro region's position in the X-axis and its face color indicates the position in the Y-axis. From Ref[104]. ..............................................................................60

Figure 5-12. (a-d) Preparation of the cobalt stearate LB films. (e) Layer structure of the Y-type $CoSt_2$ LB films deposited on silicon substrate. (f) X-ray reflectivity (small-angle X-ray diffraction) pattern of the sample. Six Bragg diffraction peaks indicate a highly-ordered layer structure. The first Bragg diffraction angle $\theta_B$ is $0.84^{o}$. (g) Sample photo of the wafer-scale LB films. (h) Cobalt fluorescence intensity profile measured in an XSW experiment. The $\theta$ angle was scanned around $\theta_B$. ....................................................63

Figure 6-1. Conceptual figure of a self-driving high-energy XRF analyzer robot for underground gold survey ..........................................................................................................................................65

Figure 6-2. XRF spectra of the gold coin buried at 6 cm depth in Soil C....................................................66

Figure 6-3. XRF spectra of the gold coin buried at 10 cm in Soil C (a) and the corresponding CWT processing results (b). ..........................................................................................................................................66

## List of Tables

Table 2-1. Specifications of the sCMOS camera. From Ref[1]. ........................................................................7

Table 2-2. Specifications of the CCD camera. From Ref[2]. ..........................................................................11

Table 2-3. Comparison of synchrotron radiation and laboratory X-rays .....................................................17

Table 3-1. Layouts of the experiment setup. Layout A is typical for synchrotron XRF spectroscopy analysis. Layout B and C are two available but imperfect layouts for full-field XRF imaging. Layout D is perfect after expanding the original beam in the horizontal direction, which is perpendicular to polarization; a large illumination area and the minimum scattering background are simultaneously realized. From Ref[46]. ........20

Table 5-1. The layer structure of the nickel/carbon periodic multilayer. From Ref[104]. ................................52

Table 6.1. Maximum detectable depth of different soils. ............................................................................65

## List of Equations

(3-1) ....................21
(3-2a)....................27
(3-2b) ....................27
(3-3) ....................27
(3-4a)....................28
(3-4b) ....................28
(3-5a)....................28
(3-5b) ....................28
(3-5c)....................28
(3-6a)....................28
(3-6b) ....................28
(3-7a)....................28
(3-7a)....................29
(3-8) ....................29
(3-9a)....................29
(3-9b) ....................29
(3-10) ....................29
(3-11a)....................29
(3-11b) ....................29
(3-12a)....................29
(3-12b) ....................29
(3-13a)....................30
(3-13b) ....................30
(3-13c)....................30
(3-14a)....................30
(3-14b) ....................30
(3-15) ....................31
(3-16) ....................31
(3-17) ....................33
(3-18) ....................33
(5-1) ....................50
(5-2) ....................50
(5-3) ....................50

(5-4) ....................................................................................................................................51
(5-5) ....................................................................................................................................57
(5-6) ....................................................................................................................................58
(5-7) ....................................................................................................................................58

# Chapter 1. Introduction

History makes men wise. When one considers developing techniques for the future, it is better to review the history first. About 400 years ago, the first optical microscope was invented by Galileo Galilei. Later in 17th century, Anton van Leeuwenhoek found that certain shaped lenses could increase the size of images and then he polished and grinded glass lenses. His lenses allowed him, for the first time, to see microscopic animals, cells, and even bacteria. His observation played a vital role in the development of cell theory. In 1930s, the first electron microscope was developed by Max Knoll and Ernst Ruska. It could provide pictures of extremely small particles, with its extraordinary magnification and resolution. It has been used extensively to study the cellular ultrastructure such as endoplasmic reticulum, mitochondria, Golgi complex, and nuclear chromatin. Also, it was pivotal in helping identify the causative agents of infectious diseases such as virus, which earned Aaron Klug the 1982 Nobel Prize in Chemistry. In 1981, the first scanning tunneling microscope was invented by Gerd Binnig and Heinrich Rohrer, which enabled them to observe samples at the atomic level. This development earned them the 1986 Nobel Prize in Physics. In the same year, Binnig and his colleagues invented atomic force microscope, bringing a true era of nano research. Moreover, the recent improvement of Cryo-EM enabled people to determine the structure of proteins with a near-atomic resolution. In 2017, the Nobel Prize in Chemistry was awarded to Cryo-EM. From the history we can learn that characterization techniques made great contributions to enrich human's knowledge about the natural world. Meanwhile, the information of images always provided the strongest evidence and detailed descriptions of complicated structures.

In the field of materials science, the history tells us some other things. In general, raw materials in the natural world are inhomogeneous and impure. People collect them to prepare new materials mainly by segmentation, uniformation, and purification. In this way, people are able to obtain stable functional materials and to study the property of simple substances. At this stage, characterization technique and analysis rely on model abstraction and simplification, such as X-ray diffraction (XRD) and X-ray reflectivity (XRR). However, in these years, people start to prepare composite materials and quite inhomogeneous structures for designed properties and advanced performance. Then, the characterization techniques should be upgraded correspondingly. New advanced imaging techniques are needed to investigate the materials inhomogeneity, to emphasize some key functional regions such as surface and interfaces, and also, to capture the changing process of materials with a temporal resolution.

In this work, the study is about chemical elements. The significance of chemical element analysis cannot be overstated: The composition of chemical elements is the primary feature of materials; the spatial distribution is the major characteristics of inhomogeneous systems; the diffusion of chemical elements is related to the principle of chemical reactions and many physiology activities; the inhomogeneity at interfaces controls the functions of many heterostructure materials. Consequently, techniques of chemical element analysis play an indispensable role in a wide range of fields including materials science, biology, environmental science, metallurgical industry, semiconductor industry, and archaeology.

There exist many techniques of chemical element analysis, such as Auger electron spectroscopy (AES), atomic absorption spectroscopy (AAS), inductively coupled plasma mass spectroscopy (ICP-MS), second ion mass spectrometry (SIMS), X-ray photoelectron spectroscopy (XPS), etc. Among these techniques, X-ray fluorescence (XRF) is quite powerful and efficient. The technique uses X-rays as the probe and therefore it has the advantages in common with many other X-ray techniques: non-destructive, nonvacuum measurement, and penetration capability of a few to hundreds of microns. Meanwhile, the signals of measurement are fluorescence X-rays. They are generated directly from element atoms, thus additional labels or indicators are not needed. Also, the photon energy of fluorescence X-rays is characteristic to chemical elements, thus the identification of chemical elements is robust and accurate.

In addition to composition analysis, XRF imaging can reveal the spatial distribution of chemical elements. This is crucial for the understanding of inhomogeneous systems. So far, two schemes of imaging are available: point-by-point scanning-type imaging and full-field imaging. The former is much more popular. It scans a micro/nano X-ray beam point-by-point on the sample and records the spectroscopy information of every point. The micro/nano X-ray beam is generally focused with polycapillaries, zone plates, or X-ray reflection mirrors. The latter remains less popular. It utilizes a wide beam to illuminate a large field on the sample, an optical component to guide fluorescence X-rays, and a 2D X-ray energy-dispersive detector to capture XRF images. This imaging scheme was established in recent years. However, it is clearly quite promising for the future. As it adopts a stationary scheme of measurement and is free of point-by-point

microbeam positional scan, “scanning” or recording other parameters like primary X-ray energy, elapsed time, and incident angle during image acquisition becomes much easier. In this way, the elemental imaging can be endowed with additional sensitivities including chemical state of a specific element, temporal evolution, and surface/interface characterization. Therefore, it may inspire many new techniques for versatile applications in various material systems.

In recent years, full-field XRF imaging has been adopted to probing the element map in cultural heritage and biological samples. However, still it has not been widely applied. The reason could be the existence of many challenges. First, the technique requires a 2D energy-dispersive detector. At present, such detectors are highly expensive and not common, and only a few groups involved in cooperation can maintain one. Second, the technique requires appropriate X-ray optics to project X-ray images from the sample to the detector. Performance of such X-ray optical components should be tested. Third, to endow the technique with additional sensitivities like surface/interface characterization, related X-ray physics must be clarified. Most important, much effort is required to construct the bridge to connect the new techniques to practical scientific applications. In my doctoral study, I worked on solving these challenges. In Chapter 2, I will introduce the instruments for all the experiments. Competitive 2D X-ray energy-dispersive detectors based on commercially-available visible-light camera sensors were developed, and high-resolution XRF images were obtained using simple X-ray optical components. In Chapter 3, I will explain how we reduced scattering background in full-field XRF imaging scheme and adopted it to investigate trace elements. In Chapter 4, I will show the temporal resolution of the imaging technique with using two successful applications of XRF movie imaging. In Chapter 5, I will demonstrate how the imaging technique could be endowed with interface sensitivity for the study of impurities in periodic nanolayers. Furthermore, in Chapter 6, an additional chapter, I will discuss interesting applications of high-energy XRF analysis.

## Chapter 2. Instrumentation: Full-field X-ray fluorescence imaging with camera snapshots

*Portions of this chapter were adapted with permission from W. Zhao and K. Sakurai, Sci. Rep. 7, 45472 (2017)[1] Copyright (2017) by Nature Group, and W. Zhao and K. Sakurai, Rev. Sci. Instrum. 88, 063703 (2017)[2] Copyright (2017) by American Institute of Physics.*

### 2.1. 2D energy-dispersive Detectors

A two-dimensional energy-dispersive X-ray detector is essential for full-field XRF imaging. To obtain high-quality images, the detector should have large amounts of pixels to record the position of every X-ray photon. To distinguish the fluorescence X-rays emitted from different elements, the detector should be able to resolve the energy of detected X-ray photons. Nevertheless, for a long time, there are rare X-ray detectors being able to simultaneously satisfy these two requirements. Traditional energy-dispersive X-ray detectors are generally point detectors, such as silicon drift detector (SDD). These detectors have a high energy resolution, but they have no positional sensitivity. Sometimes the point X-ray energy-dispersive detectors are bound to an array for positional-sensitive XRF spectroscopy experiment. However, it cannot do imaging experiment due to the too large pixel size and too small pixel amount. On the other hand, there are also many pixel-type two dimensional X-ray detectors, such as Pilatus[3], Eiger[4], Mythen[5], Medipix[6] and CCD camera. These detectors can work well for X-ray imaging experiment. However, their ability of resolving X-ray photon energy to distinguish different elements are still under gradual development and optimization. These years, with the development of detector technique, some advanced two-dimensional X-ray energy-dispersive detectors have appeared[7–9]. Several advanced setups for full-field XRF imaging have been developed and applied. However, while only several groups involved in cooperation can use such setups, the high expense of these detectors has become a bottleneck for the generalization of the full-field XRF imaging technique. For this reason, we consider modifying commercially-available visible-light camera sensors. The advances include not only low cost but also a more reliable quality control due to the mass production for commercial use. Also, such visible-light camera sensors have a larger pixel amount, smaller pixel size, and competent energy resolution, making them competitive options for XRF imaging applications. To specify, in this work, we have established the methods of utilizing a visible-light sCMOS (scientific complementary metal oxide semiconductor) camera and a conventional CCD (charged-couple device) camera and as two-dimensional X-ray energy-dispersive detectors.

#### 2.1.1. Visible-light sCMOS camera

Generally, a visible-light digital camera is used for taking photos in visible light, however, it can have a new function to measure the photon energy of X-rays. The new function is based on the basic working principle of digital cameras. When a photon hits a pixel photodiode on the camera sensor chip, charges are generated. The amount of charges is proportional to the photon energy[10]. In the case of visible light, one photon can only generate one charge, therefore, a camera cannot distinguish the photon energy or the color of visible light. In the case of X-rays, one photon can generate thousands of charges as its photon energy is thousands of times higher than visible light. The quantity of charges is recorded in the form of pixel intensity and then the corresponding photon energy is implied. If the X-rays are fluorescent X-rays emitted from atoms, the corresponding elements can be identified by matching their characteristic fluorescence energy. In short, a visible-light digital camera can be applied to identify chemical elements.

In order to individually measure each photon's energy, the recorded photon events on one camera image should be dispersed sparsely to separate them. This special condition is generally named as single-photon-counting mode. It is a prerequisite when applying a camera to X-ray spectroscopy measurement. Single-photon-counting mode can be easily achieved by reducing the amount of X-ray photon events on each image. Related discussion dates back to at least the 1980s[11], and from then on it was applied to both special X-ray CCD cameras[7,12,13] and conventional CCD cameras[14–17]. Nevertheless, none of these CCD cameras are frequently considered as current ordinary visible-light digital cameras. On the other hand, these days CMOS cameras become more and more popular for both domestic appliances and scientific research. CMOS cameras are also used for X-ray imaging[18–21], however, they are rarely used in direct X-rays. Scintillator layers are always installed in front of the image sensor to convert X-rays to visible light. In this case, information on X-ray photon energy is frequently lost. In this work, we use a visible-light CMOS camera for direct X-ray measurement. The ordinary digital camera becomes able to measure X-ray energy-dispersive spectra when it is specially operated, and the camera images are properly processed.

In order to obtain high quality X-ray spectra, the adopted camera should be of high quality as well. In most cases, the larger the better for the camera's dynamic range and the readout noise should be as small as possible. In this work, we use a commercially-available scientific CMOS (sCMOS) camera[22]. Its analog to digital (A/D) conversion is 16 bits. It is named as "scientific" because it is suitable for scientific research because of its high quality and reliable performance. As the camera is designed for taking photos in visible light, its front cover is made of transparent glass and an optical lens system is installed in front of the cover. As the transparent glass cover is 2 mm thick, X-rays cannot go through it. In order to fit out the camera for direct X-ray measurement, the lens system and the glass cover are removed to allow X-rays to pass, and an opaque front cover with an X-ray window is installed to avoid the influence of visible light.

In details, the camera used in this research is a PCO.edge 5.5 sCMOS camera from PCO AG. In order to apply the camera to direct X-ray measurement, the optical lens system in front of the camera is removed. The front cover is a 2-mm-thick visible-light transparent glass, and it is replaced with a 2-mm-thick aluminum alloy plate. On the plate, there is a circular aperture with a diameter of 4 mm. An X-ray window is pasted on the aperture. The X-ray window employed is commercially available 12 micron thick polymer film coated on both sides with 0.2 micron thick metallic aluminum (Ube Industries, Ltd.). To reduce the light leakage caused by small pinholes (unsuccessfully coated parts), we layered two (sometimes three) sheets of the film. The film is strong enough mechanically and stable. The aluminum coating blocks visible light but is almost transparent for X-rays. The replacement of the camera cover was done in a glove box filled with nitrogen gas to avoid the risk of oxidation or moisture. In the experiment, the function of B/W noise filter should be switched off to avoid artificial disturbance.

As stated earlier, the camera should work in single-photon-counting mode to measure X-ray energy-dispersive spectra. The amount of photon events on one camera image should be carefully controlled by adjusting the intensity of incident X-rays or adjusting the single exposure time. When the camera snapshots does not show any continuous pattern but only shows many discrete dots, the condition of single-photon-counting mode is thought to be achieved. The next step is to process the camera snapshots. Generally, the X-ray photon energy can be retrieved from the pixel intensities of the corresponding photon event on the snapshot, however, the retrieval process is not always straightforward. In this work, we propose an integrated-filtering method to ensure the retrieval process is effective and correct, then high quality XRF spectra can be readily obtained after processing the raw camera images.

The detailed procedures of retrieving X-ray energy-dispersive spectra from camera snapshots are as follows: Prior to the experiment, 100 dark images are acquired without any illumination of visible light or X-rays. It is found that the average intensity of an unilluminated pixel is approximately 100. In different images, the intensity of the same pixel may vibrate around 100 because of dark current. The frequency distribution of all pixel intensities in all the dark images shows a symmetric sharp peak at 100. The FHWM this background peak is 8, implying the level of dark current. An average background image is generated by averaging all the dark images. As the pixels on the sCMOS sensor are quite independent of each other, the exact average intensity of different pixels is not totally the same, hence the average background image should be subtracted from every experimental image to eliminate the fixed-pattern noise. The level of dark current is not influenced by external X-rays.

When the sCMOS camera receives X-rays and works in the single-photon-counting mode, discrete bright dots appear on the black background in the snapshots. The pixels in the black background are not influenced by X-ray photons, so their intensities are still around 100. The intensities of pixels in the bright dots are obviously higher than the background value of 100, generally from hundreds to thousands. In order not to count the large number of unilluminated pixels, only pixels whose intensity is larger than 200 are considered. After that, their intensities are respectively modified by subtracting the average background image.

As the bright pixels are always gathered in discrete bright dots, it is reasonable to infer that the pixels in one bright dot are illuminated by the same X-ray photon and one bright dot corresponds to one photon event. That is to say, the charges generated by an X-ray photon are shared by a group of neighboring pixels. This phenomenon of charge sharing is frequently seen in many CCD cameras as well[7,8,15,23]. Unlike a visible-light photon, an X-ray photon can generate a charge cloud of thousands of photoelectrons. The charge cloud has a certain size in the photodiode matrix of the image sensor, so that the charges will be collected by either a single pixel or some neighboring pixels. In previous reports on CCD cameras, there are both single-pixel photon events and multi-pixel photon events. The size of a multi-pixel photon event is

generally smaller than 3 ×3 pixels. Nevertheless, in this work with the present sCMOS camera, nearly all photon events are multi-pixel events. The size of a multi-pixel event generally exceeds the region of 3 × 3 pixels. These differences are probably due to different pixel sizes and anatomies of the CCD sensor and sCMOS sensor. The minimum CCD pixel size in previous related works is 13 μm × 13 μm[8], and it is only 6.5 μm × 6.5 μm in this sCMOS camera. Consequently, it is reasonable that more pixels are needed to collect one charge cloud.

A threshold of 200 is proposed to pick out photon events from the image background. It has been found that the pixel intensities in dark images can hardly exceed 200. Based on the study of the 100 dark images, the probability is about 0.005%. Consequently, if the intensity of a pixel is higher than 200 in an X-ray image, a photon event can be recognized at this position. The next step is to collect all signal pixels of this photon event. All pixels in the region of 5 × 5 pixels are taken into consideration. The center of the 5 × 5 region should be the pixel whose intensity is the maximum in the photon event. It is recognized as the impinging position of the X-ray photon. After subtracting the average background image, the intensities of all 25 pixels are integrated.

However, even after integration, a problem of incomplete charge collection still exists. As the sCMOS camera is designed for visible light, its depletion region of photodiodes is not thick enough to fully absorb all high energy X-ray photons. Some X-ray photons may penetrate the depletion region and be absorbed in field-free regions below. The charges generated in the field-free regions diffuse rapidly. Some of the charges can still be collected if they spread to the depletion region, whereas the rest of the charges are lost. As a result, the integrated intensity of a photon event may still underestimate the true X-ray photon energy. There have been some similar discussions on thin-depletion-region CCD cameras. The same discussions can be generalized to sCMOS cameras because the principle of charge collection is not very different.

A threshold is mandatory to distinguish and remove all incomplete-charge-collection photon events. If an X-ray photon is absorbed in the depletion region, the generated charges will be quickly collected with no loss. In this case, the size of the charge cloud should not be too large, and the center pixel should collect many more charges than other pixels. In contrast, if the X-ray photon is absorbed in field-free regions, the charge cloud diffuses rapidly, and then only a portion of the charges can be collected. In this case, the ratio of charges collected by the center pixel to all collected charges cannot be distinctly high. For this reason, the center-to-integrated ratio can serve as an indicator to identify incomplete-charge-collection photon events. In the final, a filtering criteria of [40%, 50%] for the center-to-integrated ratio is determined. Only when the center-to-integrated ratio of one photon event is within [40%, 50%] can it be counted as a valid signal. This filtering criteria may reject 90% of photon events. However, the remained photon events can make a high quality XRF spectra.

Figure 2-1 summarizes the flow chart of the overall integrated-filtering method for processing camera snapshots in X-rays. All pixels in camera images except those in borders are examined by this flow charge to retrieve the X-ray energy-dispersive spectra and also X-ray color images. We have coded the integrated-filtering method in the camera controlling software, therefore the X-ray spectra can be output immediately after measurement.

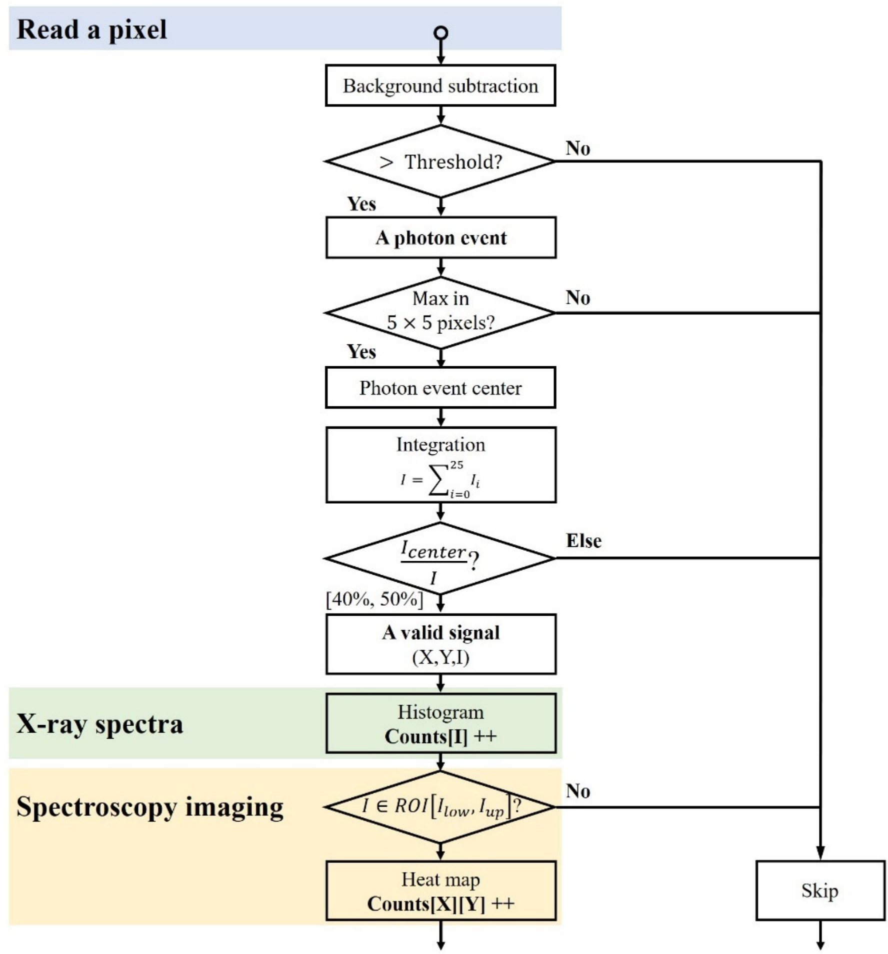


Figure 2-1. Flow chart of the overall procedures for processing snapshots from the sCMOS camera.

The energy resolution of the sCMOS camera is determined as 220 eV at 5900 eV by measuring the full-width-at-half-maximum (FWHM) of the manganese K$\alpha$ peak. Therefore, the present visible-light sCMOS camera can measure XRF spectra and analyze the composition of elements in the sample. For example, a ceramic plate which has a white base [Figure 2-2(c), back side] and blue patterns [Figure 2-2(a), front side] is tested. The two photos in Figure 2-2 (a) and (c) are taken by the sCMOS camera before removing the optical lens system and the transparent glass cover. The photos are monochrome as there is no color filter in the camera. After removing the lens system and replacing the glass cover with an X-ray window, the XRF spectra of the front side [Figure 2-2(b)] and back side [Figure 2-2(d)] are respectively measured by the same sCMOS camera. In the experiment, the primary X-ray beam is monochromatic Cu K$\alpha$ X-rays. The exposure time for one single image is 100 ms. The accumulation time is 30 minutes. In the spectra, every peak can be identified, thus the corresponding elements can be identified as well. It could be noted that the element composition of the front side and the back side are quite similar, whereas cobalt only appears in the front side, indicating the relations between cobalt and the blue color of the ceramic.

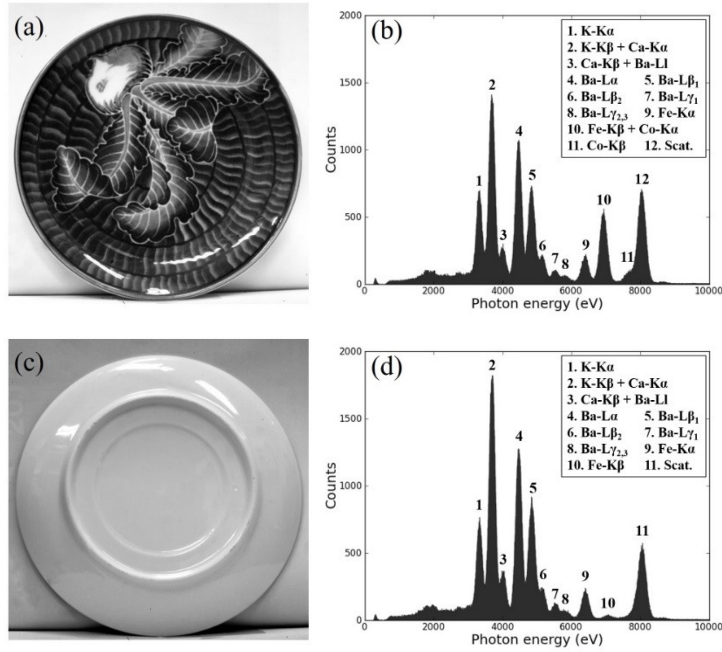


Figure 2-2. Photos and X-ray fluorescence spectra of a ceramic plate obtained by the same sCMOS camera. (a) is the photo of the ceramic plate's front side and (b) is its spectra. The photos and the XRF spectra are obtained by the same sCMOS camera. From Ref[1].

To sum up, a conventional, visible-light digital camera is developed for taking ordinary photos. As a kind of visible-light camera, an sCMOS camera is of very high quality so that it has been widely introduced in many areas of scientific research for recording visible light signals[24]. There are also some reports on using sCMOS cameras for X-ray imaging. However, scintillator layers are always needed to convert X-rays to visible light, and it is very rare to expose a bare sCMOS sensor to direct X-rays. Obtaining the spectroscopy information of X-rays is generally difficult for sCMOS cameras. In this research, it has been found that an ordinary sCMOS camera can work with direct X-rays and measure X-ray photon energy. The operational procedures include replacing the front cover, using the camera in single photon counting mode and analyzing camera images by the integrated-filtering method. All these operations do not require any modifications to the inner structures or on-chip electronics of the sCMOS camera and they can be conducted smoothly. In conclusion, the XRF spectra obtained by the sCMOS camera have highly accurate energy calibration and a fine energy resolution of 220 eV. The count rate capacity is also capable of measuring normal intensity X-rays. As a consequence, the visible-light sCMOS camera could be easily introduced to routine XRF analysis as a spectrometer. The composition of elements in samples can be analyzed as well. With installing external X-ray optics, the camera can also work for full-field XRF imaging. The specifications of the present sCMOS camera are listed in Table 2-1.

Table 2-1. Specifications of the sCMOS camera. From Ref[1].

| **A/D conversion** | **Pixel amount** | **Dynamic range** |
|---|---|---|
| 16 bits | 2560 × 2160 | 27000:1 |
| **Cooling** | **Pixel size** | **Readout noise** |
| Peltier | 6.5 μm × 6.5 μm | 1.1 electrons med |
| **Working temp.** | **Active area size** | **Maximum frame rate** |
| 5 ºC | 16.6 mm × 14 mm | 33 frames / s |

2.1.2. Conventional CCD camera

Conventional CCD cameras are designed for recording visible-light images. It has been understood for a long time that they can work in also X-ray wavelength region, though their quantum efficiency in the X-ray domain is low due to the thin depletion layer[25]. From the 1980s, some advanced CCD cameras, such as pnCCD, were specially developed for X-ray detection in astronomy use[12,26,27]. As the depletion layer thickness reaches hundreds of microns, the quantum efficiency in the X-ray domain (1 – 10 keV) becomes 90% or even higher.

A CCD camera records ordinary X-ray images by accumulating the charges created by many X-ray photons. In additional to this, it can also record many images corresponding to different X-ray photon energies by stopping the accumulation and taking many camera snapshots quickly. As the number of charges produced by a single X-ray photon is proportional to the X-ray photon energy, X-ray energy-dispersive spectra, and colorful X-ray images, can be obtained.

To do this, the CCD camera should be operated in a special way: single-photon-counting mode. Related discussion dates back to at least the early 1980s[11,28]. With using single-photon-counting mode, the advanced X-ray CCD camera, pnCCD, became energy-resolvable. The energy resolution was 152 eV at Mn K$\alpha$[13]. In the meantime, conventional CCD cameras working in single-photon-counting mode were tested as well. From the late 1980s, some pioneer attempts were made by Lumb et al.[14,29] and Tsunemi et al.[15,30,31] In these works, the knowledge of camera operation and data processing were clearly explained.

Using conventional CCD cameras for X-ray applications is attractive because of their low cost, easy maintenance and wide supply on the market. Many successful applications to laser-plasma fluorescence imaging, element mapping and even 3D chemical analysis have been reported. Most recently, Romano et al. reported two full field X-ray cameras which used conventional CCD cameras as detectors. The thickness of the camera depletion layer was 40 μm; the energy resolution was 133 eV at MnK$\alpha$. The outstanding performance have attracted a broad interest in using conventional CCD cameras for full-field XRF imaging.

In this work, we modified a conventional CCD camera (Hamamatsu C4880-50, the sensor CCD47-10 from e2V) for energy-dispersive X-ray imaging. The camera sensor has 1024 × 1024 pixels. The pixel size is 13 μm. The thickness of the camera sensor depletion region is approximately 10 μm. This thickness is more general in commercial visible-light CCD sensors than the 40-μm one employed by Romano et al. The X-ray quantum efficiency of CCD sensor is above 40% in the spectral range of 1 – 8 keV, e.g. about 45% at 6 keV. In order to apply the camera to direct X-ray measurement, the camera front cover is replaced by a new one, on which a circular X-ray window is fabricated. The X-ray window employed is commercially available 12 micron thick polymer film coated on both sides with 0.2 micron thick metallic aluminum (Ube Industries, Ltd.). The size is 4 mm dia. To reduce the light leakage caused by small pinholes (unsuccessfully coated parts), several sheets of the film were layered. This time 5 sheets were used. The film is strong enough mechanically and stable as a window for vacuum. The used window perfectly blocks visible light but is almost transparent for X-rays higher than 3 keV. The distance from the X-ray window to the CCD sensor is 14 mm.

In order to resolve X-ray photon energy, the CCD camera was operated in single-photon-counting mode. In this mode, the camera takes many snapshots in X-rays very quickly. The amount of incident photons one image is limited to a very low level. In this way, the recorded photon events are dispersed far away from each other, and therefore every photon event can be individually resolved with no interaction from other photon events. In practice, single photon counting mode is realized by either shortening the exposure time or weakening the X-ray intensity.

The key is to recognize photon events on CCD images and correctly retrieve the corresponding photon energy. To do this, we developed a double-threshold filtering method for the present CCD camera. When there is no illumination of visible light or X-rays, the CCD gives a black image in which the intensities of all pixels are quite similar. When one pixel is affected by an X-ray photon, its intensity becomes higher. Therefore, a numerical threshold is proposed to recognize these higher intensity pixels as X-ray signal pixels. In order to avoid counting the non-signal pixels whose intensity is only slightly higher than the average background intensity due to random fluctuation of dark current, the difference between the threshold and the background intensity should be distinctly larger than the fluctuation amplitude of dark current. In the present work, the fluctuation amplitude of dark current is around 40 channels of pixel intensity, and the difference

is set as 60 channels of pixel intensity. After employing the numerical threshold, it is found that there are two types of photon events: a single-pixel event has only one isolated signal pixel while a split event has several neighboring signal pixels. The spectral range of incident X-rays in the present work is with 1 – 8 keV. In this spectral range, the size of a split event is smaller than 3 × 3 pixels. The average fraction of single-pixel event in all photon events of all XRF experiments is around 18%, and the standard deviation of different experiments is less than 3%. There is no evident relation between the fraction and the incident X-ray photon energy, which means the fraction of single-pixel event is a constant instrumentation parameter in the spectral range of 1 – 8 keV.

Then, the most important is to retrieve the exact photon energy of single-pixel events and split events. If the depletion layer of the CCD sensor is thick enough, most X-ray photons can be absorbed in the depletion layer. Therefore, photoelectrons generated by one X-ray photon can be immediately collected by one or several neighboring pixels without charge loss. In this case, the X-ray photon energy is exactly proportional to the pixel intensity of the single-pixel event or the integrated pixel intensity of the split event. This operation is suitable for CCD cameras which has a thick depletion layer, for example, the pnCCD with a 450-μm-thick sensor depletion layer and the conventional CCD camera with a 40-μm-thick depletion layer utilized by Romano et al. However, most conventional CCD cameras have a much thinner depletion layer. For these thin depletion layer CCDs, some X-ray photons can go through the depletion layer and be absorbed in the field-free region below. In this case, the photoelectrons generated by one X-ray photon diffuse rapidly. Some charges may spread back to the depletion layer and are then collected by several neighboring pixels due to the large diffusion area, whereas the rest of the charges are lost, resulting in a charge-loss split event. The integrated pixel intensity of a charge-loss split event will underestimate the corresponding photon energy. In practice, it is very difficult to recognize a charge-loss split event from all split events. For this reason, all split events should be abandoned to avoid any risk of incorrect photon energy retrieval. Only single-pixel events are considered as valid events. This operation is frequently applied to CCD cameras of which the depletion layer is thinner than 20 μm. It is able to introduce the most general conventional CCD cameras to the field of X-ray spectroscopy, and it is more robust for many types of CCD cameras than other integration methods or mathematical fitting methods.

Sometimes, underestimation of photon energy may also happen even for a single-pixel event: A small portion of charges could be leaked to surrounding pixels. The amount of leaked charges is so small that the intensity of surrounding pixels is not apparently higher than the background intensity. In detail, the intensity increase of surrounding pixels is within the fluctuation amplitude of dark current. These charge-leaked events lead to low-energy tails to every peak in XRF spectra, which will reduce the performance of detecting minor elements. In order to reject the charge-leaked events as much as possible, another strict and lower threshold is proposed to check the surroundings of a single-pixel event. The difference between this lower threshold and the background intensity is smaller than the dark current amplitude. In the present work, it is set as 20 channels of pixel intensity. A standard sample of known composition has been tested to reveal the influence of charge-leaked events and the function of the lower threshold.

To sum up, two thresholds are proposed to obtain valid X-ray signals and to filter out undesirable photon events. Using the first higher threshold can efficiently recognize X-ray signals and distinguish single-pixel events and split events, therefore, the strong background in the low energy side of the whole XRF spectra can be removed. Using the second lower threshold can effectively reject charge-leaked photon events, therefore, low-energy tails of every peak can be significantly reduced. The present filtering method may sacrifice the efficiency of accumulating X-ray signals, however, it is a quite robust way to obtain high quality XRF spectra and to perform reliable XRF analysis with thin depletion layer CCD cameras.

In the final, each valid X-ray signal is represented by a 3-dimensional coordinate $(X, Y, I)$, where $X$ and $Y$ are its position on the image, and $I$ notates its intensity. In order to generate X-ray energy-dispersive spectra, the frequency distribution of $I$ of all signals is counted as a histogram. In order to generate X-ray spectroscopy images, the signals whose intensity locates in the region of interest (ROI) $[I_{low}, I_{up}]$ are painted on the image as a heat map. If all XRF photons are projected via an appropriate X-ray optical component, e.g. a micro pinhole, from a sample, the heat map on the ROI $[I_{low}, I_{up}]$ shows the spatial distribution of corresponding elements in the sample.

An overall flowchart of filtering and image process is given in Figure 2-3.

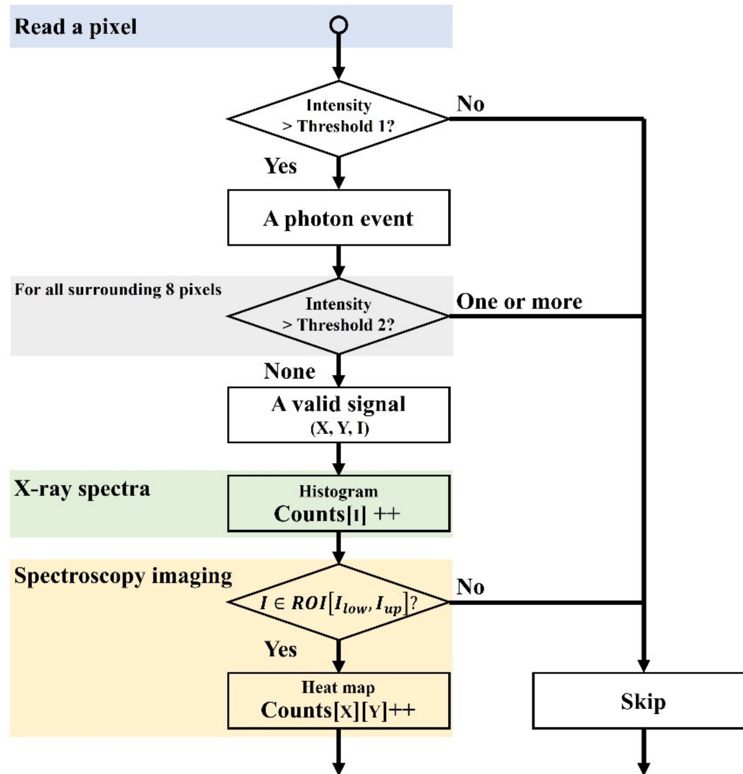


Figure 2-3. Flow chart of imaging processing of CCD camera snapshots.

The CCD camera is utilized to measure XRF spectra of different samples to examine its feasibility in X-ray spectroscopy. In this measurement, the 4-mm-dia X-ray window is fully open, and no additional X-ray optical component is installed. The exposure time of one camera snapshot is 1 second. In this condition, single-photon-counting mode is satisfied. In order to accumulate sufficient X-ray signals, in total 500 snapshots are acquired. The total accumulation time is 500 seconds. The image processing is usually done in parallel to the acquisition of images. All X-ray data including the XRF spectra can be output immediately after the measurement concludes.

The relation between pixel intensity I and the corresponding X-ray photon energy E is calibrated by measuring a standing sample containing potassium, titanium, chromium, iron, and cobalt. In this work, the calibration function is $E = a \cdot I - b$, where $E$ is the photon energy in eV, $I$ is the pixel intensity of a valid X-ray signal, $a = 2.9452$ and $b$=5497.5. The coefficient $a$ is mainly determined by the amplification gain of the CCD camera.

In the present work, the lower energy side limit is around 3 keV. The spectral peaks below 3 keV cannot be detected. As the main reason for this is the absorption in the aluminum coated X-ray window, it is worth considering optimizing the thickness depending on the analysis of the elements contained in the samples. The energy resolution of the CCD camera is determined as 150 keV at 5900 eV by measuring the full-width-at-half-maximum of Mn K$\alpha$ peak.

In order to confirm whether the CCD camera can detect minor elements, a natural sample is measured by the CCD camera and a commercial SDD (Amptek Inc.), respectively. The accumulation time of the SDD measurement is 60 seconds. Two spectra are compared [Figure 2-4 (a), (b)]. The natural sample is pond sediment powders of Environmental Certified Reference Materials from the National Institute for Environmental Studies, Japan (NIES CRM NO.2)[32]. For ease of measurement, 30 wt.% of pond sediment powders are mixed into cellulose matrix and then pressed into a pellet. The final weight percentage of potassium, calcium are 0.23%, 0.27%, respectively. For ease of comparison, the peaks of potassium and calcium are enlarged. Although the concentrations of the two elements are low and the peaks are weak, the intensity profiles in CCD-measured spectra and SDD-measured spectra look similar. This is owing to the low background in the CCD-measured spectra.

In Figure 2-4 (c), it is noted that the CCD camera can detect the small Mn K$\alpha$ peak although the amount of manganese is very low. In minerals, manganese is often associated with iron. When a major amount of iron exists, detection of the minor amount of manganese becomes difficult, because the small Mn K$\alpha$ peak may submerge into the low-energy tail of the intensive Fe K$\alpha$ peak. In this measurement, a sample of standing steel (JSS 066-4, carbon steel) is tested. The sample contains 0.79 wt.% manganese and more than 98 wt.% iron. The small Mn K$\alpha$ peak can be clearly recognized at the foot of the intensive Fe K$\alpha$ peak. This is owing to the high energy resolution and small low-energy tail of the CCD camera in XRF spectroscopy measurement. It should be figured out that the small Mn Kα peak cannot be recognized when the second lower threshold is not employed. This experiment has reconfirmed the necessity of rejecting charge-leaked photon events.

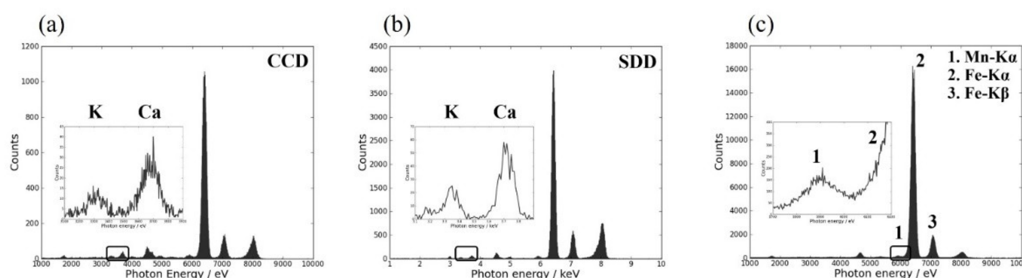


Figure 2-4. XRF spectra analysis with the CCD camera. (a) and (b) are the spectra of a pond sediment sample, measured by CCD and SDD, respectively. (c) shows that the CCD camera is able to identify low-concentration Mn in a steel alloy. From Ref[2].

In conclusion, we have found that a conventional CCD camera for optical use is competitive enough to serve as a large-area-size X-ray spectrometer. As it has large amounts of pixels and fine pixel size, it can effectively work contribute to full-field XRF imaging when appropriate X-ray optics are introduced. The specifications of the CCD camera are summarized in Table 2-2 below.

Table 2-2. Specifications of the CCD camera. From Ref[2].

| **A/D conversion** | **Pixel amount** | **Dynamic range** |
|---|---|---|
| 16 bits | 1024 × 1024 | 13300:1 |
| **Cooling** | **Pixel size** | **Readout noise** |
| Water + Peltier | 13 µm × 13 µm | 6 electrons rms |
| **Working temp.** | **Active area size** | **Maximum frame rate** |
| - 30 $^{o}$C | 13.3 mm × 13.3 mm | 0.25 frames / s |

### 2.2. X-ray optics for full-field XRF imaging

In order to image the elements, an X-ray optical component has to be introduced between the sample and the 2D energy-dispersive detector to project XRF images from the sample to the detector. The function of the X-ray optical component is quite similar with the convergence lens system for taking photos in visible light. However, because the photon energy of X-rays and visible light is extremely different, this is no convergence lens system that can work for X-rays. Special X-ray optical components are designed for full-field XRF imaging, such as X-ray reflection mirrors, poly-capillaries, a micro pinhole, and a collimator plate.

When the incident X-rays hit a smooth surface of matters in grazing incidence, the incident X-rays can be totally reflected. On this principle, some complicated X-ray reflection mirror systems are fabricated, such as the Wolter-type mirror and the Kirkpatrick-Baez (KB) mirror. These mirrors can project X-ray beams with convergence or divergence. Poly-capillaries are another option which projects X-rays by the total reflection at the inner surface of many curved capillaries. However, fabricating and polishing curved X-ray mirrors of poly-capillaries are generally not easy. In our work, we use micro pinholes and collimator plates.

2.2.1. Micro pinhole

A micro pinhole is frequently used in XRF imaging. The size of the micro pinhole determines the spatial resolution of XRF imaging. However, in order to shield X-rays, the thickness of the pinhole plate must be several tens of microns. Then it is difficult to manufacture a very small pinhole. On the other hand, when the pinhole size approaches the pinhole plate thickness, mathematical expression of spatial resolution become less reliable, thus the actual spatial resolution must be tested with direct resolution targets. To our knowledge, common spatial resolution achieved in pinhole X-ray imaging is from 50 to hundreds of microns. Romano et al. achieved 30 μm spatial resolution by manufacturing a 50 μm pinhole on a 70-μm-thick tungsten plate[8]. In the present work, we are able to improve the spatial resolution of pinhole X-ray imaging to 15 μm.

Figure 2-5 shows one result of pinhole full-field XRF imaging obtained with the CCD camera and a laboratory X-ray source. The spatial resolution is tested as 20 μm. The laboratory X-ray source is a sealed type X-ray tube of copper target (TOSHIBA A26L-Cu, 1.5 kW) equipped with a crystal monochromator (graphite (002), 2d = 6.72 Å). A micro pinhole was attached on the top of the camera front cover. The pinhole size is 12 μm. It is drilled on a 30-μm-thick tungsten foil by 266 nm UV lasers. The test target is black chromium patterns coated on transparent glass substrate [Figure 2-5(a)]. The thickness of the chromium layer is 1000 Å. As shown in the photo, in each group, the chromium bars are equidistantly distributed in 1 mm gaps, and their individual width equals the separation between each of them. The numbers across the top show the number of bars in each group. In this experiment, the distance from the target to the pinhole is 2 mm; the distance from the pinhole to the CCD sensor is 14 mm; hence the magnification of pinhole imaging is 7. Limited by the camera sensor size, the observation area on the target is 1.9 mm × 1.9 m, indicated by the dashed square in Figure 2-5(a). The separation of observed bars in the center is 20 μm. As the pinhole size is small and the coated chromium layers are thin, the measurement time becomes long to one week. In the final, The full-field XRF spectra of the viewing area are shown in Figure 2-5(b). In the spectra, the peaks of calcium and chromium can be identified. Here, the calcium is inferred from the glass substrate. The glass substrate may also contain other elements such as silicon and sodium, however, this time they cannot be detected because their fluorescent X-rays are strongly absorbed in the CCD window materials. The images of calcium [Figure 2-5(c)] and chromium [Figure 2-5(d)] are painted by signals in the ROIs of their respective peaks. In the calcium image, the XRF intensity distribution is homogeneous, which indicates that calcium is homogeneously distributed in the glass substrate. In the chromium image, the chromium bars with 20 μm separation can be clearly distinguished, indicating that spatial resolution is better than 20 μm.

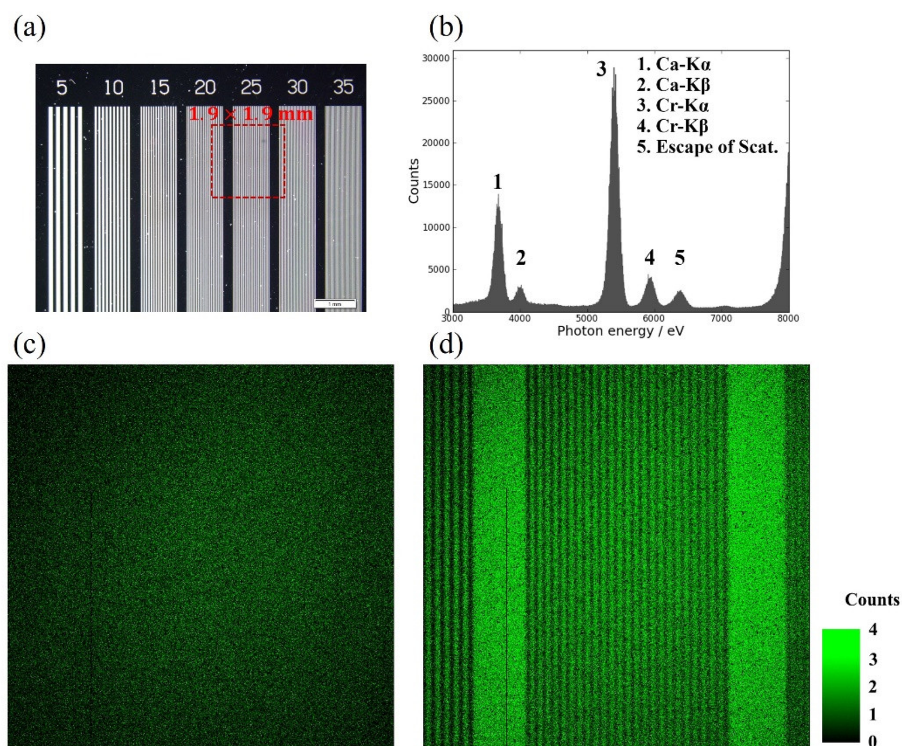

Figure 2-5. 20-μm spatial resolution obtained in pinhole XRF imaging. (a) shows the photo of the test target; the observation area is marked by the dashed square. (b) shows the acquired XRF spectra. The imaging results of Ca in the substrate and Cr in black patterns are shown in (c) and (d), respectively; the Cr bars with 20-μm separation are clearly distinguished. From Ref[2].

Figure 2-6 shows one result of pinhole full-field XRF imaging obtained with the sCMOS camera and synchrotron radiation. The spatial resolution is tested as 15 μm. The experiment is carried out in Beamline14B, Photon Factory, KEK. The primary X-ray beam is monochromatized to 9.53 keV by a double-crystal Si(111) monochromator. In this experiment, the pinhole size is 10 μm, manufactured on a 50-μm-thick tungsten foil. The distance from the pinhole was 1.65 mm to the target and 14 mm to the camera sensor; hence the magnification in pinhole imaging is about 8.5 times. The resolution target was chromium patterns (4000 Å thick) coated on a silica glass [Figure 2-6(a)]. In the final, the full-field XRF spectra [Figure 2-6(b)] showed the major spectral peaks of chromium from the target as well as an XRF contamination of copper and zinc which came from the brass housing of the camera. The XRF image of chromium [Figure 2-6(c)] showed that patterns separated by at least 15 μm can be resolved, indicating a spatial resolution of 15 μm.

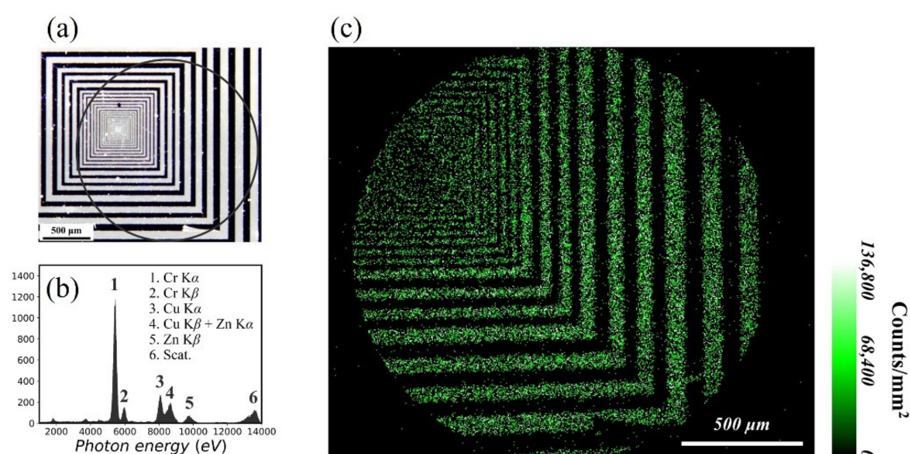


Figure 2-6. Full-field XRF imaging of a commercial resolution target sample. (a) An optical photograph of the resolution target. The black rectangular patterns are chromium coatings. The XRF imaging area is enclosed by the circle and the scale bar is 500 μm. (b) Full-field XRF spectra accumulated for 6 h. (c) An XRF image Cr Kα and Kβ. From Ref[33].

In pinhole XRF imaging, a smaller pinhole brings a better spatial resolution, however, it also reduces the transmitted intensity and therefore worsens the measurement efficiency. In practical experiments, larger pinholes, e.g. 50 μm to 100 μm, are frequently applied to obtain a higher measurement efficiency. Figure 2-7 shows the element map in a natural agate stone [Figure 2-7(a)] measured by the CCD camera and the laboratory X-ray sealed-type copper tube. The pinhole size is 38 μm. The magnification imaging is 4. The spatial resolution in this condition has been tested as 50 μm. The observation area is 3.9 mm × 3.9 mm, indicated by the dashed square in Figure 2-7(a), which shows yellow substrates and black fringes. A white mark of titanium dioxide is pasted on the sample to confirm the observation area more easily. In the full-field XRF spectra [Figure 2-7(b)], the peaks of titanium, manganese and iron are observed. The small Mn Kα peak is just at the foot of the intensive Fe Kα peak. The agate stone may have a silicon matrix, however, as the lower limit of valid spectra range is 3 keV, silicon or other low-Z elements were not observed. Some high-Z elements which cannot be excited by the primary Cu Kα beam cannot be detected either. The titanium image [Figure 2-7(c)] is painted by signals in ROI of Ti Kα peak and Ti Kβ peak; the manganese image [Figure 2-7(e)] is painted by signals in ROI of Mn Kα; the iron image [Figure 2-7(d)] is painted by signals in ROI of Fe Kα and Fe Kβ. This time, 2×2 binning has been applied to make the images more visible. Because the spatial resolution is limited by the pinhole size (around 50 μm in this case) and the pixel size is 13 μm ×13 μm, the 2×2 binning does not lead to any loss of information.

By comparing the sample photo to element images, the relation between the sample appearance and element distribution is clarified: Black fringes on stone relate to iron deposition, and manganese contributes to the black dots with special gloss, which are marked by A and B in Figure 2-7(a) and Figure 2-7(e). This

time, the small Mn K$\alpha$ peak is at the foot of the intensive Fe K$\alpha$ peak, however, by virtue of the CCD camera's fine energy resolution and small low-energy tail, the Mn K$\alpha$ peak can be clearly distinguished in XRF spectra. Purely on this basis, it becomes possible to clearly image the spatial distribution of manganese with little influence from iron background.

Using a micro pinhole for full-field XRF imaging has many advantages: low cost, simple instrumentation and alignment, flexible sample-to-detector distance, flexible imaging magnification, and high spatial resolution to 15 μm when the pinhole size is around 10 μm. This is the reason why micro pinholes are used in many following XRF imaging experiments. However, the compromise between the spatial resolution and imaging efficiency is unavoidable. Other X-ray optical components with a similar spatial resolution and a much better imaging efficiency could be used.

In optical pinhole imaging, the optimal pinhole size and spatial resolution is determined by the wavelength of light. As the wavelength of visible light is 400 ~ 700 nm, an intuitive idea would be that the optimal pinhole size is about one micron. However, when the pinhole is small, geometrical optics does not pertain, but Fraunhofer diffraction pertains[34]. The best spatial resolution occurs in the condition of $s^2 \sim 0.61\lambda f$, where $s$ denotes the pinhole size, $f$ denotes the distance from pinhole to camera sensor, and $\lambda$ denotes the wavelength of light. For example, when 400 nm light is used and the pinhole-to-sensor distance is 1 mm, the optimum pinhole size as well as the best spatial resolution is 15.6 μm. Theoretically speaking, the spatial resolution may become much better in case of a small pinhole-to-sensor distance, but this appears to be less practical.

In X-ray pinhole imaging, the optimal pinhole size and spatial resolution is not determined by the wavelength of X-rays any more. Instead, it is determined by the necessary thickness of a pinhole screen opaque to X-rays. Because of penetration power of X-rays, the necessary thickness is several tens of microns to hundreds, depending on X-ray photon energy and the material of screen. Tungsten foils are used in the present work. The thickness is 25 μm or 50 μm. In this case, it is difficult to manufacture a very small pinhole on the thick foil. Even when the very small pinhole is successfully manufactured, it works like a tunnel or a collimator rather than a pinhole, and it cannot project wide images. Pinholes of 10 μm ~ 20 μm are already nearly the limitation. Such pinholes are prepared in our lab with using UV lasers. The best spatial resolution of X-ray pinhole imaging is verified to be 15 μm. So far, this has been the best level of XRF pinhole imaging.

#### 2.2.2. Collimator plate

Sometimes a collimator plate is used for full-field XRF imaging. Figure 2-7 shows the illustration illustration of the imaging optics. The collimator plate assembles many parallel straight hollow capillaries. The thickness of the collimator plate is 1 mm. The diameter of each capillary is 6 μm. The overall opening ratio of the collimator plate is 0.58. The collimator plate is made of glass. The inner surfaces of the capillaries are coated with thin gold films to prevent X-ray transmission. In the experiment, the collimator plate is fabricated inside the camera housing. When the gap width between the sample surface and the camera sensor is close, e.g. 3 mm, high-resolution XRF images can be obtained. The spatial resolution is mainly influenced by the sample-to-detector distance, given by $Resolution = (d/t) \cdot l$, where $d$ is the capillary diameter, $t$ is the collimator plate thickness, and $l$ is the sample-to-detector distance. When the instruments are well aligned, $l$ can be 2.5 mm ~ 3 mm, then the corresponding spatial resolution is 15 μm ~ 20 μm.

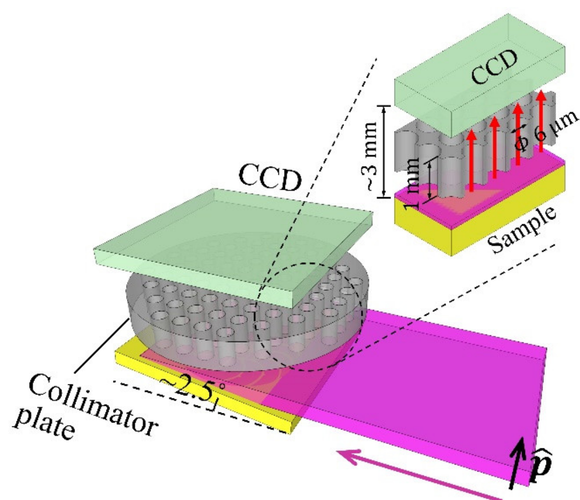


Figure 2-7. Schematic illustration of the full-field XRF imaging setup with a collimator plate. From Ref[35].

Figure 2-8 shows one result of collimator imaging with using the laboratory X-ray source, the CCD camera, and the collimator plate. The resolution target is one part cut from that used in Figure 2-5. The image shown here shows the distribution of chromium. The full available viewing area is about 13 × 13 mm, which is the same as the CCD sensor size, as the collimator plate leads to 1:1 imaging. The actual sampling size is limited by the primary beam size. In the image, chromium bars with 20 μm separations can be distinguished, indicating a spatial resolution of 20 μm.

Utilizing a collimator plate for XRF imaging was introduced by Prof. Kenji Sakurai at 1999 [36]. After that, the collimator plate has been successfully applied to XRF movie imaging[37], X-ray diffraction (XRD) imaging[38], X-ray absorption fine structure (XAFS) imaging[39,40], etc. In this work, we first use the collimator plate with taking camera snapshots for energy-dispersive XRF imaging. There are many advantages of using the collimator plate: First, it allows a very close sample-to-detector distance. Second, it has a much higher imaging efficiency compared with a micro pinhole. In the final, in an XRF imaging experiment with the collimator plate, the solid angle for all parts on the sample are the same. This provides a great convenience for comparing the quantitative information in imaging. It should be figured out, with using the same collimator plate, the overall detected XRF intensity does not change when the sample-to-detector distance changes, but the achieved spatial resolution changes correspondingly. However, with fixing the sample-to-detector distance and the collimator plate thickness, the spatial resolution becomes better but the transmitted XRF intensity becomes weaker when the diameter of the capillaries reduces. This is to say, there is still an unavoidable compromise between the spatial resolution and the measurement efficiency. One may choose the most suitable collimator plate depending on the actual experimental requirements.

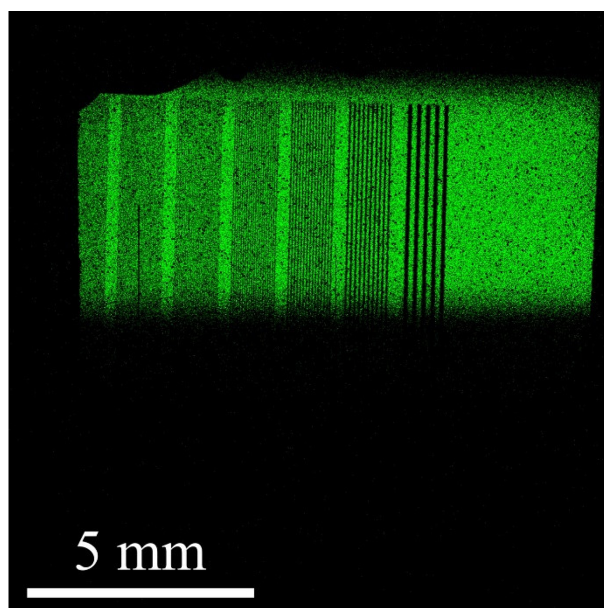


Figure 2-8. Chromium imaging with using the collimator plate and the CCD camera. The verified spatial resolution is 20 μm.

**2.3. Spatial resolution and time resolution**

Spatial resolution and time resolution are two key parameters of full-field XRF imaging. They determine the applicable field of the technique. So far, they still suffer clear limitations. More applications may become possible after removing the limitation factors.

The primary limit factor is the X-ray optical component. In the present work, we use a micro pinhole and a collimator plate. X-ray imaging is realized by selecting fluorescence X-rays spread in specific directions and screening X-rays in other directions. Therefore, only a small part of X-rays can pass the optical component, resulting in the weak intensity of X-ray imaging. The compromise between spatial resolution and time resolution is always unavoidable. Meanwhile, so far, our achieved spatial resolution has reached nearly the physical limitation of two X-ray optical components. The spatial resolution is about 15 μm.

The spatial resolution may become better with using other X-ray optical components. Fresnel zone plate can project X-ray images with a spatial resolution of 200 nm. However, it only passes a specific X-ray wavelength and it cannot image different elements simultaneously. Conical polycapillariy can project X-ray images with a magnification up to 10. The corresponding spatial resolution is several microns. One micron resolution is possible with current technological level although challenging. Kirkpatrick-Baez mirror[41,42] uses four total-reflection mirrors to project X-ray images with tens of times magnification. A spatial resolution of 0.5 ~ 1 μm of full-field XRF imaging has been achieved in SPring-8. Wolter-type mirror (axially symmetric mirror)[46] is another option for projecting high-magnification X-ray images. About twenty years ago, the resolution of full-field XRF imaging has been around 10 μm. Recently it becomes up to 250 nm, and it may become 100 nm in the coming several years. The axially symmetric mirror has a working distance below twenty centimeters and can be used with laboratory X-rays. Clearly it will make a breakthrough in the field of X-ray microscope.

Pixel size of X-ray detectors is the second limit factors of spatial resolution. In general, the pixel size is several microns to tens of microns. It does not influence the spatial resolution when imaging magnification is large enough. However, when the imaging magnification is low, the pixel size may become the bottleneck. At present, methods of reaching a sub-pixel resolution or adopting sub-micron pixel detectors are still under development.

In time-resolved XRF imaging or XRF movie imaging experiments, the time resolution is always limited by the low detected XRF intensity. In the future, it will be improved with using stronger synchrotron X-rays and high-efficiency X-ray optical components. On the other hand, even with present X-ray sources and X-ray optical components, still the time resolution can be greatly improved by optimizing the design of

sample reaction cells. Simple operations including shortening the sample-to-source distance, using a thinner X-ray window in the sample cell, and reducing the thickness of covered aqueous layers in the observation of liquid-phase reactions would be very much useful.

**2.4. X-ray sources**

In this work, the utilized light sources include laboratory X-rays and synchrotron radiation. Corresponding experimental schemes are determined by practical requirements. From the viewpoint of XRF analysis, the differences of laboratory X-rays and synchrotron radiation are briefly compared and summarized in Table 2-3.

The wavelength of synchrotron radiation is continuously adjustable. One may choose the optimal wavelength at his preference or continuously scan the wavelength for X-ray absorption fine structure (XAFS) analysis by changing the diffraction angle at the monochromator. Laboratory X-rays come from an X-ray tube. It has a continuous bremsstrahlung radiation and characteristic spectral lines of the metal target. Monochromators can also be used to select monochromatic X-rays in one characteristic line. The selected wavelength, the beam path, and the diffraction angle at the monochromator are generally fixed. Sometimes, the selected wavelength is also continuously adjusted in the spectral part of bremsstrahlung radiation. However, the corresponding X-ray intensity is weak, unless a special X-ray tube[45] for laboratory XAFS experiments is developed.

In laboratory, the X-ray beam intensity for X-ray diffraction (XRD) analysis is generally not exceeding $10^8$ counts/sec. For XRF analysis, the requirement of angular divergence and monochromaticity is not very strict. The X-ray beam intensity can reach $10^9$ counts/sec/mm$^2$. This is weaker than synchrotron radiation, but it can still do XRF movie imaging of gradual chemical diffusion. The intensity of synchrotron X-rays varies greatly from beamlines to beamlines. It is influenced by many factors such as electron energy in the storage ring, number of insertion devices, selected wavelength, bandwidth, mirror focusing, etc. In the most general sense, the synchrotron beam intensity is $10^{11} \sim 10^{12}$ counts/sec/mm$^2$.

Laboratory X-rays are mostly unpolarized. In some cases, if a monochromator is used, the degree of polarization (DOP) will be slightly altered due to X-ray diffraction at the monochromator. For example, the DOP of Cu Kα X-rays monochromatized by a polygraphite crystal (002) is 0.05, which is frequently neglected. On the other hand, laboratory X-rays can also become highly polarized if they are strictly collimated to ensure an exact ninety-degree deflection angle by either scattering from low-Z materials or Bragg diffraction, whereas the intensity becomes further weaker. Synchrotron radiation is inherently highly linearly polarized. The DOP is generally greater than 0.95. However, the beam size of synchrotron radiation is large in the direction parallel to polarization and small (< 2 mm) in the direction perpendicular to polarization. This results in difficulties of setting full-field XRF imaging instruments: The scattering background is even stronger than that with laboratory unpolarized X-rays. This does not influence major-element imaging, but it causes troubles of seeing minor and trace elements. The trouble can be solved by expanding the polarized synchrotron beam in the direction perpendicular to polarization. The method is described in Chapter 3.

In synchrotron beamlines, sample position is far away from the source point, generally several meters to tens of meters. Synchrotron beam is frequently collimated in a point or line shape with high wavelength resolution and very small angular divergence, enabling precise analysis of XRD, X-ray reflectivity (XRR), and X-ray standing wave (XSW). Laboratory setups have much more flexibility. The sample can be very close to the focusing point in the X-ray tube. In some full-field XRF imaging experiments, the primary X-ray beam can be uncollimated and quite wide. Monochromator can also be removed. This is to make the intensity of laboratory X-rays as large as possible for XRF imaging experiments.

Table 2-3. Comparison of synchrotron radiation and laboratory X-rays

| | Synchrotron radiation | Laboratory X-ray source |
|---|---|---|
| Wavelength | Continuously adjustable | Fixed, characteristic to X-ray target |
| Polarization | Linearly polarized | Nearly unpolarized |
| Photon flux | $10^{11} \sim 10^{12}$ cps/mm$^2$ | $10^8 \sim 10^9$ cps/mm$^2$ |

| | | |
|---|---|---|
| Beam manipulation | Monochromator used; thin beam, small divergence; large distance from source position to sample (meters) | Flexible; sometimes wide beam without monochromator; small distance from sample to focusing point |

**2.5. Other elemental imaging techniques**

Here I would like to make a comparison between present XRF imaging technique and other elemental imaging techniques.

Electron probe microanalyzer (EPMA) is a famous technique for element imaging. It scans an electron beam smaller than one micron on samples and analyzes characteristic X-rays, secondary electrons, Auger electrons, etc. emitted from the sample to map the distribution of elements at sample surface. When the signal for analysis is characteristic X-rays, the technique looks similar to scanning-type XRF imaging except that its probing beam is electrons rather than X-ray radiation. Its spatial resolution with using a desktop setup is better than one micron owing to highly development of magnetic lens. The technique is widely applied associated with the popularization of SEM. Nevertheless, XRF imaging has some clear advantaged compared to EPMA: (i) Vacuum environment. A vacuum environment is essential to use electron probes. This is clearly a limitation of EPMA to samples in various states and conditions. Problems may happen when a sample is wet or in liquid state (e.g. electrodeposited patterns in electrolyte) and when a sample is too large to put in the vacuum chamber (e.g. oil paintings). (ii) Probing depth. Electron analysis is generally surface sensitive. For EPMA, the probing depth is limited to several nanometers if the signals are electrons and can reach one to two microns if the signals are characteristic X-rays. In contrast, the probing depth of XRF imaging is much higher. For example, when the target element is iron, the probing depth in rock is more than one hundred microns, and in water it is more than one millimeter. The penetration power of XRF imaging makes it an indispensable tool to see reactions in solutions. (iii) Surface coating. Using electron microscopes, insulator samples need to be coated with a thin conductive layer like carbon or gold to avoid charge accumulation. This may influence the analysis of surface elements. In contrast, surface coating is unnecessary in XRF imaging. (iv) Radiation damage. EPMA is believed to be non-destructive to samples. However, it is still risky to characterize fragile cultural heritages on cloths, silks, or papers. XRF imaging is even safer compared to EPMA. So far, XRF imaging has been successfully applied to the investigation of many precious oil paintings.

Optical images are frequently recorded in the observation of chemical reactions. The color shown in visible light is considered as a partial evidence to infer the corresponding element in solutions. However, the color of one element is highly dependent on its concentration, valence, and mixture or compound with other elements. Therefore, the color shown in visible light is unreliable to tell the distribution of different elements in an on-going reaction. In contrast, the wavelength, i.e. the color of fluorescence X-rays is always characteristic of the element regardless of valences or chemical states. XRF imaging provides much reliable information on chemical elements than optical imaging.

In physiology, imaging of ions like $Ca^{2+}$, $K^{+}$, and $Cl^{-}$ is of great significance to reveal the mechanism of life activities in neural systems, cardiac muscles, and cancer tissues. Additional indicators of proteins or synthetic molecules are always needed to locate the ions or to quantify their amount. When these indicators are combined with the ions, characteristic fluorescence in visible-light domain will be emitted under the illumination of lambs or lasers. So far, this technique has become a mainstream method for biological functional imaging with a sub-second time resolution. However, it is generally difficult to design an indicator with good performance; the indicator is sensitive to only one specific ion rather than multi elements; and it is generally troublesome to introduce the indicators into bio-tissues by either genetical engineering or injection. In contrast, XRF imaging does not any additional indicator, and different elements can be simultaneously imaged. In recent years, XRF imaging technique has a ceaseless development. I believe its potential in biological functional imaging will appear soon.

# Chapter 3. Trace-element imaging with a size-expanded polarized synchrotron beam

*Portions of this chapter were adapted with permission from W. Zhao, K. Hirano, and K. Sakurai, Rev. Sci. Instrum. 90, 113704 (2019)[46] Copyright (2019) by American Institute of Physics and W. Zhao, K. Hirano, and K. Sakurai, J. Anal. At. Spectrom. 34, 2273 (2019)[35] Copyright (2019) by Royal Society of Chemistry.*

### 3.1. Introduction

Analyzing trace elements in samples is significantly important in many aspects: In environmental samples such as contaminated soils, marine products, and cereals, the concentration of harmful elements is frequently in trace level. In biological samples, the physiological activity is frequently influenced by some trace-level metal ions as coenzyme. In materials science, especially in semiconductors, a small number of impurity elements may greatly change the property of the material. In some chemical raw materials, such as pharmaceutical raw materials, the contaminants due to insufficient purification or catalytic metal residues are frequently in the ppm level.

On the other hand, the distribution of trace elements in the sample is frequently inhomogeneous. They can be aggregated into small particles or concentrated at special functional sites. For this reason, it is necessary to analyze the sample with a fairly large probing area to estimate the average concentration and to avoid the misjudgment due to the inhomogeneity. Also, it becomes even better if the spatial distribution of the trace elements can be imaged. That is to say, observing a small number of elements clearly by full-field XRF imaging is important.

However, as the small number of elements is diluted in a matrix, the scattering X-rays from the matrix are much stronger than the fluorescence X-rays from the elements. Even when primary X-rays are monochromatic and the scattering and fluorescence X-rays are detected with different energy channels by an energy-dispersive detector, the large counts of scattering X-rays in higher-energy channels may degrade the signal-to-background ratio in the XRF spectra, mainly due to incomplete energy collection at the photodiode of the detector. For this reason, it is necessary to block the scattering X-rays before they reach the detector.

A feasible approach involves using a linearly polarized X-ray beam because the angular distribution of the scattering intensity has a sharp minimum in the polarization direction. This approach has been applied to laboratory three-dimensional polarized XRF spectrometers[47,48] and synchrotron XRF experiments[49,50] to reduce the scattering background in XRF spectroscopy analysis. However, applying the same idea to full-field XRF imaging is difficult. To illuminate a large sample, an X-ray beam should be sufficiently wide in the direction perpendicular to its polarization. However, such X-ray beams are rare. Linearly polarized X-ray beams can be generated in the laboratory by scattering from low-Z materials[47,48] or Bragg diffraction[51,52]. when the deflection angle is $\pi/2$. To obtain a high degree of polarization (DOP) for a wide beam, a fine collimation by Soller slits[53] is necessary. This greatly reduces the beam intensity and makes it unsuitable for investigating diluted/trace elements. In contrast, using synchrotron radiation is much more convenient because of its strong intensity and perfect linear polarization in the electron motion plane. However, synchrotron radiation is inherently narrow (e.g. < 2 mm) in the direction perpendicular to the polarization, which makes it difficult to design an experimental setup. In this chapter, the best solution to use the excellent linear polarization for full-field XRF imaging was described. The proposed method is expansion of the beam perpendicular to the polarization vector.

### 3.2. Experiment

The experiments were done at BL-14B, Photon Factory, KEK, Japan. The beamline was equipped with a unique vertical wiggler[54,55] and a vertical Si(111) double-crystal monochromator. The primary X-ray beam is inherently vertically polarized, while ordinary synchrotron radiation is horizontally polarized. The used beam size in vertical is larger than 30 mm. The size in horizontal is about 2 mm. The beam was collimated in horizontal by the slits at the monochromator to ensure that the energy resolution was in the order of $10^{-4}$. The beam shape and polarization direction were rotated by 90° with respect to the synchrotron radiation using bending magnets or an ordinary horizontal wiggler. Nevertheless, the synchrotron radiation remained narrow in the polarization direction. Therefore, the difficulty encountered in this beamline is common to other beamlines. Table 3-1 lists several experimental setup layouts. The beam utilized is cut from the original full-beam size of 2 mm (H) × 30 mm (V). Layout A is typical for polarized XRF spectroscopy analysis. The detector is small and is placed vertical to the sample. The observation direction is the same as

the polarization direction, such that the collected scattering intensity is the minimum. Layout B is a similar scheme for full-field XRF imaging with the observation direction being vertical. The small detector is replaced with an X-ray camera and the sample is placed nearly horizontally, such that a long line on the sample is illuminated owing to glancing incidence. Layout B retains the perfect condition for minimizing the scattering intensity. However, it is unsuitable for large samples because only a thin strip of the sample can be illuminated. In contrast, Layout C can illuminate large areas of a sample, but its observation direction has to be perpendicular to the polarization and consequently, it collects the maximum scattering intensity. Layout C is the most commonly adopted in synchrotron full-field XRF imaging research because the imaging of concentrated/major elements is not significantly influenced by the scattering background. However, its diluted/trace elements imaging performance is severely limited, and sometimes it performs even worse than laboratory experiments with unpolarized X-rays.

This difficulty can be solved by decoupling the relation between polarization and synchrotron beam size. Instead of tailoring the polarization by special insertion devices[56–58] or phase-plate optics[59], in this work, a much simpler approach of manipulating the beam size was proposed. A synchrotron beam was expanded in the direction perpendicular to the polarization by asymmetric Bragg reflection, whereas the polarization direction was not altered. In this way, the requirements for illuminating large areas of samples and reducing the scattering background were simultaneously satisfied.

Table 3-1. Layouts of the experiment setup. Layout A is typical for synchrotron XRF spectroscopy analysis. Layout B and C are two available but imperfect layouts for full-field XRF imaging. Layout D is perfect after expanding the original beam in the horizontal direction, which is perpendicular to polarization; a large illumination area and the minimum scattering background are simultaneously realized. From Ref[46].

| | Utilized beam size / mm | Sample surface | Illumination / mm | Observation direction | Scattering |
|---|---|---|---|---|---|
| A | 2 (H) × 2 (V) | Vertical; normal to the x-ray beam | ~ 2 × 2 | Vertical | Min. |
| B | 2 (H) × 0.6 (V) | Nearly horizontal; glancing angle ~2.5 degree | ~ 2 × 13 | Vertical | Min. |
| C | 0.6 (H) × 13 (V) | Vertical; glancing angle ~ 2.5 degree | ~ 13 × 13 | Horizontal | Max. |
| D | 13 (H) × 0.6 (V) | Nearly horizontal; glancing angle ~ 2.5 degree | ~ 13 × 13 | Vertical | Min. |

In this study, the primary X-ray beam was generated using 2.5-GeV electrons in the storage ring of Photon Factory. The critical wavelength of the vertical wiggler was 0.5 Å. The distance from the wiggler to the experimental hutch was ~25 m. As shown in Figure 3-1, after expanding the primary X-ray beam in the horizontal direction by an asymmetric-cut Si crystal, the beam was cut in the vertical direction by a 0.6-mm slit. The sample was mounted nearly horizontally, with a glancing angle of 2.5° with respect to the primary X-ray beam. The conventional CCD camera (Hamamatsu C4880-50, sensor CCD47-10 produced by e2V), which was described in Chapter 2, was installed above the sample, facing downward. The CCD sensor was 10-µm thick and contained 1024 ×1024 pixels. The pixel size was 13 × 13 $\mu m^2$. The CCD sensor was designed for recording visible-light signals; however, in this study, it was operated in the single-photon-counting mode, so that it resolved the X-ray photon energy and recorded color X-ray images. The energy resolution was 150 keV at 5.9 keV. The X-ray optical component here is the collimator plate which has been described in Chapter 2. The width of the gap between the CCD sensor and the sample surface $d$ was adjustable. In this study, it was set to ~3 mm. The collimator plate, which assembled many parallel straight hollow capillaries, was inserted in this gap. The thickness of the collimator plate was 1 mm, and the diameter of the capillaries was 6 µm. The capillaries could project x-ray images from the sample to the CCD sensor.

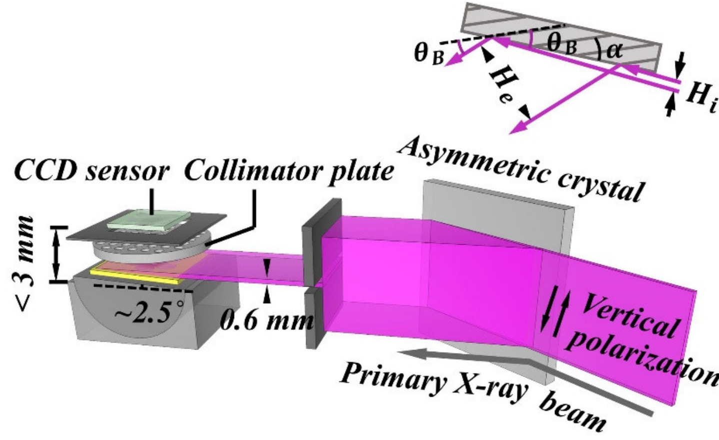


Figure 3-1. Schematic illustration of the experimental setup. The width of the primary x-ray beam was expanded from 2 mm ($H_e$) to ~39 mm ($H_i$) in the direction perpendicular to the polarization with using an asymmetric-cut crystal. The reflection lattice plane was Si(220). The miscut angle α was 18°. The Bragg diffraction angle $\theta_B$ was 19.79°. From Ref[46].

In order to demonstrate how much the scattering intensity was reduced by the present synchrotron polarized experiment, the XRF spectra of several standard samples containing trace elements were measured with the present synchrotron setup. In addition, one controlled trial was performed with unpolarized X-rays in the laboratory. The same samples were measured again. In the laboratory experiment, the primary X-rays came from a sealed-type copper X-ray tube. A crystal monochromator [graphite (002)] was employed to obtain monochromatic copper Kα X-rays (8.05 keV). The beam size was 1 (H) × 5 (V) mm. The full-beam intensity was on the order of $10^8$ counts per second. Because of the diffraction at the monochromator, the primary X-rays were slightly polarized with a DOP of 0.05, but the contribution to the observed scattering intensity is almost negligible. The sample was vertically mounted. The angle between the sample surface and primary X-ray beam was 3°. A Si-PIN detector (X-123 from Amptek) was placed in the same horizontal plane as the primary X-ray beam and the sample. The distance from the sample surface to the detector top was 80 mm. The active area of the detector sensor was 6 mm$^2$. The sensor thickness was 500 μm.

**3.3. Results**

In this experiment, the primary X-ray energy was set to 9.53 keV (1.3 Å). The Bragg diffraction angle at the Si(111) monochromator was 11.97°, which was close to the lowest limit of the monochromator. The reflection lattice plane in the asymmetric-cut crystal was Si(220). The corresponding Bragg diffraction angle $\theta_B$ was 19.79°. Thus, the expanding factor $b$ is given as follows:

$$b = \frac{\sin(\theta_B + \alpha)}{sin(\theta_B - \alpha)}, \tag{3-1}$$

where $\alpha$ is the miscut angle between Si(220) and the crystal surface. In practice, $\alpha$ was chosen according to a designed $b$. Specifically, $b$ was 19.62 and $\alpha$ was 18°. The width of the primary X-ray beam became ~39 mm ($H_e$) from 2 mm ($H_i$) in the direction perpendicular to the polarization. This width was sufficient to illuminate a large area on the sample (Layout D in Table 3-1).

As the collimator plate supported parallel optics and 1:1 imaging, the maximum imaging area was equal to the camera's sensor size, which was 13.3 × 13.3 mm$^2$. Therefore, the beam width utilized before expansion was 0.68 mm and occupied only a small central portion in the horizontal angular emission from the light source at the vertical wiggler. The corresponding angular width was 0.027 mrad. The DOP of this small portion, obtained using Schwinger's result to calculate the synchrotron intensity radiated from an accelerated electron, was as high as 0.998. However, because the horizontal emittance $\epsilon_H$ of the electron beam in the storage ring was too large to be neglected (36 nm rad), the DOP calculation should be corrected by considering the distribution of the electron's positions and angles of motion in the horizontal plane[60]. Considering the diffraction at the monochromator and the asymmetric-cut crystal, the final DOP of the

primary X-ray beam for the imaging experiment was 0.95. On the other hand, it is worth noting that, using the same beam expansion experimental scheme, the DOP can reach nearly one if the primary X-ray beam comes from bending magnets or an ordinary horizontal wiggler. This is because the vertical emittance of the electron beam in a storage ring is generally much smaller and neglectable, e.g., $\epsilon_V = 0.11$ nm rad in Photon Factory. In this case, to apply the same experimental scheme, rotation of the experimental setup by 90° was sufficient. In addition, because only a small portion of the original synchrotron beam was used, the X-ray intensity for imaging the samples was lowered in the order of $10^9$ counts per second. Because the illumination area was 13.3 × 13.3 mm$^2$, the photon flux on the sample surface was in the order of $10^7$ counts per second per square millimeter.

In this study, the collimator plate transmitted only X-rays that spread in the direction parallel to its capillary axis. The allowed angular divergence was only 6 mrad. Such a small angular divergence was also a key factor in minimizing the detected scattering intensity, because it completely took advantage of the sharp minimum in the angular distribution of the scattering intensity. The relationship between the signal-to-background ratio in the XRF analysis and the shape of the capillaries as well as the DOP of the primary x-rays is crucial in designing the experimental conditions to obtain the best XRF images. In addition, the small angular divergence led to a fine spatial resolution. A spatial resolution of 18 μm was once verified by measuring a standard resolution test. Sometimes, the resolution slightly varied depending on the actual gap width, but it was generally not greater than 30 μm.

The present setup was used to visualize the element distribution in a gabbroic rock collected at Mount Tsukuba, Japan. The rock surface was polished flat. In the experiment, the exposure time for every camera image was 20 s. In total, 1,500 images were acquired. The total accumulation time was 30,000 s. By comparing the sample photo [Figure 3-2(a)] and element maps [Figure 3-2(b),(c)], the relationship between the rock's appearance and element composition was clarified: the white matrix corresponds to calcium, and the black structures correspond to iron. Full-field XRF spectra [Figure 3-2(e)] and localized XRF spectra of specific regions [Figure 3-2(f)-(h)] provided more comprehensive information on the element composition. Small amounts of titanium and manganese were also detected, which is consistent with a detailed study on Tsukuba gabbroic rocks. Although the scattering peak should be located around 9.5 keV, it was nearly invisible in all linear-scale spectra. This clearly differs with a laboratory XRF measurement, in which the scattering and fluorescence intensity were of the same order of magnitude (Figure 3-3). In this experiment, the image of the scattering x-rays was nearly blank [Figure 3-2(d)], indicating that the influence of the scattering background on XRF imaging was neglectable.

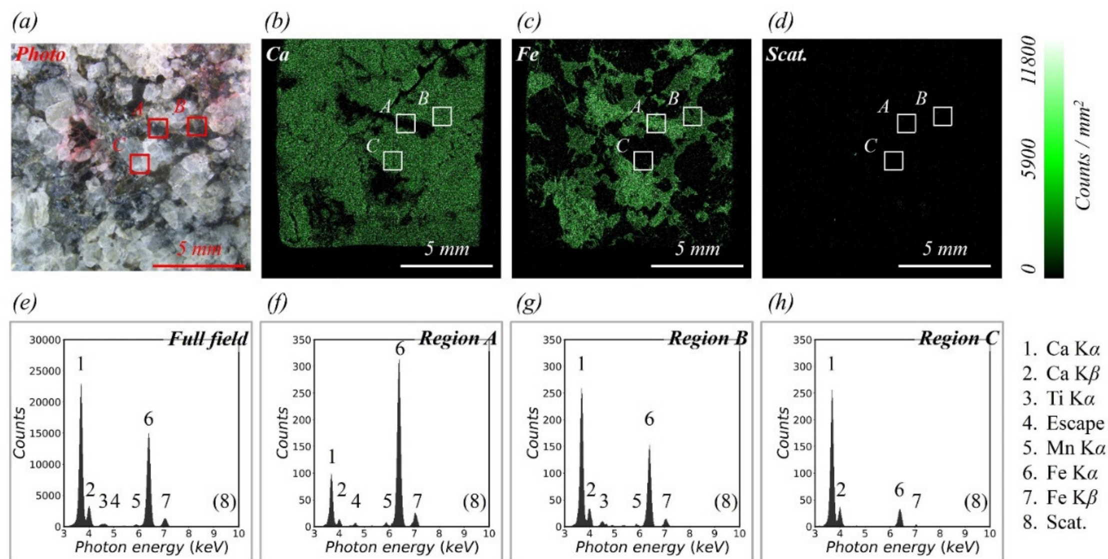


Figure 3-2. Full-field XRF imaging of a gabbroic rock from Mount Tsukuba. (a) Sample photo. (b), (c), and (d) are images of calcium, iron, and scattering x-rays, respectively. Every image has 1024 × 1024 pixels. (e), (f), (g), and (h) are the XRF spectra of the entire viewing area, Region A, Region B, and Region C, respectively. The scattering peak at ~9.5 keV is nearly invisible in all linear-scale spectra. From Ref[46].

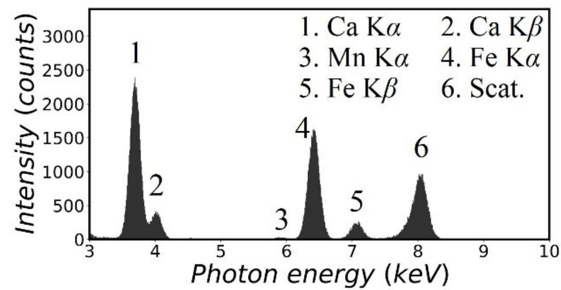


Figure 3-3. Laboratory XRF spectra of the gabbroic rock. The scattering intensity, calcium fluorescence intensity, and iron fluorescence intensity are on the same order of magnitude. From Ref[46].

In this experiment, owing to the small angular acceptance of the collimator plate and the low detection efficiency of the 10-μm-thick CCD sensor, measurements were made for hours to obtain high-quality XRF images with 1024 × 1024 pixels. However, the present layout is still attractive because of its unique ability to remove scattering x-rays, whereas the photon flux loss can be compensated by using stronger synchrotron radiation.

In order to demonstrate how much the scattering intensity was reduced, XRF spectra of samples containing trace elements were measured. Figure 3-4 shows the XRF spectra of a lithium borate pellet that includes 100 ppm chromium, iron, cobalt, and copper. The spectra in Figure 3-4(a) were measured in the synchrotron polarized experiment. The live time to accumulate the spectra was 4 h. The spectra in Figure 3-4(b) were measured in the laboratory unpolarized experiment. The live time to accumulate the spectra was 10 min. Details of the spectra were enlarged and attached to the right side. Information for all spectral lines was tabulated at the top of the figure.

On the basis of the two spectra, it was estimated that the sample contained more than 1% potassium, which might be introduced during sample preparation. In addition, a trace amount of nickel was detected. This was an unexpected contamination, and its concentration was estimated to be less than 50 ppm. It was noted that the relative intensities of the Kα lines of trace elements in the two spectra were different. This was owing to the thickness difference between the CCD sensor and the Si-PIN sensor, which resulted in different detection efficiencies for these spectral lines. In Figure 3-4(a), the scattering peak was located at 9.53 keV. Its intensity, including coherent scattering and Compton scattering, was on the same order of magnitude of the intensities of the Kα lines of the trace elements. In Figure 3-4(b), copper K lines were not excited. The scattering peak (8.05 keV) was even stronger than that of potassium Kα when the concentration of potassium was greater than 1%.

This significant difference in the scattering intensity was owing to the co-contribution of the polarization of the primary X-rays and the utilization of a collimator plate. For quantitative information, when two spectra were normalized by their respective iron Kα intensities, the intensity of scattering, which was inversely proportional to the SBR, was reduced to 1/15 from Figure 3-4(b) to Figure 3-4(a). It is worth noting that this quantitative comparison excluded the influence from the difference of the primary X-ray energies and detection efficiencies in the two experiments.

| | | | |
|---|---|---|---|
| **1** K K$\alpha$ | **2** K K$\beta$ | **3** Cr K$\alpha$ | **4** Cr K$\beta$ |
| **5** Fe K$\alpha$ | **6** Co K$\alpha$ + Fe K$\beta$ | **7** Co K$\beta$ | **8** Cu K$\alpha$ |
| **9** Cu K$\beta$ | **10** 9.5 keV *scat.* | **11** Cu K$\alpha$ *scat.* | |

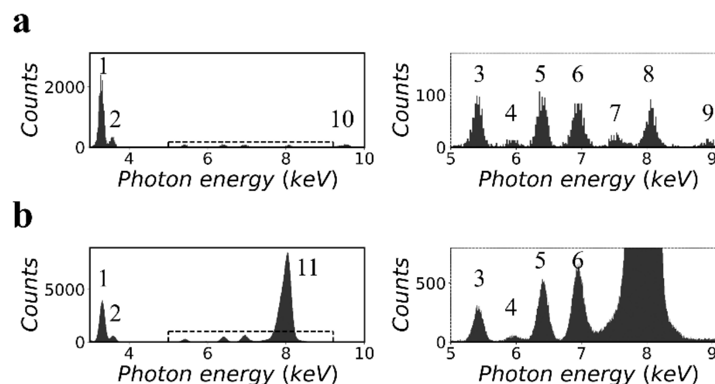


Figure 3-4. X-ray fluorescence spectra of lithium borate pellet that includes 100 ppm chromium, iron, cobalt, and copper. (a) measured in synchrotron polarized experiment, and (b) measured in laboratory unpolarized experiment. Details of spectra were enlarged and attached to right side. From Ref[35].

Figure 3-5 shows the XRF spectra of a CRM, NIST 81a, glass sand. To prepare the sample, the original material was mixed into cellulose powders at a mass fraction of 30%, following which the mixture was pressed into a pellet with a density of 1.5 g/cm$^3$. The spectra in Figure 3-5(a) were measured in the synchrotron polarized experiment. The live time was 2 h. The spectra in Figure 3-5(b) were measured in the laboratory unpolarized experiment. The live time was 10 min. On the basis of previous certified composition reports, the pellet sample was inferred to contain 147 ppm titanium, 7 ppm chromium, and 172 ppm iron, the K lines for which could be detected in the XRF spectra.

Other elements, *i.e.*, potassium, calcium, manganese, and copper, were detected. The concentrations of these elements were not reported previously. In this experiment, their concentrations were estimated to be a few ppm to tens of ppm. In Figure 3-5(a), owing to the low background intensity contributed by the small scattering intensity, the K lines of these trace elements can be detected despite the low counting statistics of the XRF spectra. In addition, the arrangement of spectral lines in Figure 3-5(b) showed good agreement with that in Figure 3-5(a), except that the cobalt K lines overlapped with the huge scattering peak, and the copper K lines were not excited by the 8.05 keV primary X-rays.

| | | | |
|---|---|---|---|
| **1** K K$\alpha$ | **2** Ca K$\alpha$ | **3** Ca K$\beta$ | **4** Ti K$\alpha$ |
| **5** Ti K$\beta$ | **6** Cr K$\alpha$ | **7** Mn K$\alpha$ | **8** Fe K$\alpha$ |
| **9** Fe K$\beta$ | **10** Cu K$\alpha$ | **11** 9.5 keV *scat.* | **12** Cu K$\alpha$ *scat.* |

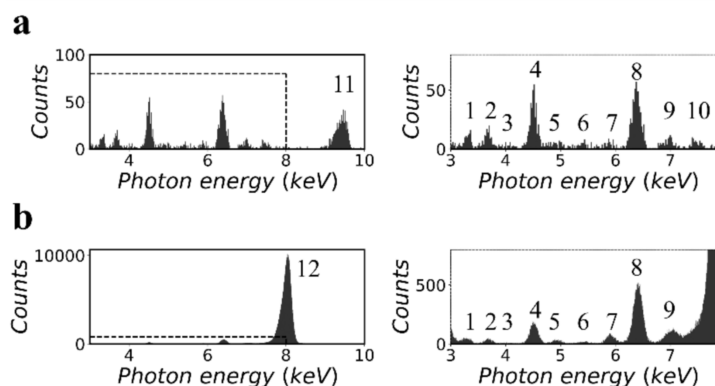


Figure 3-5. X-ray fluorescence spectra of CRM, NIST 81a, glass sand. Original material was mixed into cellulose matrix at mass fraction of 30%. (a) measured in synchrotron polarized experiment, and (b) measured in laboratory unpolarized experiment. Details of spectra were enlarged and attached to right side. From Ref[35].

Figure 3-6 shows the XRF spectra of a certified reference material (CRM), NIST 1515, apple leaves[61]. To prepare the sample, the original material was mixed into cellulose powders at a mass fraction of 30%, and then the mixture was pressed into a pellet with a density of 1.5 g/cm$^3$. The spectra in Figure 3-6(a) were measured in the synchrotron polarized experiment. The live time was 2 h. The spectra in Figure 3-6(b) were measured in the laboratory unpolarized experiment. The live time was 10 min. On the basis of previous certified composition reports, the pellet sample was inferred to include 0.49% potassium, 0.46% calcium, approximately 8 ppm titanium, 15 ppm manganese, 25 ppm iron, and 0.3 ppm nickel. In Figure 3-6(a), even though the spectra were unsuitable for quantitative analysis owing to the limited counting statistics, the above trace elements of low concentration could still be detected and identified. It was noted that the pellet sample also included 0.07 ppm vanadium and 0.03 ppm cobalt, of which the K lines were in the detectable X-ray energy range. However, these two elements were not detected owing to the minimum detectable limit. This experiment verified the feasibility of adopting the present experimental scheme in the detection of trace elements in low-Z matrices of environmental samples.

Figure 3-7 shows the X-ray fluorescence spectra of a CRM, JSAC 0615. This was a plastic disk that included toxic heavy metals[62]. The certified composition of the metals was 212 ppm chromium, 43 ppm cadmium, and 202 ppm lead. In the spectra, lead was not observed because its K lines or L lines were not excited by the primary X-rays. Cadmium was not detected either because its L lines are inherently weak and easily absorbed in the plastic matrix. Chromium was easily detected. In Figure 3-7(a), the Kα line was even stronger than the intensity of the scattering X-rays from the entire plastic matrix. In addition, two other trace elements, iron and cobalt, were detected. These two elements were probably contaminants during sample preparation or storage. This experiment verified the feasibility of adopting the present experimental scheme in the detection of trace toxic metals in plastic products, which is frequently a public health concern.

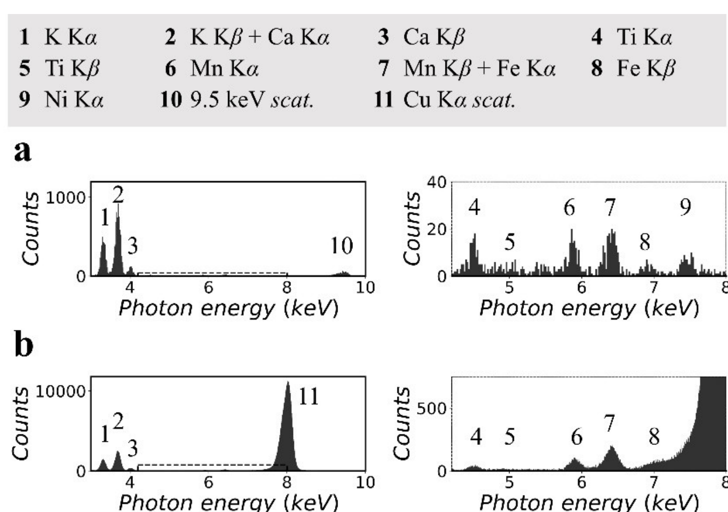


Figure 3-6. X-ray fluorescence spectra of CRM, NIST 1515, apple leaves. Original material was mixed into cellulose matrix at mass fraction of 30%. (a) measured in synchrotron polarized experiment, and (b) measured in laboratory unpolarized experiment. Details of spectra were enlarged and attached to right side. From Ref[35].

| | | | |
|---|---|---|---|
| **1** Cr K$\alpha$ | **2** Cr K$\beta$ | **3** Fe K$\alpha$ | **4** Co K$\alpha$ |
| **5** Co K$\beta$ | **6** 9.5 keV *scat.* | 7 Cu K$\alpha$ *scat.* | |

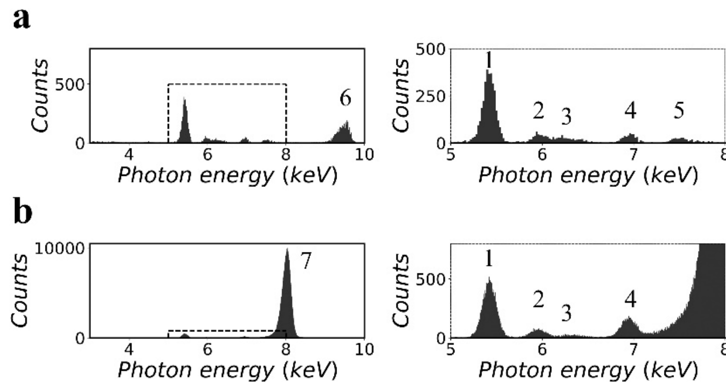


Figure 3-7. X-ray fluorescence of CRM JSAC 0615. (a) measured in synchrotron polarized experiment, and (b) measured in laboratory unpolarized experiment. Details of spectra are enlarged and attached on the right. From Ref[35].

### 3.4. Significance in antiscattering XRF analysis for large-area samples

As indicated by the XRF spectra of samples containing trace elements, the present synchrotron setup can contribute to not only full-field XRF imaging but also trace-element XRF spectroscopy analysis for large-area samples. In the conventional scheme of trace-element XRF spectroscopy analysis with polarized X-rays is as follows: illuminating a small probing area on the sample, opening a small active area on the detector, and arranging a large sample-to-detector distance. However, the probing area needs to be enlarged to study the elements dispersed in large-area samples and to visualize their spatial distribution by full-field XRF imaging. In this case, the sample-to-detector distance has to be increased greatly to ensure the detector is still roughly in the polarization direction with respect to every part on the sample. This is sometimes unacceptable owing to the size limitations of instruments or the strong absorption of low-energy fluorescence X-rays in a long air path. In the present study, as the radius of the capillaries is at the micron level, and the length of the capillaries, *i.e.*, the thickness of the collimator plate is 1 mm, the sample-to-detector distance becomes as short as 2 to 3 mm, making it easier for the analysis of low-Z elements.

In this work, the accumulation efficiency of the XRF spectra in the synchrotron polarized experiment was low. One reason was that the primary synchrotron beam was weakened owing to beam manipulation. More important, the capillaries on the collimator plate in this work had a small RLR. The radius of the capillaries was 3 μm, and the length of the capillaries was 1 mm. The resulting effective solid angle was only $2.8 \times 10^{-5}$ sr. Such a small RLR was designed for collecting X-rays in a small angular divergence with respect to the direction of polarization, but it certainly worsened the measurement efficiency as it blocked fluorescence X-rays in other directions. Nevertheless, when the present synchrotron setup is utilized solely for antiscattering XRF analysis, it is frequently unnecessary to use such a small RLR of capillaries. When the angular distribution of the scattering intensity has an invariant component around the direction of polarization, the SBR cannot be optimized infinitely by reducing the RLR of the capillaries ceaselessly. In other words, there exists a critical condition at which a further reduction in the RLR of the capillaries can no longer improve the SBR. This critical value of the RLR depends on the degree of polarization (DOP) of the primary X-rays. In an experiment, the RLR of the capillaries should be designed at this critical value so that it can collect X-rays as much as possible under the premise of the best achievable SBR. When the primary X-rays are not perfectly polarized, the critical value of the RLR is dependent on the DOP of the primary X-rays.

The calculation result here provides guidance for choosing an optimum collimator plate for a practical experiment to obtain the maximum counting rate under the premise of achieving the best SBR. The relation between the detected scattering intensity and the RLR of the capillaries under different DOP conditions were calculated. The calculation here only considered the differential cross section of coherent scattering and Compton scattering from an electron[63] because this physical process determines the fact that the angular distribution of the scattering intensity has a sharp minimum in the direction of polarization. In

the calculation, the primary X-ray energy was set as 9.53 keV. The detailed calculation procedure is as follows:

The calculation result is in the form of the cross section of scattering, including coherent scattering and Compton scattering, and is an average of the cross section of scattering from every point in the probing area on the sample. The average scattering cross section is denoted by $\bar{\sigma}_{scat}$. In addition, as the effective solid angle $\Omega$ of the capillaries determines the detectable fluorescence intensity, it is necessary to normalize $\bar{\sigma}_{scat}$ by $\Omega$. The resulting $\bar{\sigma}_{scat}/\Omega$ is considered to be inversely proportional to the signal-to-background ratio in the XRF spectra. It is worth noting that in an actual experiment, other factors including the atomic form factor, incoherent scattering function,[64] and absorption in the sample matrix should also be considered. However, when the radius-to-length of the capillaries is small enough, these factors have little influence on the final conclusion, and therefore they are not included in the calculation model for simplicity.

A *cartesian* coordinate system is introduced to describe the geometry in this problem. The primary X-rays propagate along the *z*-axis. For polarized X-rays, the polarization is along the *x*-axis. The observation direction of the scattering X-rays is described by two angles, $\theta$ and $\phi$, where $\theta$ is the polar angle between the *z*-axis and the observation direction, and $\phi$ is the azimuth angle between the *x*-axis and the projection of the observation direction in the *x-y* plane. The differential cross sections of scattering from an electron are given by

$$\left(\frac{d\sigma}{d\Omega}\right)_{coh} = r_e^2(1 - \sin^2\theta\cos^2\phi) \tag{3-2a}$$

and

$$\left(\frac{d\sigma}{d\Omega}\right)_{Comp} = r_e^2\left(\frac{k}{k_0}\right)^2 \frac{\left(\frac{k}{k_0} + \frac{k_0}{k} - 2\sin^2\theta\cos^2\phi\right)}{2}. \tag{3-2b}$$

where $(d\sigma/d\Omega)_{coh}$ denotes the differential cross section of coherent scattering, $(d\sigma/d\Omega)_{Comp}$ denotes the differential cross section of Compton scattering, $r_e$ denotes the classical electron radius and equals $2.82 \times 10^{-5}$ Å, and $k_0$ and $k$ denote the wave vectors of the primary X-rays and scattering X-rays, respectively. The ratio of $k$ and $k_0$ is given by

$$\frac{k}{k_0} = \frac{1}{1 + \frac{E_0}{m_e c^2}(1 - \cos\theta)}, \tag{3-3}$$

where $E_0$ denotes the photon energy of the primary X-rays, $m_e$ denotes the electron mass, and $c$ denotes the speed of light. It is noted that $k/k_0$ does not equal unity when $\theta = \pi/2$. Therefore, $(d\sigma/d\Omega)_{Comp}$ is not zero even when the observation direction is in the direction of polarization. On the other hand, as $k/k_0$ is dependent on $E_0$, this calculation relies on an assumed primary X-ray energy. Here, $E_0$ is set as 9.5 keV.

To clarify the role of the DOP, the primary X-ray beam is assumed to be a combination of two linearly polarized components: a parallel component and a perpendicular component. The polarization direction of the parallel component and the perpendicular component is parallel and perpendicular to the capillary axis of the collimator plate, respectively, as shown in Figure 3-8 and Figure 3-9. When the DOP of the primary X-ray beam is $p$, the percentage of the parallel component is $(1 + p)/2$, and the percentage of the perpendicular component is $(1 - p)/2$. The radius of the capillaries is $r$, and the length of the capillaries, *i.e.*, the thickness of the collimator plate, is $t$. For each capillary, the viewing area on the sample can be equivalently treated as a circular disk $S_1$ at one end of the capillary, and the corresponding active opening area on the detector can be equivalently treated as a circular disk $S_2$ at the other end. The radii of $S_1$ and $S_2$ are both $r$.

In the calculation, the cross section of scattering X-rays emitted from an area element $dS_1$ at $P_1$ on $S_1$ and detected by an area element $dS_2$ at $P_2$ on $S_2$ is first considered. The positions of $P_1$ and $P_2$ are described by polar coordinates for $S_1$ and $S_2$, which are $(\rho_1, \alpha_1)$ and $(\rho_2, \alpha_2)$, respectively. Here, $\rho_i$ is

defined as the length of $\overrightarrow{O_iP_i}$, and $\alpha_i$ is defined as the rotation angle from the $z$-axis to $\overrightarrow{O_iP_i}$, where $i = 1, 2$. The corresponding area element is

$$dS_1 = \rho_1 \, d\rho_1 \, d\alpha_1, \tag{3-4a}$$

and

$$dS_2 = \rho_2 \, d\rho_2 \, d\alpha_2. \tag{3-4b}$$

In the calculation of the parallel components, as shown in Fig. S3, for the scattering X-rays from $P_1$ to $P_2$, the observation direction in the *cartesian* coordinate system is described as

$$x = t, \tag{3-5a}$$

$$y = \rho_2 \, sin \, \alpha_2 - \rho_1 \, sin \, \alpha_1, \tag{3-5b}$$

$$z = \rho_2 \, cos \, \alpha_2 - \rho_1 \, cos \, \alpha_1. \tag{3-5c}$$

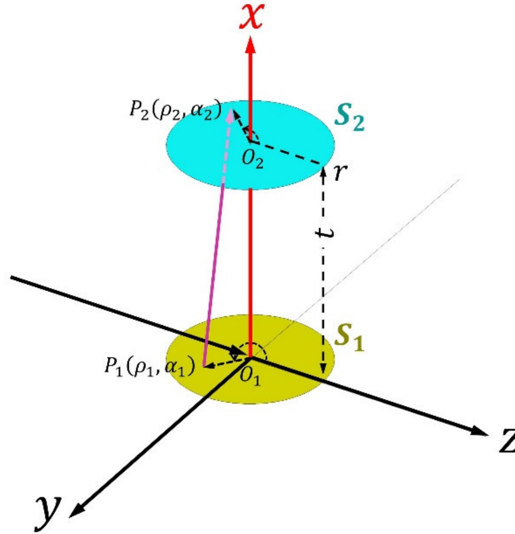


Figure 3-8. Calculation of parallel components in primary X-ray beam. Polarization is parallel to capillary axis of collimator plate. From Ref[35].

Thus, the corresponding polar angle $\theta$ and azimuth angle $\phi$ of the observation direction are

$$\theta = arccos \frac{z}{\sqrt{x^2 + y^2 + z^2}} = arccos \, \frac{\rho_2 \, cos \, \alpha_2 - \rho_1 \, cos \, \alpha_1}{\sqrt{t^2 + \rho_1^2 + \rho_2^2 - 2\rho_1\rho_2 \, cos(\alpha_2 - \alpha_1)}} \tag{3-6a}$$

and

$$\phi = arctan \frac{y}{x} = arctan \frac{\rho_2 \, sin \, \alpha_2 - \rho_1 \, sin \, \alpha_1}{t}, \tag{3-6b}$$

and the corresponding trigonometric functions that will be used in the following calculations include

$$\sin \theta = \frac{\sqrt{x^2 + y^2}}{\sqrt{x^2 + y^2 + z^2}} = \frac{\sqrt{t^2 + (\rho_2 \, sin \, \alpha_2 - \rho_1 \, sin \, \alpha_1)^2}}{\sqrt{t^2 + \rho_1^2 + \rho_2^2 - 2\rho_1\rho_2 \, cos(\alpha_2 - \alpha_1)}} \tag{3-7a}$$

and

$$\cos\phi = \frac{x}{\sqrt{x^2+y^2}} = \frac{t}{\sqrt{t^2+(\rho_2 \sin\alpha_2 - \rho_1 \sin\alpha_1)^2}}. \tag{3-7a}$$

The corresponding solid angle for collecting the scattering X-rays in this observation direction is

$$d\Omega = \sin\theta\, d\theta\, d\phi. \tag{3-8}$$

Therefore, the cross section of scattering X-rays that are emitted from $dS_1$ and detected by the entire $S_2$ is

$$\sigma_{coh,\ dS_1} = \iint_{S_2} \left(\frac{d\sigma}{d\Omega}\right)_{coh} (\theta,\phi) \cdot d\Omega(\theta,\phi) \tag{3-9a}$$

and

$$\sigma_{Comp,\ dS_1} = \iint_{S_2} \left(\frac{d\sigma}{d\Omega}\right)_{Comp} (\theta,\phi) \cdot d\Omega(\theta,\phi). \tag{3-9b}$$

As $S_2$ is more easily described by $(\rho_2, \alpha_2)$ rather than $(\theta, \phi)$, it is necessary to find a *Jacobian* matrix to relate them. The relation is given as

$$d\theta\, d\phi = \left\| \begin{matrix} \frac{\partial\theta}{\partial\alpha_2} & \frac{\partial\theta}{\partial\rho_2} \\ \frac{\partial\phi}{\partial\alpha_2} & \frac{\partial\phi}{\partial\rho_2} \end{matrix} \right\| d\alpha_2\, d\rho_2 \tag{3-10}$$

$$= \frac{t\rho_2}{[t^2+\rho_1^2+\rho_2^2-2\rho_1\rho_2 \cos(\alpha_2-\alpha_1)]\sqrt{t^2+(\rho_2 \sin\alpha_2 - \rho_1 \sin\alpha_1)^2}} d\alpha_2\, d\rho_2.$$

Then, the average cross section of the scattering from every point in the probing area $S_1$ on the sample is

$$\bar{\sigma}_{coh} = \frac{1}{S_1} \iint_{S_1} \sigma_{coh,\ dS_1} \cdot dS_1 \tag{3-11a}$$

and

$$\bar{\sigma}_{Comp} = \frac{1}{S_1} \iint_{S_1} \sigma_{Comp,\ dS_1} \cdot dS_1. \tag{3-11b}$$

Consequently, for the parallel component in the primary X-ray beam, by combining the equations in (3-1) and from (3-4) to (3-11), the final expression for the average cross section of coherent scattering is

$$\bar{\sigma}_{coh} = \frac{r_e^2}{\pi r^2} \int_0^r d\rho_1 \int_0^{2\pi} d\alpha_1 \int_0^r d\rho_2 \int_0^{2\pi} d\alpha_2\, \frac{t\rho_1\rho_2[\rho_1^2+\rho_2^2-2\rho_1\rho_2 \cos(\alpha_2-\alpha_1)]}{[t^2+\rho_1^2+\rho_2^2-2\rho_1\rho_2 \cos(\alpha_2-\alpha_1)]^{\frac{5}{2}}}, \tag{3-12a}$$

and the final expression for the average cross section of Compton scattering is

$$\bar{\sigma}_{Comp} = \frac{r_e^2}{\pi r^2} \int_0^r d\rho_1 \int_0^{2\pi} d\alpha_1 \int_0^r d\rho_2 \int_0^{2\pi} d\alpha_2 \tag{3-12b}$$

$$\times \left(\frac{k}{k_0}\right)^2 \left(\frac{k}{2k_0} + \frac{k_0}{2k} - \frac{t^2}{t^2 + \rho_1^2 + \rho_2^2 - 2\rho_1\rho_2 \cos(\alpha_2 - \alpha_1)}\right)$$

$$\times \frac{t\rho_1\rho_2}{[R^2 + \rho_1^2 + \rho_2^2 - 2\rho_1\rho_2 \cos(\alpha_2 - \alpha_1)]^{\frac{3}{2}}}.$$

In a similar way, the average scattering cross sections for the perpendicular component in the primary X-ray beam are calculated. As shown in Fig. S4, the coordinates of the observation direction for the scattering X-rays from $P_1$ to $P_2$ are changed:

$$x' = \rho_2 \sin\alpha_2 - \rho_1 \sin\alpha_1, \tag{3-13a}$$

$$y' = t, \tag{3-13b}$$

$$z' = \rho_2 \cos\alpha_2 - \rho_1 \cos\alpha_1. \tag{3-13c}$$

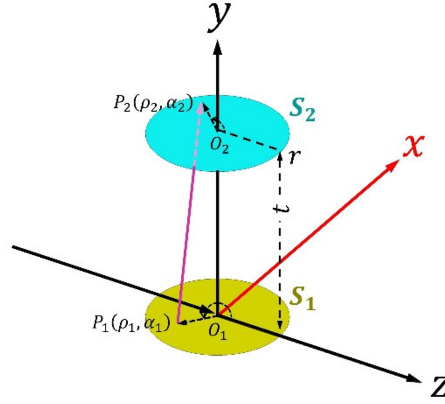


Figure 3-9. Calculation of perpendicular components in primary X-ray beam. Polarization is perpendicular to capillary axis of collimator plate. From Ref[35].

By replacing the coordinates $(x, y, z)$ in equations (S5) to (S10), the final expression for the average cross section of coherent scattering for the perpendicular component is

$$\bar{\sigma}'_{coh} = \frac{r_e^2}{\pi r^2}\int_0^r d\rho_1 \int_0^{2\pi} d\alpha_1 \int_0^r d\rho_2 \int_0^{2\pi} d\alpha_2 \, \frac{t\rho_1\rho_2[t^2 + (\rho_2 \cos\alpha_2 - \rho_1 \cos\alpha_1)^2]}{[t^2 + \rho_1^2 + \rho_2^2 - 2\rho_1\rho_2 \cos(\alpha_2 - \alpha_1)]^{\frac{5}{2}}}, \tag{3-14a}$$

and the final expression for the average cross section of Compton scattering for the perpendicular component is

$$\bar{\sigma}'_{Comp} = \frac{r_e^2}{\pi r^2}\int_0^r d\rho_1 \int_0^{2\pi} d\alpha_1 \int_0^r d\rho_2 \int_0^{2\pi} d\alpha_2 \tag{3-14b}$$

$$\times \left(\frac{k}{k_0}\right)^2 \left(\frac{k}{2k_0} + \frac{k_0}{2k} - \frac{(\rho_2 \sin\alpha_2 - \rho_1 \sin\alpha_1)^2}{t^2 + \rho_1^2 + \rho_2^2 - 2\rho_1\rho_2 \cos(\alpha_2 - \alpha_1)}\right)$$

$$\times \frac{t\rho_1\rho_2}{[t^2 + \rho_1^2 + \rho_2^2 - 2\rho_1\rho_2 \cos(\alpha_2 - \alpha_1)]^{\frac{3}{2}}}.$$

Finally, combining the coherent scattering cross section and the Compton scattering cross section for the parallel component and the perpendicular component, the final obtained average scattering cross section is

$$\bar{\sigma} = \frac{1+p}{2}\left(\bar{\sigma}_{coh} + \bar{\sigma}_{Comp}\right) + \frac{1-p}{2}\left(\bar{\sigma}'_{coh} + \bar{\sigma}'_{Comp}\right). \quad (3\text{-}15)$$

In the meantime, the effective solid angle $\Omega$ of the capillaries is given by

$$\begin{aligned}\Omega &= \frac{1}{S_1}\iint_{S_2} d\Omega \\ &= \frac{1}{\pi r^2}\int_0^r d\rho_1 \int_0^{2\pi} d\alpha_1 \int_0^r d\rho_2 \int_0^{2\pi} d\alpha_2 \frac{t\rho_1\rho_2}{[t^2 + \rho_1^2 + \rho_2^2 - 2\rho_1\rho_2 \cos(\alpha_2 - \alpha_1)]^{\frac{3}{2}}}.\end{aligned} \quad (3\text{-}16)$$

In this work, the integrations in (3-12), (3-13), and (3-15) are numerically calculated by C#. The final obtained value of $\bar{\sigma}/\Omega$ is plotted with respect to the radius-to-length ratio of the capillaries and the DOP of the primary X-rays in Fig. 3-10. In addition, it is noticed that $\bar{\sigma} \propto \Omega^2$ when $r/t$ is small but still larger than the critical value in Figure 3-10. The calculation result is shown in the color map in Figure 3-10. The *x*-axis was plotted in log scale since it is the RLR of the capillaries. Here, *r* denotes the capillary radius, and *t* denotes the thickness of the collimator plate, *i.e.*, the capillary length.

The *y*-axis was plotted on a square-root scale since it is the DOP of the primary X-rays. The intensity in the color map indicates the detectable average scattering cross section $\bar{\sigma}_{scat}$, which was subsequently normalized by the effective solid angle $\Omega$. For the same sample, as the detectable fluorescence intensity is proportional to the effective solid angle $\Omega$, $\bar{\sigma}_{scat}/\Omega$ was considered to be inversely proportional to the SBR in the XRF spectra. It is worth noting that in an actual experiment, other factors including the atomic form factor, incoherent scattering function, and absorption in the sample matrix should also be considered. However, when $r/t$ is small, these factors do not significantly distort the contour of the color map in the same experiment. Therefore, they were not included in the calculation model for simplicity.

As indicated in Figure 3-10, at a specific DOP, the reduction of $\bar{\sigma}_{scat}/\Omega$ terminates at a critical value of $r/t$. This critical value depends on the DOP. For example, when the thickness of the collimator plate is 1 mm, when the DOP is 0.9, 0.95, 0.99, and 0.999, the corresponding critical radii of the capillaries are 30 µm, 25 µm, 14 µm, and 6 µm, respectively. In this way, Figure 3-10 provides guidance on choosing the optimum collimator plate for a practical experiment when the DOP of the primary X-rays is known.

In addition, it is noted that even when the primary X-rays are perfectly polarized, the reduction of $\bar{\sigma}_{scat}/\Omega$ still terminates at $r/t$ = 0.003. This relates to the fact that the differential cross section of Compton scattering does not vanish in the direction of polarization. The value of 0.003 is the smallest RLR of the capillaries in the present polarization-collimator scheme. The experiments in this work verified that trace elements of a few ppm can be detected even when using capillaries with the smallest RLR.

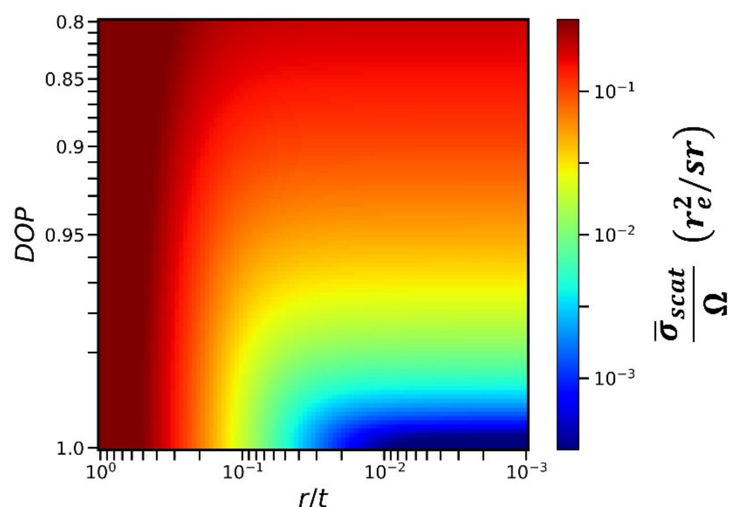


Figure 3-10. Average scattering cross section $\bar{\sigma}_{scat}$ with respect to DOP of primary X-rays and ratio of capillary radius $r$ to collimator plate thickness $t$. Scattering cross section is in units of $r_e^2$, where $r_e$ denotes classical electron radius and equals $2.82 \times 10^{-5}$ Å, and is normalized by effective solid angle Ω of capillaries. From Ref[35].

In this work, the probing area on the sample was 13.3 × 13.3 mm, making it convenient to survey trace elements dispersed in large-area environmental samples and industrial products. Meanwhile, the sample-to-detector distance was always approximately 3 mm, which was independent of the probing area size. Such a small distance reduces the absorption of low-energy fluorescence X-rays in air and is consequently favorable for the detection of low-Z elements such as sulfur and chlorine.

On the other hand, if a collimator plate is not utilized, the optimum sample-to-detector distance becomes much longer. For example, assuming that the probing area on the sample is Φ 10 mm and the active area on the detector is Φ 6 mm, in order to achieve a similar $\bar{\sigma}_{scat}/\Omega$ value as the critical condition in the collimator-plate experiment, the necessary sample-to-detector distance is 16 cm, 18 cm, 32 cm, and 70 cm when the DOP of the primary X-rays is 0.9, 0.95, 0.99, and 0.999, respectively. The advantage of using a collimator plate is clear.

In order to clarify how much the scattering intensity can be reduced by the present polarization-collimation experimental scheme, a set of XRF spectra was generated using the Monte Carlo simulation software XMI-MSIM[65]. In the simulation, the sample was a cellulose pellet that included 100 ppm iron. The geometrical parameters were set the same as in the experiments in this work, either for the model of the synchrotron polarized experiment or for the model of the laboratory unpolarized experiment. For ease of comparison, in the two models, the primary X-ray energy was set the same at 9.53 keV, and the detector sensor thickness was set the same at 500 μm. The final simulated XRF spectra are included in the Supporting Information. It was found that when using polarized primary X-rays and the collimator plate in this work, the SBR improves by more than 10 times when the DOP is 0.90, 30 times when the DOP is 0.95, and 60 times when the DOP is 0.99.

The simulated X-ray fluorescence spectra were generated by XMI-MSIM, which is an open-source tool developed by Tom Schoonjans, Laszlo Vincze and their co-workers. The software uses fundamental parameters in X-ray physics and Monto Carlo algorithms.

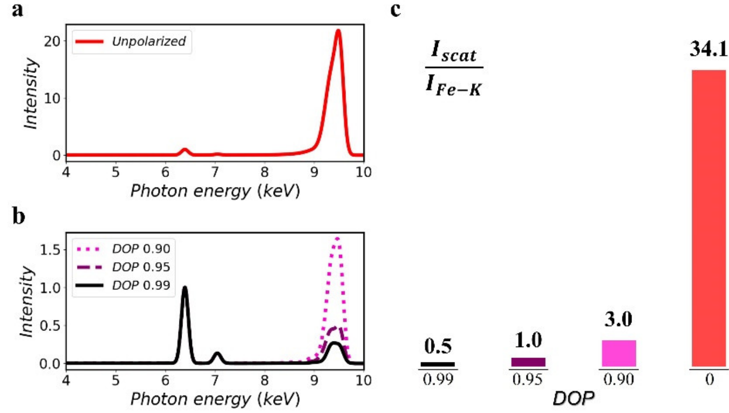


Figure 3-11. Simulated XRF spectra. Sample was cellulose pellet that included 100 ppm iron. Model for (a) resembles laboratory unpolarized experiment in this work, and model for (b) resembles synchrotron polarized experiment. For ease of comparison, primary X-ray energy in two models was set the same at 9.53 keV, and detector sensor thickness was set the same at 500 μm. (c) summarizes ratio of scattering intensity to iron K-line intensity in all spectra. Spectra in (a) are labeled as DOP = 0. From Ref[35].

In the simulation, the sample was a cellulose pellet that included 100 ppm iron. The density of the cellulose matrix was 1.5 g/cm$^3$, and the thickness was 1 cm. There were two simulation models. In the model for Figure 3-11(a), the geometry parameters were set the same as in the laboratory unpolarized experiment in this work. The primary X-rays were set as totally unpolarized for simplicity. In the model for Figure 3-11(b), the geometry parameters were set the same as in the synchrotron polarized experiments. The radius-to-length ratio of collimation was 0.003. The DOP of the primary X-rays was set as 0.90, 0.95, and 0.99. For ease of comparison, in the two models, the primary X-ray energy was set at 9.53 keV to eliminate the influence of energy-dependent photon-matter interaction cross sections. The detector sensor thickness was set at 500 μm to eliminate the influence of the detection efficiency. In all spectra, the intensity on the $y$-axis was normalized by the peak height of iron K$\alpha$ so that the huge difference of scattering intensity in the two models could be directly visualized. The ratio of the scattering intensity to the iron K-line intensity, which is inversely proportional to the signal-to-background ratio, is summarized and plotted in Figure 3-11(c). Clearly, the collimator plate makes a great contribution to reducing the scattering background, especially when the DOP of the primary X-rays is high.

Improving the SBR in XRF spectra makes it easy to analyze trace elements. One major concern is the minimum detectable limit (MDL). This limit is determined by the statistical fluctuations of the background beneath a given XRF peak. Therefore, the accumulated counts of the background play an important role, and the signal-to-noise ratio (SNR) is more crucial than the SBR in this discussion. Approximate equations of the SNR and the MDL are given by

$$SNR = \sqrt{I_0 T}\frac{S}{\sqrt{B}} \tag{3-17}$$

and

$$MDL = C\frac{1}{\sqrt{I_0 T}}\frac{\sqrt{B}}{S}, \tag{3-18}$$

where $C$ is a constant for a specific element, $I_0$ is the intensity of the primary X-rays, $T$ is the accumulation time, $S$ denotes the detected XRF signals, and $B$ denotes the detected background which is mostly contributed from and proportional to the detected scattering X-rays. When polarized primary X-rays and a collimator plate are utilized, $S$ is proportional to the effective solid angle $\Omega$ and $B$ is approximately proportional to $\Omega^2$ when $\Omega$ is small because of the angular distribution of scattering X-rays (See Section II in the Supporting Information). Consequently, when $I_0$ and $T$ are fixed, the MDL remains unchanged even

if $\Omega$ is reduced and the SBR is improved. However, in the case where the primary X-rays are very strong and the XRF detector is easily saturated by the strong scattering X-rays, the intensity of the primary X-rays must be weakened to avoid saturation. Thus, the available $I_0$ is limited by the intensity of the scattering X-rays, i.e. $I_0 \propto \Omega^{-2}$. In this case, within the same accumulation time $T$, the MDL is proportional to $\Omega$, and it can be improved by reducing $\Omega$. This relation also applies to conventional polarized XRF experiments without a collimator plate[66].

For example, in this work, the $I_0$ in the laboratory experiment was on the order of $10^8$ counts per second. The corresponding $T$ was $600$ seconds and $\Omega$ was $9.4 \times 10^{-4}$ sr. Meanwhile, the $I_0$ in the synchrotron experiment was on the order of $10^9$ counts per second. The corresponding $T$ was about $10^4$ seconds and $\Omega$ was $2.8 \times 10^{-5}$ sr. Such a small $\Omega$ significantly reduced the accumulation efficiency of the XRF spectra. As a result, the signal counts obtained in the synchrotron experiment was even smaller than those obtained in the laboratory experiment with considering the lower X-ray detection efficiency of the CCD sensor. On the other hand, nowadays, the $I_0$ in most 3rd generation synchrotron facilities exceeds $10^{11}$ counts per second, whereas the saturation of most XRF detectors is below $10^6$. For this reason, the strong primary X-rays are frequently weakened and wasted in trace-element analysis to avoid the saturation of XRF detectors. In this case, utilizing the collimator plate is adequate to fully use the strong primary X-rays and to improve the MDL.

The present experimental scheme can work in either vacuum or air. In this work, the sample-to-detector distance was 2~3 mm. It can become up to tens of millimeters for the ease of sample alignment. When the primary X-rays are strong enough, the present experimental scheme can be combined with the total-reflection XRF (TXRT) technique to improve the MDL further. It can also apply to handheld XRF setups if a wide polarized X-ray beam is produced with using Soller slits and a scatterer. When the incident particles are electrons rather than polarized X-rays, the background in the spectra is mostly bremsstrahlung X-rays of which the intensity has no sharp minimum in the angular distribution. Thus, the use a collimator plate in electron-excited energy dispersive X-ray spectroscopy is unnecessary. The collimator plate can be replaced by other X-ray collimation components such as 2D Soller slits. The detector can be the CCD sensor, a silicon drift detector, or any other XRF detector. However, a large active area on the detector sensor is essential. In this work, we used the CCD sensor for its large sensor area of greater than 170 $mm^2$, while such a large area is still uncommon for ordinary XRF detectors.

The present experimental scheme is suitable for many practical applications such as the survey of elemental impurities in pharmaceuticals and heavy metal contaminations in soils[67,68], agriculture products[69], and marine products[70]. The technique of XRF analysis is adopted for easy sample preparation and rapid sample screening. As the concentration of the target element is frequently below 1 ppm and they are dispersed in sample matrixes, utilizing strong and polarized synchrotron X-rays is necessary. In addition, as the distribution of the trace elements in the sample matrixes is frequently inhomogeneous, it is better to probe a large area on samples to eliminate the influence of inhomogeneity.

### 3.5. Extension to trace-element chemical-state imaging

Reducing the scattering background has a wide range of benefits in many XRF techniques, especially when investigating diluted/trace elements. One instance is XAFS imaging[71,72]. If the target element is present in small amounts and is diluted in a thick matrix, measuring its fluorescence intensity is much preferable than measuring the transmission intensity of the thick matrix. In this case, the full-field XRF imaging scheme can be adopted while the primary x-ray energy is scanned around the absorption edge of the target element. In previous studies, the instruments were arranged as Layout C, as shown in Table I, to image a large sample area. The atomic-level structure and the chemical state of the target element could be successfully resolved, even if the detector was a conventional CCD camera with no x-ray energy resolution[39,40]. However, this layout remains unsuitable for diluted/trace element analysis, even though a color x-ray camera can separate scattering and fluorescence x-rays with different energy channels[73]. This is because the primary x-ray energy is around the absorption edge of the target element, which is too close to the fluorescence x-ray energy. Thus, the weak fluorescence signals are disturbed by the high scattering counts at the higher-energy side. For this reason, it is necessary to reduce the scattering background by using the linear polarization of synchrotron radiation. Although our related experiments have shown that using Layout B, as shown in Table I, without beam expanding can also produce square-centimeter XRF images by acquiring and connecting many thin slices while scanning the sample stage in one direction, it was still

impossible to perform simultaneous XAFS imaging with the full field. In this study, this obstacle was overcome by expanding the synchrotron beam in the direction perpendicular to the polarization with a simple asymmetric-cut crystal, whereas an optional symmetric crystal can be used to fix the path of the size-expanded synchrotron beam during energy scanning. Besides XAFS imaging, the present setup may also have other applications.

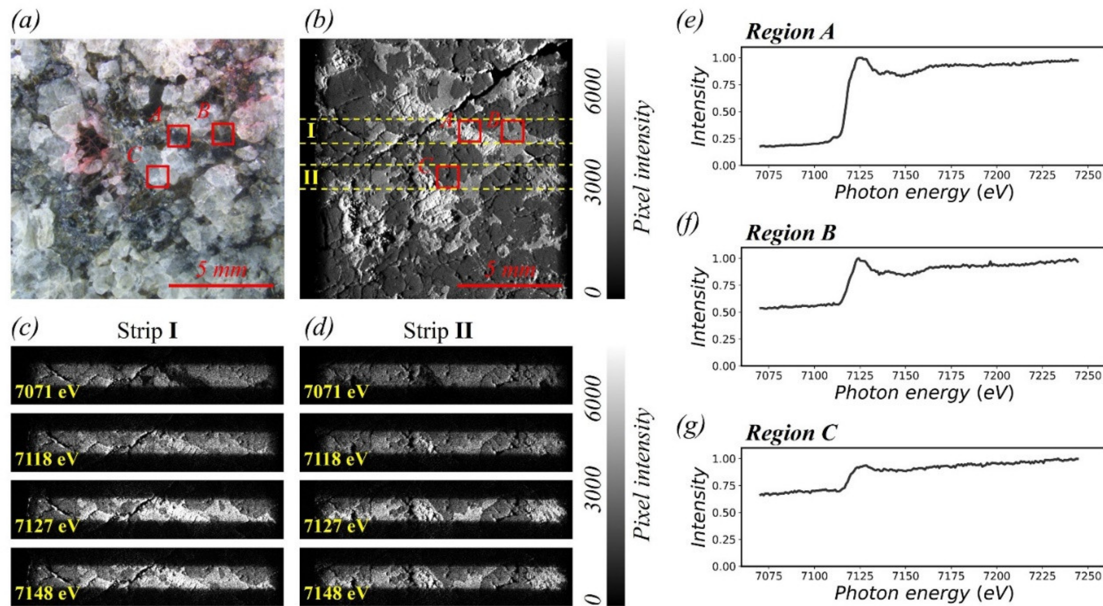


Figure 3-12. (a) Photo of the gabbroic rock sample. (b) Black-and-white XRF image. It is connected from 141 thin strips. (c) and (d) are XAFS imaging scan of Strip I and II, respectively. (e), (f), and (g) are XAFS spectra of Region A, B, and C, respectively. From Ref[46].

The experiment in this section was carried out in Beamline NW2A, Advanced Ring, Photon Factory, KEK, Japan. As the beamline utilizes a horizontal undulator, the synchrotron beam is narrow in the vertical direction, and its linear polarization is horizontal. The gabbroic rock sample and a conventional CCD camera were mounted according to Layout B in Table I: the rock surface stood vertically, and the camera sensor was perpendicular to polarization. The synchrotron beam was cut to 0.6 (H) × 1.0 (V) mm. In the horizontal place, the rock surface was at an angle of 3˚ to the primary beam, so that a 1-mm-high strip on the rock surface could be illuminated. The gap width between the rock surface and camera sensor was ~3 mm. The same 1-mm-thick collimator plate was inserted in the gap.

The CCD camera in this experiment was Hamamatsu C4742, which used the same sensor type of CCD47-10 produced by e2V. Although the camera can resolve X-ray photon energy if it is operated in single-photon-counting mode, this time it worked in a general accumulation mode to capture black-and-white X-ray images.

Limited by the beam size, the experimental setup could acquire only a 1-mm-wide strip of XRF image in one exposure. The exposure time was 40 s. To record a full image, repeated exposures were performed while the sample was moved in the vertical direction with a step length of 100 µm. The XRF image in Figure 3-12 was merged from 141 thin strips. The primary X-ray energy in this measurement was 7,400 eV. In this condition, iron fluorescence is much stronger than calcium fluorescence, therefore the bright parts in the image correspond to iron-rick structures in the rock, which appear to be black in the photo. To study the chemical state of iron in Region A, B, and C, Strip I and II were selected successively for XAFS imaging. The primary X-ray energy was scanned around the absorption edge of iron, i.e., 7,112 eV. Some key frames are displayed in Figure 3-12 (c) and (d). Clearly, the brightness of some structures changes with energy. For example, the brightness profiles of Region A, B, and C are plotted in Figure 3-12 (e), (f), and (g), respectively. In three regions, the jump ratio at iron absorption edge is different. This owes to the difference of iron concentration, which is corroborated by the localized XRF spectra of Region A, B, and C in Figure 3-2. On the other hand, the brightness profiles can be processed to XAFS spectra of iron, after

subtracting the background from the matrix and other elements. However, a preferable approach is to separate them directly with using an energy-dispersive X-ray camera, which can be realized by operating the present conventional CCD camera in single-photon-counting mode. Nevertheless, it should be noted that, when diluted/trace elements are of interest, removing scattering X-rays by using the linear polarization of synchrotron radiation is always necessary, no matter whether the X-ray camera has energy resolution or not. The reason is that the scattering X-ray energy is close to fluorescence X-ray energy so that the influence of strong scattering cannot be eliminated by energy dispersion.

Figure 3-12 was processed based on Prof. Kenji Sakurai's previous experiment.

### 3.6. Summary

In conclusion, one asymmetric-cut crystal was used to expand a thin synchrotron beam in the direction perpendicular to the polarization. Thus, full-field XRF imaging was performed with a size-expanded polarized synchrotron beam. High-quality XRF images were obtained with a parallel-optics collimator plate and a conventional CCD camera operated in single-photon-counting mode. The sample imaging area was $13 \times 13$ mm$^2$, consisting of more than one million pixels. The spatial resolution was up to 18 μm and the energy resolution was 150 eV at Mn K$\alpha$. More importantly, the technique took full advantage of the linear polarization of synchrotron radiation to remove the scattering background in color XRF imaging. This is important for the investigation of diluted/trace elements. As the technique adopts a stationary measurement scheme, it will have many attractive extensions, such as full-field XAFS imaging to study the chemical state of diluted/trace elements in inhomogeneous natural samples.

On the other hand, the present experimental scheme remains attractive enough in antiscattering XRF analysis for large-area samples when elemental images are not required. The collimator plate inserted between the sample and the detector can optimize the SBR in the XRF spectra by tens of times when the primary X-rays have a high DOP. The probing area on the sample was as large as $13.3 \times 13.3$ mm, making it convenient to survey trace elements dispersed in large-area environmental samples and industrial products. The sample-to-detector distance was as short as 3 mm, making the instruments compact and applicable to low-Z elements. The present polarization-collimator experimental scheme can exhibit the maximum potential if it is combined with a strong and highly polarized synchrotron radiation.

## Chapter 4. X-ray fluorescence movie imaging for visualizing chemical diffusion

*Portions of this section were adapted with permission from W. Zhao and K. Sakurai, ACS Omega 2, 4363 (2017)[74] Copyright (2017) by American Chemical Society and W. Zhao and K. Sakurai, J. Synchrotron Radiat. 26, 230 (2019)[33] Copyright (2019) by IUCr Jounrals.*

Nowadays XRF imaging has been widely utilized to study the stable spatial distribution of chemical elements in samples. However, in many samples, the distribution of chemical elements constantly changes due to diffusion. This chemical diffusion process may relate to the nature of chemical reaction, material formation, segregation/aggregation of particles, and even complicated life activities such as coagulation, muscle contraction, and neuron dynamics. Therefore, it is of great importance to record the entire process of chemical diffusion by taking many XRF images quickly and combing all images into one XRF movie. On this basis, *in operando* chemical element analysis on an ongoing reaction also becomes possible.

In the conventional scheme of scanning-type XRF imaging, different parts in a sample are not measured simultaneously. Thus, it only measures stable samples and it is unsuitable for time-dependent analysis on samples in reaction. On the other hand, full-field XRF imaging can be upgraded into movie imaging easily if the measurement time for every image is quick enough, i.e., time resolution is short enough to capture the changing process of the sample. However, such trials of movie imaging remain rare until today, even for experienced researchers of full-field XRF imaging. Probably this is due to the difficulty of coordinating chemical reaction and the sample cell with the XRF imaging setup. Our lab has a long tradition of taking XRF movies on various reactions. In recent years, the advent of X-ray camera-snapshot imaging endowed the movie with spectroscopic resolvability for recording multi-element reactions.

At present, the XRF movie imaging technique still suffers from problems of limited spatial resolution, which is tens of microns, and temporal resolution, which is tens of seconds. In the future, such problems could be solved with using brilliant synchrotron X rays and advanced X-ray optical components. On the other hand, simple instruments like laboratory X-ray tubes and micro pinhole may still be preferred when the diffusion rate is slow and when the scale of reaction is large. Depending on the condition of target reaction, the instruments of XRF movie imaging should be carefully chosen, sometimes for high resolution and sometimes for easy access to most researchers and workers.

On the other hand, people may take a movie in visible light for recording the full process of a chemical reaction. However, generally the movie taken in visible light cannot reveal the element composition in the reaction. One may more or less infer the element information by looking at the color in appearance, but the relation between the color and the corresponding elements is not reliable enough. In contrast, the color of fluorescence X-rays from the sample is characteristic to chemical elements. Therefore, a movie of a continuous series of XRF images may become a powerful tool for exploring multi-element reactions such as ion exchange, composition segregation, selective precipitation and the formation of chemical-gradient materials.

In this chapter, two applications of XRF movie imaging were demonstrated. First, the gradual chemical diffusion in chemical garden was recorded with using a laboratory X-ray tube and the conventional CCD camera. Second, the rapid growth of zinc dendrites during electro-deposition was recorded using synchrotron X-rays (BL-14B, Photon Factory, KEK) and the sCMOS camera. In the future, the XRF movie imaging technique can also be applied to reveal the mystery of some fascinating chemical reactions, such as the Belousov-Zhabotinsky reaction and the growth of the Traube cell. In the field of materials science, it can be used for inspecting high-temperature diffusion at electrodes and in soldering materials. Even more, with further instrument optimization, the technique may also be applied to some physiology research, such as the role of calcium ions in the coagulation process and the transmembrane transportation of chlorine, potassium, calcium ions in neural circuits.

### 4.1. Gradual chemical diffusion in a chemical garden

#### 4.1.1. Introduction of chemical garden

Chemical garden is a famous chemical phenomenon. The reaction is generally started by seeding a soluble metal salt crystal into sodium silicate solution. When the crystal starts to dissolve, it is immediately enveloped by a semipermeable membrane which precipitates at the interface of the internal metal salt solution and the external silicate solution. The continuous dissolution of the metal salt increases the osmotic

pressure of internal solutions, driving external water molecules to enter the envelop continuously through the membrane. As the internal water pressure increases, the membrane envelop expands, and finally it ruptures at its weakest point, ejecting a fluid of metal salt solution into the external sodium silicate solution. Again the fluid is immediately trapped by a new envelop which precipitates at the interface of two solutions. This envelop precipitation-rupture process is ceaselessly repeated, resulting in a continuous growth of membrane tubules in the solution. Because the metal salt solution is less dense than the sodium silicate solution, the flow direction of the ejected fluids is generally forced to be upward by the influence of buoyancy. Therefore, the direction of tubular growth is upward as well.

The chemical garden phenomenon was firstly discovered by Johann Glauber in 1646. At that time, it inspired a broad interest in discussing the original form of life, because its growth regime and plant-like tubular shape resemble some organisms. In the subsequent three centuries, its self-organized inorganic semipermeable membrane was frequently associated with biological membrane[75]. However, as people accumulated more and more knowledge on biology and biochemistry, this analogy between chemical garden and organism life was finally in decline in the mid-20th century. After that, except for its impressive fascinating appearance, the scientific significance of chemical garden did not cause much interest until 1980.[76] Nowadays, much modern research on chemical garden has been conducted, and many types of chemical garden reactions have been systematically studied. The terminology of chemical garden has been extended to represent a wide range of chemical reactions, in which a semipermeable membrane precipitates at the interface of two different aqueous solutions and a steep transmembrane chemical gradient automatically forms.[77] In these modern research, the reactants are quite variable. The general formation mechanism of chemical garden has been clarified[78]. Different growth regimes have been reported[79] and an oscillation growth model has been established[80,81]. The precipitated tubular structures have been comprehensively characterized in many aspects, including the morphology[82,83], hierarcharical nanostructure[84], composition gradient[85–87], crystallography[88], porosity, magnetism, catalytic[89,90], etc. Some experiments were conducted in microgravity to discuss the fluid convection which is free of buoyancy[91,92], and some experiments were conducted in a magnetic field to influence the ions in fluid and to induce 3D morphological chirality[93,94]. The gradually deepened understanding of chemical garden would certainly lead to fruitful achievements in different fields. It has been found that the chemical garden phenomenon also occurs in submarine vents[95] and in the process of cement hydration[96] and metal corrosion[97]. It has been reported that the chemical garden reaction could be applied to the field of nanowires[98], fuel cells[99], cytocompatible biomaterials[100] and biomineralizations[101]. Since so much progress has been made in the past forty years, in 2015 it was suggested to introduce a new terminology "*chemobrionics*" to represent the field of all these modern research on chemical garden[77]. Moreover, much future research on synthesizing new materials and fabricating new composites via the chemical garden route is expectable.

The modern research on chemical garden provides much observation detail and scientific insight compared with the early-stage naturalistic surveys centuries ago. This is mainly due to the advent of many powerful characterization techniques, such as scanning electron microscopy, transmission electron microscopy (TEM), energy dispersive spectroscopy (EDS), X-ray diffraction (XRD), themgravimetric analysis (TGA) and Raman spectroscopy. However, till now most of these characterization techniques can only analyze the final precipitated products of chemical garden as the specimen, which must be firstly isolated from the solution. As a result, it would be extremely troublesome and probably sometimes unreliable to reveal the stagewise development of precipitated tubules. Although Mach-Zehnder interferometry[78] was once used to observe the formation of chemical garden, still the most general method is to observe the appearance change by human eyes or an optical microscopy. This method can describe the obvious morphological change during the tubular growth. Nevertheless, it may not be effective to study the gradual chemical diffusion and precipitation during the subsequent aging process. More importantly, this method cannot reveal the nature of element species. In order to synthesize new materials via the chemical garden route, it will be unavoidable to introduce two or more species of metal ions in one chemical garden reaction. Therefore, it is necessary to record the whole process of spatiotemporal diffusion and precipitation of different elements in the same reaction. As a consequence, a new realtime characterization technique is needed.

Full-field X-ray fluorescence (XRF) imaging is a powerful technique to study the spatial distribution of elements in materials. In 2003, its time-resolved version, sometimes named as XRF movie, has been utilized to visualize the chemical diffusion dominated by an ion-exchange resin. The subsequent development of X-ray detectors empowered this technique with spectroscopy resolvability to distinguish

different elements. Most recently, the instrument of this technique has been further simplified, making the technique much more price-friendly and serviceable. It has been proved that even with a laboratory X-ray tube one can fluently take a realtime XRF movie, which displays the process of chemical redistribution in an aqueous reaction system. Therefore, the technique is quite suitable for realtime observation of diffusing elements in chemical garden.

4.1.2. Experiment

In this research, a fine mixture of calcium salt and ferrous salt was used as a seed of chemical garden. Its tubular growth and subsequent aging process were recorded by an XRF movie. By virtue of the movie, it has been established that the calcium distribution greatly differed from the iron distribution in the final precipitated tubular structures. Moreover, calcium and iron showed quite different diffusion behaviors in the aging process of many hours. The reason for such difference was explained.

The chemical garden experiments is performed in a Hele-Shaw cell, which is prepared by covering the upper surface of a shallow polystyrene container with a polyester thin film. The depth of the container is 0.5 mm. The thickness of the thin film is 50 microns. The operation of attaching the thin film has to be very careful to ensure the film is perfectly flat and parallel to the bottom surface of the container. In the experiment, the seed of chemical garden is placed in the container prior to attaching the thin film. After attaching, the cell is vertically placed. The chemical garden reaction is triggered by injecting the sodium silicate solution into the cell from the cell's upper edge. The dimension of the Hele-Shaw cell is 3 mm (H) × 1.5 mm (V).

In this study, the seed of chemical garden is a mixture of calcium chloride and ferrous sulfate heptahydrate. The mass ratio of these two salts is 1:1. They are mixed and grinded into fine powders in a mortar, and then the powders are pressed into a 0.5-mm-thick wafer. The chemical garden seed is a square of approximately 1.5 mm × 1.5 mm which is cut from the wafer. The color of the seed is pale yellow. The aqueous sodium silicate solution used in this research is diluted from a commercial concentrated solution (*wt.* 55% $Na_2SiO_3$). The mass ratio of the commercial solution to the distilled water is 1:2.

The growth of chemical garden and the subsequent aging process is observed by a realtime XRF movie. The technique details of XRF movie have been described in Chapter 2. The Hele-Shaw cell is fixed on the sample holder. Because one surface of the Hele-Shaw cell is made of thin film, incident X-rays can penetrate this surface to excite the inner reactants and fluorescence X-rays can escape from it. The elapsed time of chemical garden reaction as well as the XRF movie is 15 hours. After that, the Hele-Shaw cell is moved to an optical microscopy, and a photo of the precipitated tubules is captured. The observation area of XRF movie is approximately 7 mm (H) × 4 mm (V), which is mainly limited by the size of the incident X-ray beam. The spatial resolution is better than 100 micron.

The schematic illustration of the Hele-Shaw cell under XRF movie observation is shown in Figure 4-1.

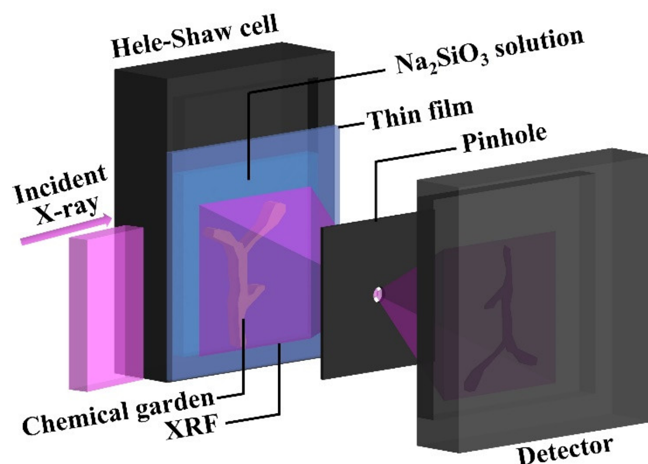


Figure 4-1. Schematic illustration of the Hele-Shaw cell and the XRF instruments. The dimension of the cell is 3 mm (H) × 1.5 mm (V) × 0.5 mm (thickness). From Ref[74].

4.1.3. Results and discussion

Figure 4-2 shows the photo of the final chemical garden structure after the reaction. The scale bar is 1 mm. The arrow indicates the upward direction of the vertically-placed Hele-Shaw cell. The red dashed rectangle indicates the observation area of XRF movie. The red triangular mark indicates the initial position of the wafer seed, which dissolves and is enveloped by a big swell during the reaction. Some plant-like tubules appear on the base of the big swell. Their growth directions are mostly upward. The final chemical garden structure shows different colors at different parts. In general, the white structures appear at the upper parts of the tubules, whereas the green structures appear at the lower parts as well as the boundary of the big swell. Clearly, the diversity of colors indicates the difference of chemical composition. It should be noticed that the initial wafer seed is a homogeneous mixture. Therefore, such a macroscopic diversity of chemical composition is actually a product of self-organization. This phenomenon is presumably due to the difference of chemical properties of iron and calcium, because it has not been reported in previous chemical garden experiments of pure calcium salt seed or pure ferrous salt seed. Nevertheless, it is difficult to deduce the chemical composition at difference parts only by looking at the appearance color. This is the reason why the XRF movie technique has been employed for this observation.

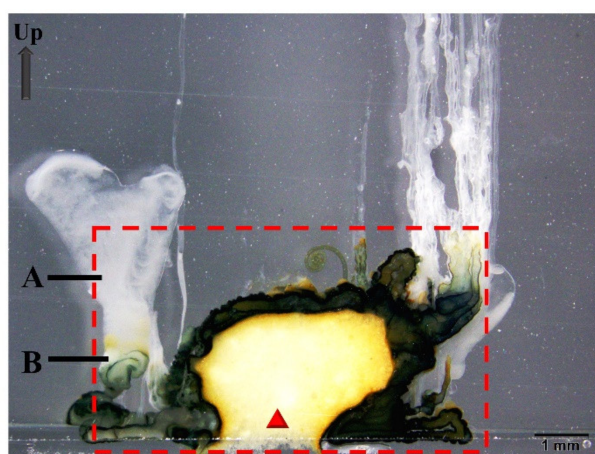


Figure 4-2. Optical microscopy photo of the final chemical garden structure after 15 hours reaction. The scale bar is 1 mm. The red dashed rectangle indicates the observation area of XRF movie, which is approximately 7 mm (H) × 4 mm (V). Region A indicates a typical tubular structure of white color and Region B indicates a typical structure of green color. From Ref[74].

A similar experiment is conducted under the observation of an optical microscopy. The rapid tubular growth is recorded in Figure 4-3. The same phenomenon is reproduced, proving that the color diversity is not induced by X-rays. As shown in the video, the tubular growth is pioneered by white structures, whereas green color subsequently follows to appear from lower parts to upper parts.

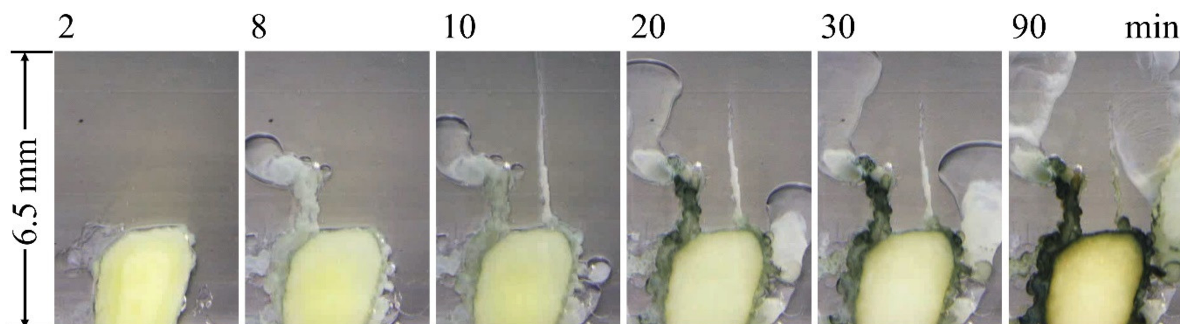


Figure 4-3. Tubular growth of in a similar chemical garden experiment, recorded by an optical microscopy

The XRF movie provides much information in different forms. Figure 4-4 shows the full-field XRF spectra, which accumulate all detected XRF signals in 15 hours. The spectroscopic property of XRF movie

enables it to distinguish different elements. As shown in Figure 4-4, the spectra peaks of calcium (Ca K$\alpha$, Ca K$\beta$) and iron (Fe K$\alpha$, Fe K$\beta$) can be clearly identified. The spectra peaks of calcium are much weaker than those of iron, because XRF photons of calcium have lower energy than iron and consequently they are more intensively absorbed in the solution, in air and in the detector window. For the same reason, other elements in the reaction system, including hydrogen, oxygen, sulfur, sodium and chlorine, are not shown in the spectra, because their even lower-energy XRF photons are totally absorbed. Nevertheless, since the seeded metal cations is generally of the most interest, the XRF observation can still provide much useful information even if doesn't see light elements.

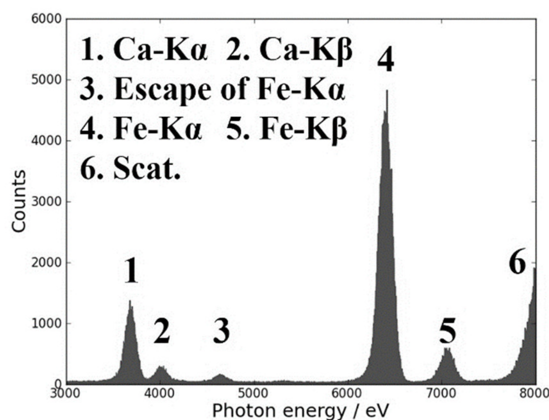


Figure 4-4. Full-field XRF spectra of the chemical garden. The XRF signals are accumulated in the whole 15 hours reaction. Spectra peaks of Ca and Fe can be identified. From Ref[74].

The XRF signals of calcium and iron are extracted to compose time-resolved XRF images of calcium and iron, respectively. Since the observation of XRF movie lasts for 15 hours, it is acceptable to set its frame rate as one frame per hour in order to study the gradual chemical diffusion during the long-term aging process. In this case, for each element, in total 15 movie frames are generated, and every movie frame represents the element's spatial distribution in this one hour. Figure 4-5 displays some key movie frames, in which the scale bar is 1 mm.

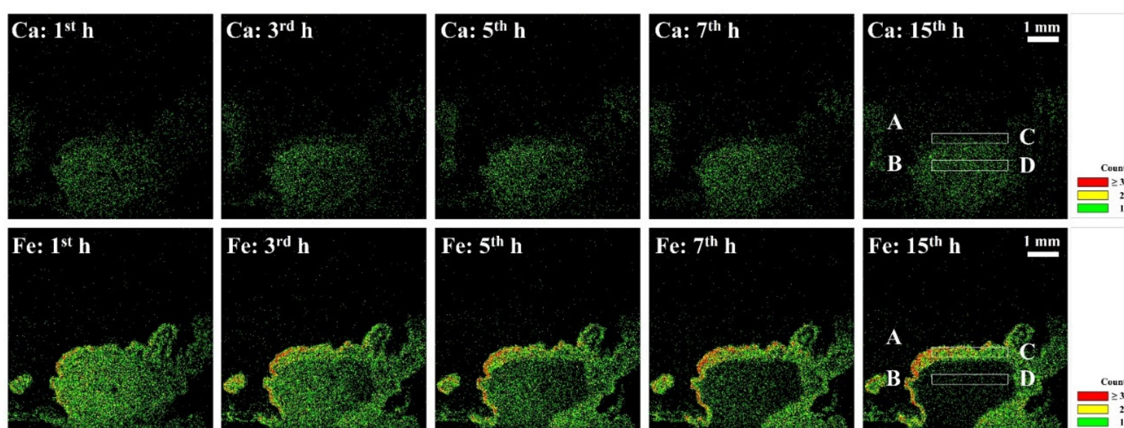


Figure 4-5. Sequential movie frames of Ca and Fe. The movie indicates the gradual diffusion of calcium and iron during the long-term aging process. The frame rate of the movie is one frame per hour. Region A and B have different element composition. Region C is at the boundary of the big swell, and Region D is inside the swell. From Ref[74].

The correlation between optical appearance and element composition is clarified by comparing Figure 4-2 with the 15th movie frames in Figure 4-5. It is quite clear that the green structures include both calcium and iron, whereas the white structures only include calcium. Thus, it is presumably inferred that iron is the actual color agent in the green structures. The most typical evidence is marked by A and B in both Figure 4-2 and Figure 4-5. At the position of A, the XRF image of calcium doesn't exactly match the outline

of white plumes in the photo. This is because the XRF observation is more sensitive to superficial structures. The gossamer white calcium membranes located in the deeper parts of the Hele-Shaw cell cannot be clearly imaged, because calcium XRF photons are intensively absorbed in the solution. It should be figured out that the one-to-one mapping of calcium to white color and iron to green color is a very fortunate case in the field of chemical garden. In many other cases, the correlation between appearance color and element composition is confusing. For example, the precipitated membrane of iron shows green color when it is ferrous-dominated, and it turns brown when it is oxidized to ferric-dominated. For another example, cobalt shows red color when its cations are dissolved in solution, but it turns blue when it is precipitated in the form of cobalt hydroxide colloid. The correlation may become more complicated when two or more metal cations are mixed or coprecipitated. For this reason, it is necessary to utilize XRF imaging to reveal the reliable spatial distribution of different elements in a chemical garden reaction.

After understanding the correlation between appearance color and element composition, the optical microscopy recorded images (Figure 4-3) of the chemical garden reaction is reviewed. As shown in the images, the growth of tubules is quite fast, whereas iron climbs up these tubules in the later stage. This is presumably because that the growth of calcium tubules is much faster than iron. In 2011, it was reported that calcium chloride has the lowest induction time and the highest linear growth rate among four metal-ion salts of calcium chloride, manganese chloride, cobalt chloride and nickel sulfate. This tendency is believed to be related to the solubility product constant of these salts in hydroxides. For calcium hydroxide, the solubility product constant is $5 \times 10^{-6}$, which is much larger than the other three metal elements. Our experiment is consistent with this conjecture, because the solubility product constant of ferrous hydroxide is $8 \times 10^{-16}$, which is significantly smaller than calcium hydroxide. This experiment proves that the difference of growth rate is remained, even when the two reactant metal salts are evenly mixed in advance. The difference of growth rate results in a macroscopic inhomogeneous distribution of calcium and iron, which could be subsequently fixed when the tubular growth stops for some reasons. As a result, it looks like that a portion of calcium is purified from the mixture of two elements.

The sequential movie frames in Figure 4-5 show the gradual diffusion of calcium and iron in the long-term aging process after the tubules have been formed. It is quite clear that iron is gradually diffused from the internal solutions to the precipitated boundary walls of the big swell. This phenomenon is not of surprise, because hydroxyl ions are continuously driven into the swell through the semipermeable membrane by its transmembrane concentration gradient. As a result, more and more ferrous ions in the internal solution are trapped and precipitated at the interior surface of the membrane. This process leads to the composition gradient of the membrane, which mainly contains metal hydroxides in its interior surface. In general, the composition gradient is characterized by EDS, and it has been widely reported in many other works[79,86,88].

On the contrary to iron, the spatial distribution of calcium remains quite stable in the aging process of many hours. This contrast could be explained by the solubility product constant as well. As the constant of calcium hydroxide is ten orders of magnitude larger than ferrous hydroxide, the calcium ions are far less sensitive to the entered hydroxyl ions than the ferrous ions. Therefore, the diffusion and precipitation behavior of calcium is obviously different from iron, and its redistribution is nearly unnoticeable. The present research is for the first time reporting such a difference in a mixture-seed chemical garden reaction, but some related clues can be found at least in one paper published in 2011.[79] In that paper, the authors stated that the wafer seed of manganese chloride and the wafer seed of cobalt chloride became empty or hollow at the end of their respective chemical garden reaction, whereas this phenomenon is not mentioned in the calcium chloride reaction. The nature of the hollow iron shell would be almost the same with manganese and cobalt, because their solubility product constants are in the same level. In the present research, the gradual formation process of the hollow iron shell is directly recorded by the XRF movie. It proves that the formation mechanism is dominated by the metal ion's chemical property rather than fluid convection, because the big swelling shell is still full filled with calcium. This also would explain the reason why calcium structures grow faster than iron structures even if these two elements share the same tubules. During the tubular growth, when ferrous ions are ejected or pumped upward, they are more likely to be trapped and exhausted by the diffusing hydroxyl ions. As a result, the tubular growth is always guided by calcium structures.

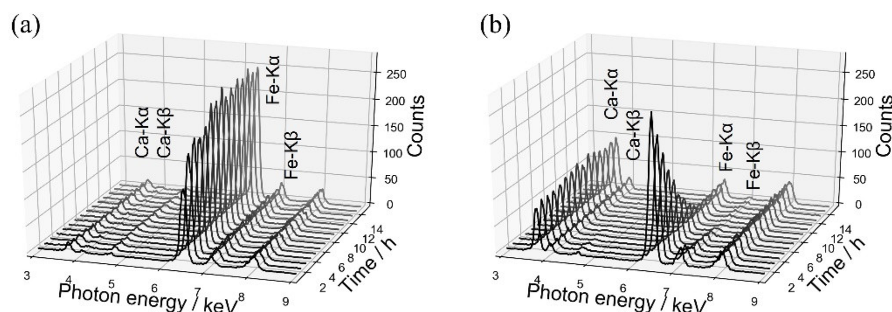


Figure 4-6. Sequential time-resolved localized XRF spectra at Region C (a) and Region D (b)

In order to study how one can synthesize new composite materials via the chemical garden route, in many cases people need to quantitatively know the composition or concentration change at different parts in the reaction. The XRF movie can provide such quantitative information. It can generate plenty of time-resolved localized XRF spectra, which reflects the element composition within a micro region in a specific time interval. For example, in Figure 4, two regions are defined. Region C is at the boundary of the big swell, and Region D is inside the swell. Many time-resolved XRF spectra of C and D have been collected. They are displayed in Figure 4-6. The localized XRF spectra taken from different hours are clearly different, indicating the respective composition change at C and D. It is possible to calculate the exact element concentration by carefully analyzing the time-resolved localized XRF spectra, but generally this requires much effort in modeling the sample matrix and fitting the spectra. This time, the intensity of XRF peaks was just used to represent the amount of the corresponding element, because such semi-quantitative approximation is broadly adopted in many other XRF imaging studies. Figure 4-7 shows the time-dependent change of calcium intensity and iron intensity at C and D, respectively. As shown in the figure, the intensity of iron increases at C, which is negatively correlated to its intensity decreasing at D. On the contrary, the calcium intensity remains quite stable in all the 15 hours, at either C or D. This semi-quantitative analysis in Figure 4-7 agrees with our impression on the sequential movie frames in Figure 4-5.

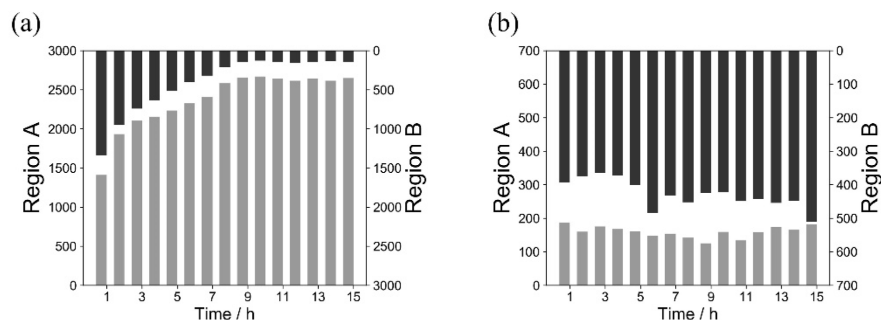


Figure 4-7. XRF intensity change of Fe (a) and Ca (b) at two different regions.

The XRF movie also records the rapid tubular growth at the early stage. To see this, the frame rate of movie is adjusted to one frame per three minutes. This three-minute-time-resolution movie is generated from the same data base of all detected XRF signals. Some key movie frames of iron are displayed in Figure 4-8, showing the growth process of the specific tubules containing iron. In this experiment, because the detected calcium XRF intensity is not so strong, it is difficult to collect sufficient statistics in every three minutes to generate a clear frame of the three-minute-time-resolution movie. However, this barrier could be easily removed by optimizing the X-ray movie instrument in the future, mainly be increasing the incident X-ray intensity. After that, people can directly compare the growth rate of calcium tubules and iron tubules by appreciating an XRF movie. This will be more reliable than looking at the appearance color of tubules in an optical microscopy video. In the XRF movie observation, if some necessary data processing parameters have been set in advance, the XRF movie frames can be sequentially generated parallel to the chemical garden reaction. Thus, the XRF movie observation is a realtime observation.

In this study, the chemical garden reaction is confined in a quasi-two-dimensional Hele-Shaw cell rather than in a three-dimensional test tube. This is convenient for X-ray observation, because generally X-rays cannot penetrate into or escape from deep parts of solutions. This operation of reducing the dimensionality is also adopted in some other works[76,78] for the ease of observation and discussion. Though most chemical garden reactions are three-dimensional, the observation of quasi-two-dimensional reactions can still construct an approximated model to help understand the universal reaction mechanism. It should be figured out that the Hele-Shaw cell in this research is vertically placed. It doesn't eliminate the buoyancy force and consequently the formed tubular structure is the same with general chemical garden structures. In some other works[102,103], the Hele-Shaw cell in horizontally placed and the vertical growth of chemical garden structures is restricted, therefore some special spiral patterns are finally formed. It should be noticed that the chemical garden reactions discussed in this research are different from those horizontal reactions.

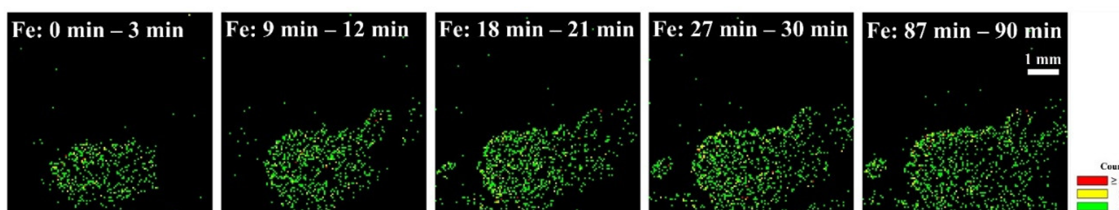


Figure 4-8. Sequential movie frames of iron at the rapid tubular growth stage. From Ref[74].

4.1.4. Conclusion

Instead of seeding only one species of metal salt in a chemical garden reaction, the present research used a mixture of two metal salts, which were calcium chloride and ferrous sulfate heptahydrate. It was found that the upward growth of calcium structures was obviously faster than iron structures, even though these two elements shared the same tubules in the same reaction. In addition, during the subsequent long hours aging process, iron diffused to the boundary of a big swell formed around the initial seed position, forming an empty iron shell at the end of reaction. On the contrary, calcium was homogeneously dispersed inside the shell with no obvious distribution change over time. The difference of growth rate and diffusion behavior could be explained by the different solubility product constants of calcium and iron in their hydroxides. As a result, a macroscopic diversity of colors and element compositions occurred in the final self-organized chemical garden structures, implying a possibility of purifying elements or synthesizing gradient composites via the chemical garden route in future.

The discovery in this research relied on the use of XRF movie technique. It can reveal the nature of element species and monitor their spatiotemporal change during the reaction. Moreover, the X-ray movie technique can provide plenty of time-resolved XRF spectra for micro-region analysis, which semi-quantitatively reflect the composition and concentration change at different parts. In short, the X-ray movie technique provides much information on chemical composition, which cannot be analyzed by an optical microscopy video. Therefore, the technique is significantly helpful to understand the stagewise formation process of chemical garden structures. Nowadays, in order to seek for material applications of chemical garden, more and more chemicals are introduced into the reaction. The use of XRF movie will be an indispensable realtime characterization technique to observe diffusing elements in such reaction.

**4.2. Rapid growth of zinc dendrites in electrodeposition**

4.2.1. Introduction to dendrite growth in electrodeposition

Dendrite growth in electrodeposition is a diffusion limited aggregation process. The final product has a dense branching morphology. This phenomenon may happen for metals like lithium, copper, zinc, and silver. It has been reported that the deposited structure may have catalytic performance. In recent years, the dendrite growth in lithium batteries has caused wide interests because the deposited lithium dendrites may reduce the battery life time and cause safety problems. Many methods have been proposed to inhibit dendrite growth. For this reason, it is of great significance to study the formation and growth mechanism of dendrite structures in electrodeposition.

Optical microscopy is utilized as the most common tool to record the entire process of dendrite growth. However, when people want to see the invisible ions dissolved in solutions and to learn the

interaction of two or more ions of different elements, XRF movie imaging is an indispensable technique. More than ten years ago, Prof. Kenji Sakurai has recorded high-time-resolution (~1 s) and high-spatial-resolution (< 20 μm) XRF movies of the growth process of copper dendrites with using a conventional CCD camera and the collimator plate. Unfortunately, at that time the camera had no X-ray energy resolution and consequently the movie could not record the diffusion of two or more elements simultaneously. In this work, we use the sCMOS camera working in single-photon-counting mode. The newly-introduced X-ray energy resolution enables the multi-element study on dendrite growth.

4.2.2. Experiment

The experiments were conducted in BL-14B, Photon Factory, KEK, Japan. The primary X-ray beam passed through a double-crystal monochromator in which the reflection plane was Si (111). The primary X-ray beam was collimated to 1 mm in width and 10 mm in height. Its energy was 13.5 keV. In the imaging experiments, samples were vertically placed and the glancing angle between the primary X-ray beam to the sample surface was around 5°.

The utilized visible-light CMOS camera (PCO.edge 5.5, PCO AG) has been introduced in Chapter 2. A micro pinhole was drilled on a 50-μm-thick tungsten foil and then the pinhole was installed in front of the X-ray window. In order to measure X-ray photon energy, the camera was operated in single-photon-counting mode and all camera images were processed by an integrated-filtering method for charge-sharing correction.

Two additional operations were necessary for applying the camera to synchrotron experiments. Firstly, the top part of the camera housing was changed from aluminum to 2-mm-thick brass so that it can shield high-energy X-ray scatterings. On the other hand, the double-crystal monochromator was adjusted to detuning to eliminate high-order harmonics reflected from Si (333), otherwise the high-energy X-rays above 40 keV will cause strong electric noises on the camera sensor.

4.2.3. Results and discussion

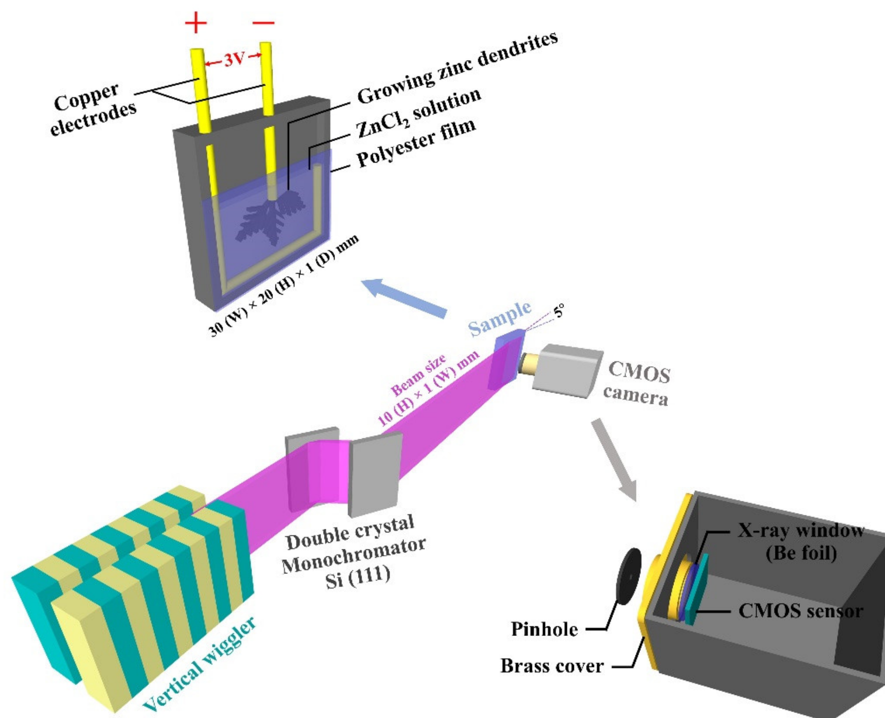


Figure 4-9. Schematic illustration of the experimental setup. From Ref[33].

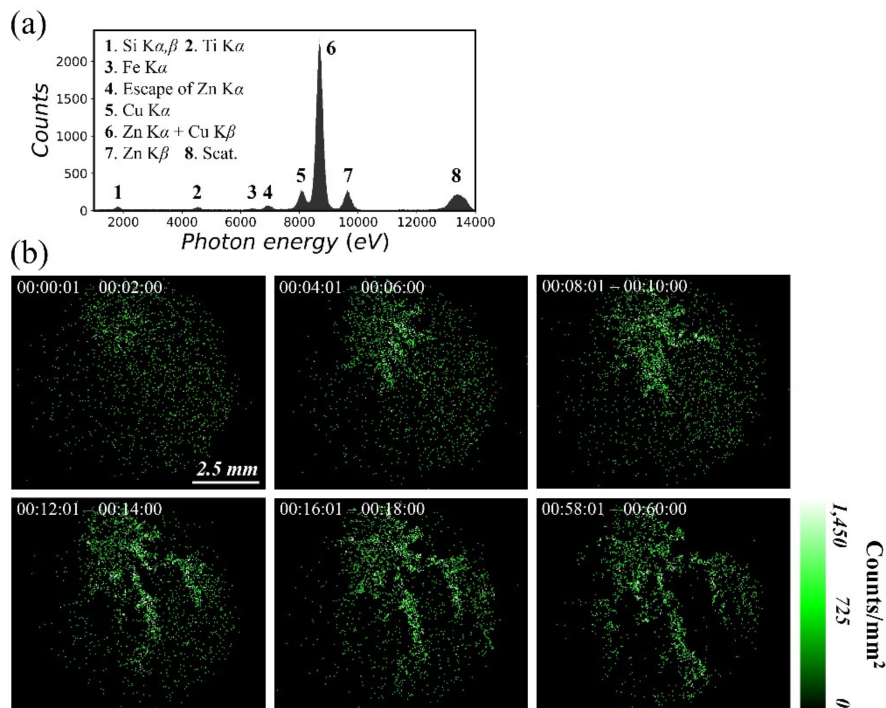


Figure 4-10. XRF movie of zinc dendrites growth during electro-deposition. (a) Full-field XRF spectra. (b) Some key frames of the movie. The time resolution is 2 minutes. From Ref[33].

As a demonstration of multi-element X-ray movie imaging, the growth process of zinc dendrites during electro-deposition was recorded. The reaction took place in a thin container whose dimensions were 30 mm (W) × 20 mm (L) × 1 mm (D). In the container, 0.1 M $ZnCl_2$ solution were filled and two copper electrodes were inserted (Figure 4-9). The distance from the upper cathode tip to the lower horizontal anode wire was 15 mm. The electric potential between them was 3 V. The front surface of the container was made of a 50-μm-thick polyester film to pass X-rays. In this experiment, the pinhole was replaced by a 50-μm-dia one to collect more XRF signals though it will reduce the spatial resolution. The distance from the pinhole was 8 mm to the reaction cell and 14 mm to the camera sensor. After triggering the reaction by connecting the circuit, the experiment lasted for 1 hour and so did the movie recording. In the full-field XRF spectra [Figure 4-10(a)], most signals in the Zn K$\alpha$ peak came from the reaction cell and therefore the spectral imaging of Zn K$\alpha$ was able to sketch the zinc distribution in the reaction. Parallel to the reaction, images of zinc were generated every two minutes and finally a continuous movie was obtained [Figure 4-10(b)]. It is clear that zinc dendrites firstly appeared on the upper cathode tip and then gradually grew downward while the zinc dispersed in the solution was gradually exhausted.

In the spectra in Figure 4-10(a), the small peak of Si K$\alpha,\beta$ came from the Si-based camera sensor. The small peaks of Ti K$\alpha$ and Fe K$\alpha$ came from trace environmental contaminants. In addition, in this study the XRF spectra have a slight spectral contamination of zinc and copper from the brass camera housing. In the future, this contamination can be easily eliminated by optimizing the housing shape or coating other high-Z “XRF-silent” elements. On the other hand, the present work shows that the spatial resolution of full-field XRF imaging can reach 15 μm solely by utilizing a micro pinhole of which the size is small enough. Nevertheless, in this case the XRF intensity collected by the pinhole becomes too weak and consequently a larger pinhole is adopted in the movie experiment as a compromise. To solve this problem, one may use an even stronger synchrotron X-ray beam to compensate the intensity loss or replace the pinhole by other X-ray imaging optics such as the collimator plate.

The silicon-based image sensor of the CMOS camera was estimated to be thinner than 10 μm by measuring and comparing its absorption efficiency for X-rays of different energies. Therefore, the visible-light CMOS camera has a lower detection efficiency for high-energy X-rays compared to many professional X-ray area detectors. However, still its low cost provides a great feasibility for many researchers to build up their own setups. Moreover, considering its unique advantage of large pixel amount and fine pixel size, it is

clear that the CMOS camera will become an irreplaceable instrument for visualizing the chemical diffusion in various reactions.

In this work, the XRF imaging technique is applied to the observation of dendrite growth during electrodeposition. It can also do realtime observation of ion absorption and desorption in batteries during charge cycles. It can be applied to many types of batteries including NiMH batteries, Ni-Cd batteries, and lead-acid batteries. However, unfortunately it cannot see lithium element directly: Generally speaking, XRF analysis is not applicable to low-Z elements ($Z<14$) because their XRF energy as well as the fluorescence yield is too low. Nevertheless, the process of lithium absorption and desorption can still be studied indirectly by inspecting the structure change of electrodes with using other realtime X-ray techniques, e.g., the morphological evolution of multilayer electrodes during lithiation.

Catalyst metallic ions also play an important role in batteries. Their chemical-state map is generally more important than their diffusion. In this case, X-ray absorption fine structure (XAFS) imaging for the electronic structure of transition metals is more useful than XRF movie imaging. However, so far, there is no full-field XAFS imaging technique available for investigating minor elements yet. In Chapter 3, a scheme of full-field XRF imaging is developed with using a size-expanded polarized synchrotron beam to improve the signal-to-background ratio in the investigation of trace or minor elements. In the next, the scheme will be smoothly extended to XAFS imaging for minor elements, and the chemical-state map of catalyst metallic ions in batteries will be an important application.

In recent years, X-ray techniques are more and more applied to battery studies. Powerful methods for clarifying reactions inside batteries include XAFS for the electronic structure of the transition method in cathode material, XRD for the crystal structure of the cathode active material and so on. On the other hand, the breakthrough may come if these X-ray techniques can be endowed with a spatial resolution to visualize the inhomogeneity in batteries and with a temporal resolution to capture the changing process. Developing such techniques for inhomogeneous systems and for chemical diffusion is right the aim of present thesis.

## Chapter 5. X-ray standing wave imaging for visualizing interface inhomogeneity

*Portions of this chapter were adapted with permission from W. Zhao and K. Sakurai, Phys. Rev. Mater. 3, 023802 (2019)*[104] *Copyright (2019) by American Physical Society.*

### 5.1. Introduction: From XSW analysis to XSW imaging

Nanolayers assemble atoms, molecules, and nano-particles into a highly ordered structure in Z direction for designed properties. They play an important role in surface coating, semiconductor devices, and some sensors. Nanolayers may have many defects like pores and impurities and the properties of nanolayers are strongly influenced by such defects. The distribution of these defects in nanolayers are generally inhomogeneous. Therefore, the analysis of nanolayers should be not only in Z direction but also in the XY plane.

On the other hand, the conditions of surface and interfaces are crucial in organizing nanolayers and they are often the switch of controlling nanolayer properties. For this reason, the inhomogeneity of defects, especially foreign impurities at surface and buried functional interfaces, should be carefully analyzed. Visualizing the inhomogeneity at buried functional interfaces is necessary to understand the structure-property correlation of nanolayers.

So far, the full-field XRF imaging technique provides 2D images which reflect the XY distribution of impurity elements in samples. However, the technique itself has no sensitivity to the buried depth or Z distribution of the elements. On the other hand, the existing X-ray standing wave (XSW) technique can measure the depth profile of chemical elements in nanolayers, yet it has no imaging capability and the measurement neglects the inhomogeneity in the XY plane. For this reason, it is necessary to combine these two techniques into a new one: XSW imaging.

The XSW field[105] created by the interference of incident X-ray waves and reflected X-ray waves creates an atomic-scale yardstick for measuring the precise position of impurities in their host materials. Theoretically speaking, this works for any material where strong X-ray interference can be induced, e.g., Bragg diffraction in a perfect single crystal, total reflection at a smooth surface, and multiple reflections in a periodic multilayer (PML). In these materials, the XSW field has a periodic intensity variation in the direction normal to the reflection planes. Also, the XSW field moves in the normal direction when the angle between the propagation direction of the incident waves and the reflection waves changes slightly. As the XRF intensity of an impurity is proportional to the XSW intensity at its location, one can study the distribution of the impurity in the normal direction by analyzing how its XRF intensity changes during an angle scan. More than 50 years ago, the technique was first presented by Batterman to determine the foreign atom sites in a single crystal[106,107]. Subsequently, the technique was further developed to locate adsorbates at a crystal surface[108,109]; to investigate the impurities in a layered synthetic structure[110,111]; to probe the electrochemical deposition, diffusion layers, and bio-membranes at a solid/air or solid/liquid interface[112–115]; and even to sketch the concentration profile of the solute at a liquid/air interface[116]. Today, the technique is widely applied to characterize various nanolayer structures and interfaces.

While the XSW technique has an atomic-scale resolution in the direction perpendicular to the reflection plane, it has no spatial resolution parallel to the reflection plane. On the other hand, in XSW analysis, the probing area is determined by the illumination area of the incident X-rays, which is frequently larger than a few square millimeters. Therefore, when the XSW technique is applied to investigating the impurities in materials, the depth distribution of the impurity should be identical for every point in the probing area. However, for some ultra-thin nanolayers and interfaces, maintaining in-plane uniformity over such a wide area is difficult. For this reason, it is necessary to combine the existing XSW technique with an in-plane imaging capability. As the area of nanolayers and interfaces is frequently a few square centimeters to square millimeters, an imaging resolution at the sub-millimeter-level to micron-level is already sufficient to match the macroscopic in-plane inhomogeneity of the entire sample.

The technique of full-field XRF imaging is efficient to provide the in-plane spatial resolution. In this study, an sCMOS camera was employed as an energy-dispersive XRF imager and a micro-pinhole was inserted between the sample and the camera; thus it is possible to upgrade conventional XSW analysis to a new technique of XSW imaging (Figure 5-1). In the scheme of conventional XSW analysis [Figure 5-1(a)], the XRF intensity profile $Y(\theta)$ with respect to the angle scan is measured for all the impurity locations

combined; thus, the resolved $\rho(z)$ represents the average depth distribution of the impurity throughout the entire probing area. In contrast, in the scheme of XSW imaging [Figure 5-1(b)], the in-plane imaging capability splits the entire probing area into many independent pieces; thus, the acquired XRF intensity profile $Y_{x,y}(\theta)$ reveals the impurity depth profile $\rho_{x,y}(z)$ specifically at $(x,y)$. In this way, the XSW imaging technique provides a systematic description of the impurity locations when the impurity depth distribution has in-plane variation in the sample. The application of XSW analysis can be extended to non-uniform nanolayers and interfaces.

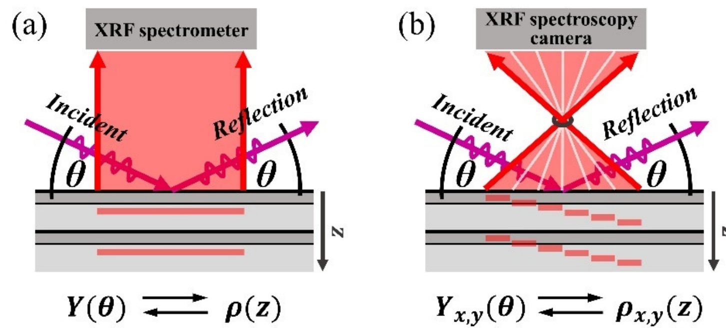


Figure 5-1. (a) Conventional XSW analysis. It measures the full-field XRF intensity profile $Y(\theta)$ and analyzes the average depth distribution $\rho(z)$ of the impurity over the entire probing area. (b) XSW imaging technique. It measures $Y_{x,y}(\theta)$ independently at every $(x,y)$ point and reveals their respective impurity depth distribution $\rho_{x,y}(z)$. From Ref[104].

**5.2. Development of the XSW imaging technique**

5.2.1. Experiment

To establish the XSW imaging technique, the sample for demonstration had total of 150 nickel/carbon bilayers coated on a 0.25 mm thick silicon substrate. The sample is prepared by DC sputtering and is commercial one from X-Ray Optics Department of Ovonic Synthetic Materials Company, Inc. Its periodic structure leads to X-ray diffraction and it serves as an X-ray mirror or an X-ray monochromator. Based on our previous XRF study, the sample was known to contain a small amount of iron as an impurity. The mass fraction of iron in nickel is estimated to be above 1%. The aim of the experiment was to investigate the distribution of the iron impurity within the periodic multilayers.

The experiment was carried out using a rotating-anode X-ray tube with a copper target (Ultrax 18, Rigaku). The tube power was 40 kV and 300 mA. The X-ray tube was equipped with a 40 mm long tungsten/silicon X-ray mirror as the monochromator to pass Cu K$\alpha$ X-rays (8047 eV). In addition, 16 µm thick nickel foils were inserted in the incident beam path to remove the contamination of Cu K$\beta$ X-rays. The size of the incident beam was 0.2 mm (H) × 10 mm (V). It could irradiate a wide area on the sample at glancing incidence. The angular divergence of the incident beam was 0.025°. The intensity arriving at the sample was approximately $8 \times 10^7$ counts per second.

The layer structure of the Ni/C PML sample was determined by measuring its X-ray reflectivity pattern (XRR) pattern (RINT-2000, Rigaku). In this measurement, the slit for collimating the incident X-ray beam was temporarily changed to 0.05 mm in width. The angular resolution of the XRR measurement was 0.03°.

The distribution of the iron impurity was investigated by the XSW imaging technique. In the experiment, a full-field XRF imaging setup was placed in front of the sample. The setup consisted of an sCMOS camera (PCO.edge 5.5) and a micro-pinhole. As already explained in Chapter 1, initially the sCMOS camera had been designed for taking ordinary photos in visible light. However, after the modification, the camera became able to record the energy of every detected X-ray photon when it worked in single-photon-counting mode. The pixel size of the camera is 6.5 µm × 6.5 µm, the number of pixels is 2560 × 2160, and the active area of the sensor is 16.6 mm × 14.0 mm. The micro-pinhole was installed between the sample and the camera sensor. It was drilled in a 25 µm thick tungsten foil and the pinhole diameter was 200 µm. It was located 4.5 mm from the sample surface and 13.5 mm from the camera sensor. Therefore, the magnification of full-field XRF imaging was 3×, and consequently the probing area on the sample was 5.5

mm × 4.7 mm. In this condition, the spatial resolution of imaging was tested to be 160 μm by measuring a standard resolution target. In the XSW imaging experiment, energy-dispersive XRF images were recorded while the glancing angle between the incident X-ray beam and the sample surface was scanned around the Bragg diffraction angle of the Ni/C PML sample.

5.2.2. Results and discussion

5.2.2.1. Analytical expressions for X-ray standing wave imaging for a periodic multilayer sample

The necessity of XSW imaging for a non-uniform sample was verified using analytical expressions. The derivation starts from a uniform PML sample. In this study, the Ni/C PML sample was prepared by a repeated coating process; therefore, the depth distribution of the iron impurity is assumed to be identical in every Ni/C bilayer. Imitating the equations for XSW Fourier analysis[117,118], two quantities are employed to describe the depth distribution of the iron impurity in each Ni/C bilayer. The first one is the coherent position, $z_A$. It describes the "average" position of the impurity in the depth direction. The second one is the coherent fraction, $f_A$. It relates to the spreading width of the impurity in the depth direction. Then, the XRF intensity of the iron impurity inside the $n^{th}$ Ni/C bilayer of the PML sample is

$$Y_n(\theta) = A_n I_n(\theta)\left\{1 + R_n(\theta) + 2\sqrt{R_n(\theta)}\, f_A \cos\left[v(\theta) - 2\pi\frac{z_A}{D}\right]\right\} \quad (5\text{-}1)$$

where $\theta$ denotes the glancing angle between the incident X-ray beam and the sample surface, $A_n$ denotes the escape ratio of the XRF from the $n^{th}$ bilayer, $I_n(\theta)$ denotes the incident X-ray intensity at the $n^{\text{th}}$ bilayer, $R_n(\theta)$ denotes the corresponding reflectivity, $v(\theta)$ denotes the phase difference between the reflection X-ray waves and the incident waves at the reference plane in the $n^{th}$ bilayer, and $D$ denotes the thickness of a Ni/C bilayer. Equation (5-1) is valid when $\theta$ is scanned around the Bragg diffraction angle $\theta_B$. In this condition a strong XSW field forms.

In this study, the PML sample has 150 Ni/C bilayers. Therefore, the total XRF intensity integrated from all 150 bilayers is

$$Y(\theta) = \sum_{n=1}^{150} Y_n(\theta) = P(\theta) + Q(\theta)\, f_A \cos\left[v(\theta) - 2\pi\frac{z_A}{D}\right], \quad (5\text{-}2)$$

where

$$P(\theta) = \sum_{n=1}^{150} A_n I_n(\theta)[1 + R_n(\theta)], \qquad Q(\theta) = \sum_{n=1}^{150} 2A_n I_n(\theta)\sqrt{R_n(\theta)}. \quad (5\text{-}3)$$

In Equation (5-2), when $\theta$ is scanned across the Bragg diffraction angle $\theta_B$, the phase factor $v(\theta)$ changes by $\pi$. Therefore, the XRF intensity profile $Y(\theta)$ around $\theta_B$ is distorted from half a period of a cosine function. The two distortion factors $P(\theta)$ and $Q(\theta)$ can be calculated by applying Parratt's recursive equations to the layer structure of the PML sample. The information about the impurity depth distribution is coded in the XRF intensity profile $Y(\theta)$.

Until now, it has been assumed that the impurity depth distribution is identical for any point on the sample. In this case, measuring the full-field XRF intensity profile $Y(\theta)$ is sufficient no matter how large the probing area is. However, for a non-uniform sample, the depth distribution of the impurity may vary with respect to the in-plane position $(x, y)$. In this case, the coherent position $z_A$ and the coherent fraction $f_A$ become dependent on $(x, y)$ and they should be denoted by $Z_{A_{x,y}}$ and $f_{A_{x,y}}$, respectively. Then, the full-field XRF intensity from the entire probing area is a summation of the intensity components at all $(x, y)$ points, which is

$$Y(\theta) = \sum_x \sum_y Y_{x,y}(\theta)$$

$$= P(\theta) + Q(\theta) \sum_x \sum_y C_{x,y}\, f_{A_{x,y}}\, cos\left[v(\theta) - 2\pi \frac{z_{A_{x,y}}}{D}\right] \quad (5\text{-}4)$$

$$= P(\theta) + Q(\theta)\, f_A'\, cos\left[v(\theta) - 2\pi \frac{z_A'}{D}\right]$$

Here, $C(x, y)$denotes the amount of the impurity at $(x, y)$. In Equation (5-4), the summation of all cosine components yields a new phase $z_A'$ and a reduced amplitude $f_A{}'$. Thus, by measuring the full-field XRF intensity profile $Y(\theta)$, one only obtains an "average" estimation, which is a compromise based on the impurity depth distribution at all $(x, y)$ points in the entire probing area. In the meantime, the variation of the XRF intensity with respect to the angle scan also becomes less noticeable. Therefore, for a non-uniform sample in which the impurity depth distribution has some in-plane variation, the scheme of conventional XSW analysis may not work, or the analysis may be strongly biased by several abnormal points of high impurity concentration. Consequently, for an unknown sample, it is necessary to measure the XRF intensity profile $Y_{x,y}(\theta)$ at every point independently. This is precisely the aim of the XSW imaging technique presented in this study.

Equation (5-2) and Equation (5-3) provide an inverse method to analyze the depth distribution of the impurity based on its XRF intensity profile. Generally, the XSW analysis for a PML sample is performed by comparing the experimental profile with many simulated profiles. To do this, one has to assume many impurity depth distribution models and simulate all corresponding intensity profiles. This comparison method is frequently low efficiency and unstraightforward. By contrast, Equation (5-2) reveals the direct relation between the XRF intensity profile $Y(\theta)$ and the corresponding impurity depth distribution which is described by the coherent position $z_A$ and the coherent fraction $f_A$. The two distortion factors $P(\theta)$ and $Q(\theta)$ can be calculated using the known layer structure of the PML sample and without any pre-assumption of the impurity depth distribution. Therefore, the phase and amplitude of the cosine function can be directly solved and subsequently $z_A$ and $f_A$. Clearly this model-free inverse method is simpler and quicker than the general comparison method. In this work this method is the first time to be proposed for PML samples where the two distortion factors $P(\theta)$ and $Q(\theta)$ are introduced.

It is noted that in Equation (5-2) two approximations are introduced. The first approximation is about the absorption of X-rays in the PML sample, including the absorption of incident X-rays and fluorescence X-rays. In the equation, when the $n^{th}$ Ni/C bilayer is under investigation, the absorption of X-rays in the above $n$-1 bilayers is considered but the absorption inside the $n^{th}$ bilayer is omitted. This omission is acceptable because one Ni/C bilayer is so thin that the inside absorption is very small. The second approximation is about the phase difference $v(\theta)$ between the reflection X-ray waves and the incident waves. In the equation, we assume $v(\theta)$ is identical for all 150 bilayers. Actually, $v(\theta)$ slightly varies for different bilayers because the period of the XSW field is more or less different from the bilayer thickness $D$ when the glancing angle $\theta$ is not exact the Bragg diffraction angle $\theta_B$. However, this influence is rather weak because the XSW field forms only in a very narrow angle region around $\theta_B$.

It is also notable that Equation (5-2) is valid only in the narrow angle region around the Bragg diffraction angle where a strong XSW field forms. In the adjacent extended angle regions, the primary X-ray field inside sample changes rapidly, resulting in high frequency oscillations in the XRF intensity profile. In these extended angle regions, the XRF intensity profile can only be simulated using recursive numerical calculations and it cannot be described by analytical expressions any more.

5.2.2.2. The layer structure of the Ni/C periodic multilayer sample

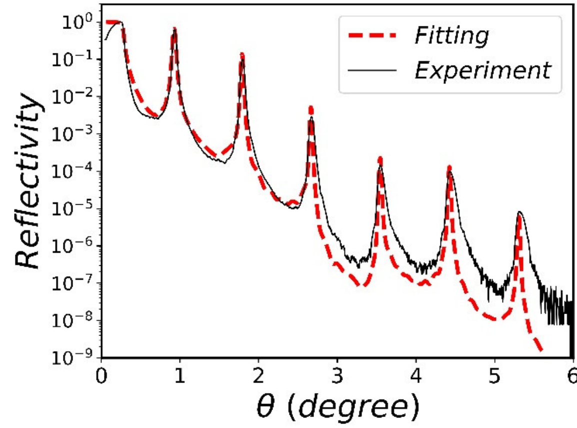


Figure 5-2. XRR pattern of the nickel/carbon periodic multilayer. From Ref[104].

The layer structure of the Ni/C PML sample was determined by measuring and fitting its XRR pattern (Figure 5-2). In the pattern, the 1st to the 6th Bragg diffraction peaks are shown. The first diffraction peak is at $\theta_B = 0.93°$. The angle position of the six diffraction peaks indicates the bilayer thickness $D$, and their intensity ratio indicates the thickness ratio of the nickel layer to the carbon layer in every bilayer, and the interface roughness. The full pattern of XRR fitting was simulated by using Parratt's recursive equations[119]. In order to simulate the interface roughness, a set of thin slices with step-changing refractive indexes were inserted at every interface. After that, the simulated XRR pattern was convoluted with a Gaussian function that represents the angular resolution of the XRR measurement. The simulated XRR pattern matched well with the experimental pattern, especially for the position and the intensity of the six Bragg diffraction peaks. It is noted that the high-order Bragg diffraction peaks in the experiment are wider than those in the simulation. This disagreement is due to the influence of diffuse scattering and the deviation of the bilayer thickness $D$ in the 150 repetitions.

The layer structure parameters obtained from fitting are listed in Table 5-1.

Table 5-1. The layer structure of the nickel/carbon periodic multilayer. From Ref[104].

| Feature | Value | Feature | Value |
|---|---|---|---|
| Bilayer thickness $D$ | 50 $Å$ | Interface roughness (RMS) | 6.5 $Å$ |
| Nickel layer thickness | 14 $Å$ | Nickel layer density | 8.0 $g / cm^3$ |
| Carbon layer thickness | 36 $Å$ | Carbon layer density | 2.1 $g / cm^3$ |

5.2.2.3. The XSW imaging experimental data

Based on the XRR measurement, the first Bragg diffraction peak of the Ni/C PML sample is at $\theta_B = 0.93°$. In the XSW imaging experiment, the glancing angle between the incident X-ray beam and the sample surface was scanned around $\theta_B$. At every angle, energy-dispersive XRF images were measured; and the measurement time was 6 hours. Figure 5-3 shows examples of the experimental data. The full-field XRF spectra were measured over the entire probing area [Figure 5-3(a)]. In the spectra, the peaks of iron and chromium correspond to the impurities inside the sample. The peak of Si K$\alpha,\beta$ corresponds to the silicon substrate. The major constituents of the sample, nickel and carbon, are not shown in the spectra because nickel K-lines were not excited and carbon K-lines were completely absorbed in air. Clearly the full-field XRF spectra are quite sensitive to the glancing angle $\theta$ when $\theta$ is scanned around $\theta_B$. This is due to the motion of the XSW field in the sample. As the main focus of this study is the iron impurity, one XRF image of Fe K$\alpha$ was generated at each angle. For instance, the Fe K$\alpha$ image taken at $\Delta\theta = +0.02°$ is shown in Figure 5-3(b). In this image, the central part is brighter than the peripheral parts because the image was measured by the pinhole-camera, and the solid angle included in the measurement was larger for the center than for the periphery. Meanwhile, there is no clear pattern in the image, indicating that the iron impurity is

dispersed randomly. In order to study the in-plane inhomogeneity, the entire image is equally divided into 100 micro-regions. The area of each micro-region is 0.55 mm × 0.47 mm, which is obviously greater than the spatial resolution of the XRF imaging. Because the micro-regions at the outermost parts of the image may be partially sheltered by radiation-shielding material around the camera sensor, these micro-regions are abandoned and only the center 64 micro-regions are labeled and analyzed, as shown in Figure 5-3(b).

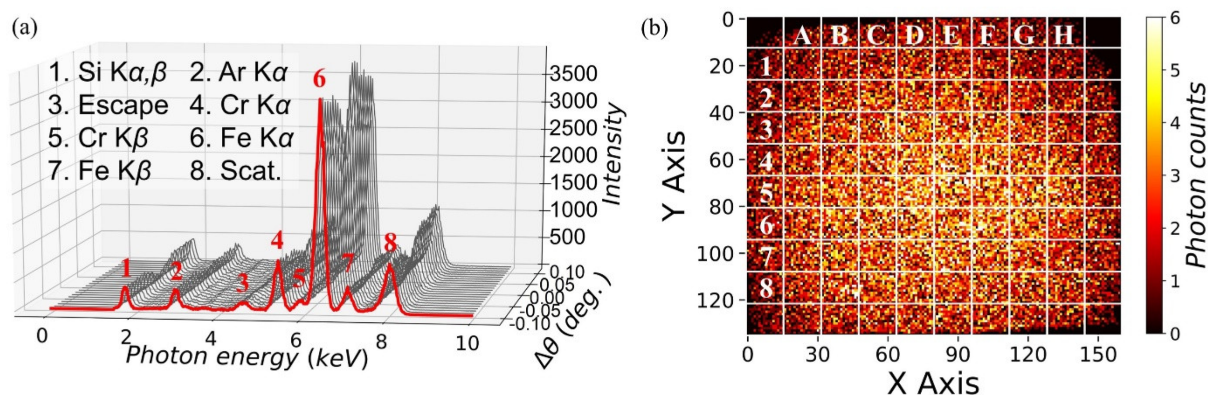


Figure 5-3. Examples of the XSW imaging experiment data. (a) Full-field XRF spectra measured over the entire probing area. (b) An XRF image of Fe K$\alpha$ taken at $\Delta\theta = +0.02°$. From Ref[104].

5.2.2.4. Verifying the in-plane uniformity of the layer structure by XSW imaging

In this study, the Ni/C PML sample is a well-established industrial product used to manufacture X-ray mirrors. Thus, it is reasonable to assume that its layer structure, which directly determines its performance as an X-ray mirror, has a perfect in-plane uniformity. It is assumed that its layer structure parameters for every micro-region are always the same as those listed in Table 5-1, which were determined by fitting the XRR pattern (Figure 5-2) of the entire sample. This assumption provides much convenience for the subsequent XSW imaging analysis. However, for many unknown samples, the in-plane uniformity of the layer structure should be verified in advance. Generally, this requires the emerging technique of XRR imaging[120], which can independently measure the XRR patterns of every micro-region in the sample. In this study, the verification was performed by the XSW imaging experiment data.

To do this, we investigated the Si K$\alpha,\beta$ intensity profile with respect to the $\theta$ scan. The Si K$\alpha,\beta$ fluorescence comes from the silicon substrate of the sample. Its intensity is roughly proportional to the X-ray intensity at the surface of the substrate, which can be calculated using Parratt's recursive equations. In the simulation, it was found that the intensity of Si K$\alpha,\beta$ decreases greatly at $\theta_B$ [Figure 5-4(a)], because the incident X-rays are strongly reflected at the Bragg diffraction angle, and the X-ray intensity attenuates rapidly when the X-rays penetrate into the deeper bilayers. This effect, also known as the extinction effect, was clearly supported by the experimental result. In the full-field Si K$\alpha,\beta$ intensity profile [Figure 5-4(a)] that was measured over the entire probing area by either the pinhole-camera system or the Si-PIN detector, the dip at $\theta_B$ is quite clear. The two full-field profiles overlap with each other, even though the sizes of their corresponding probing areas are different. Meanwhile, the experimental profiles match well with the simulated profile, when vertical contrast has been reduced by half of the simulated profile. A possible reason for this contrast reduction might be that the bilayer thickness $D$ fluctuates throughout the 150 repetitions, which has partially weakened the extinction effect.

To examine the in-plane uniformity of the layer structure, the Si K$\alpha,\beta$ intensity profiles of every micro-region have been investigated. As an example, the profiles of four micro-regions on the diagonal of the image are displayed in Figure 5-4(b). Even though the profiles suffer from a large amount of counting noise due to the weak Si K$\alpha,\beta$ intensity in detection, it is still clear that all of them have a dip at $\theta_B$, and the amplitudes of the dips are all similar to that in the full-field Si K$\alpha,\beta$ intensity profile. These results confirm our assumption that the layer structure of the sample has a perfect in-plane uniformity.

In this step, inspecting the XRF intensity profile of the silicon substrate has at least two functions. Firstly, it can screen the "broken" points where the layer structure has been destroyed, because at the "broken" points there is no strong X-ray reflection and no intensity dip can occur in the corresponding micro-region

intensity profile. Secondly, it can examine the in-plane variation of the bilayer thickness $D$, because the intensity dip occurs exactly at the Bragg diffraction angle $\theta_B$, and $\theta_B$ is extremely sensitive to the bilayer thickness $D$. Although the present approach is not as complete as the XRR imaging technique for verifying the in-plane uniformity of the layer structure, still it is quite attractive because all the necessary data can be obtained in only one angle scan using a laboratory X-ray source.

In the XSW imaging experiment, it is also possible to probe the layer structure by measuring the XRF intensity profile of nickel, because nickel is the major element that forms the frame of the PML. In this study, the XRF of nickel was not measured. The Ni K$\alpha$ intensity profile does not help in discussing the relationship between the intensity variations and $\theta_B$. As already discussed, in the Si K$\alpha,\beta$ intensity profile, the intensity dip occurs exactly at $\theta_B$. The use of Si K$\alpha,\beta$ is more useful. Furthermore, when nickel is excited by the incident X-ray beam, the intensity of Ni K$\alpha$ is so strong that it interferes with the measurement of the small Fe K$\alpha$ peak at the foot of the huge Ni K$\alpha$ peak.

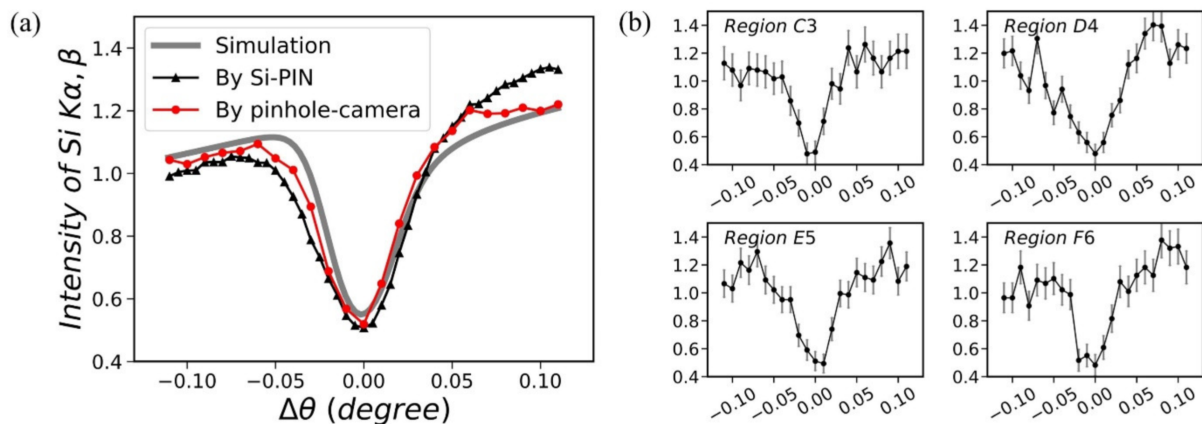


Figure 5-4. XRF intensity profile of Si K$\alpha,\beta$ from the silicon substrate. (a) Full-field profiles of the entire probing area, measured by either the Si-PIN detector or the pinhole-camera. The experimental profiles match well with the simulated profile whose vertical contrast has been reduced by half. (b) Micro-region profiles of C3, D4, E5, and F6, respectively. All of these micro-regions are along the diagonal of the image. From Ref[104].

In addition, the intensity profile of the X-ray Compton scattering[121–123] is also a potential tool for probing the layer structure of the sample. Many years ago, it has been well discussed that the intensity profile of X-ray Compton scattering has a large dip around the Bragg diffraction angle. This intensity anomaly is due to the extinction effect of the XSW field as well as its motion in the sample. Because the XSW field is directly influenced by the layer structure of the sample, the intensity anomaly of X-ray Compton scattering may become a probe to investigate the layer structure of the sample as well. In this study, we were able to record the intensity profiles of X-ray Compton scattering by the pinhole-camera in the XSW imaging experiment. Thus, the layer structure investigation can step into micro-region analysis, which is potentially an efficient tool for screening "broken" parts in the PML sample. Nevertheless, in the experiment, the pinhole-camera also receives X-ray scatterings from air and the silicon crystalline substrate. Consequently, the interpretation of the X-ray Compton scattering intensity profile becomes less straightforward and it should be performed very carefully. The full-field intensity profile and some micro-region profiles of X-ray Compton scattering are shown in Figure 5-5.

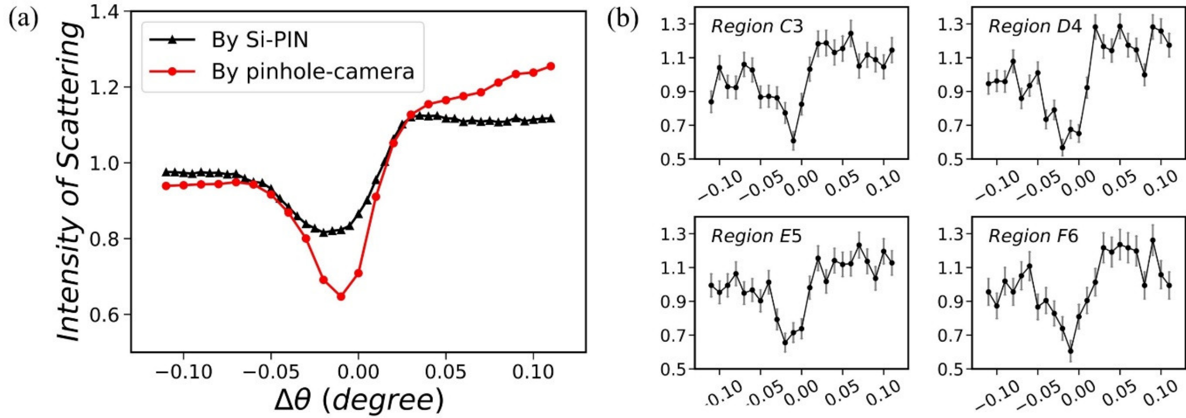


Figure 5-5. Intensity profiles of X-ray Compton scattering. (a) Full-field profiles of the entire probing area, measured by the Si-PIN detector and the pinhole-camera, respectively. (b) Micro-region profiles of C3, D4, E5, and F6, respectively. The micro regions are on the diagonal of the image. From Ref[104].

5.2.2.5. XRF intensity profiles of the iron impurity

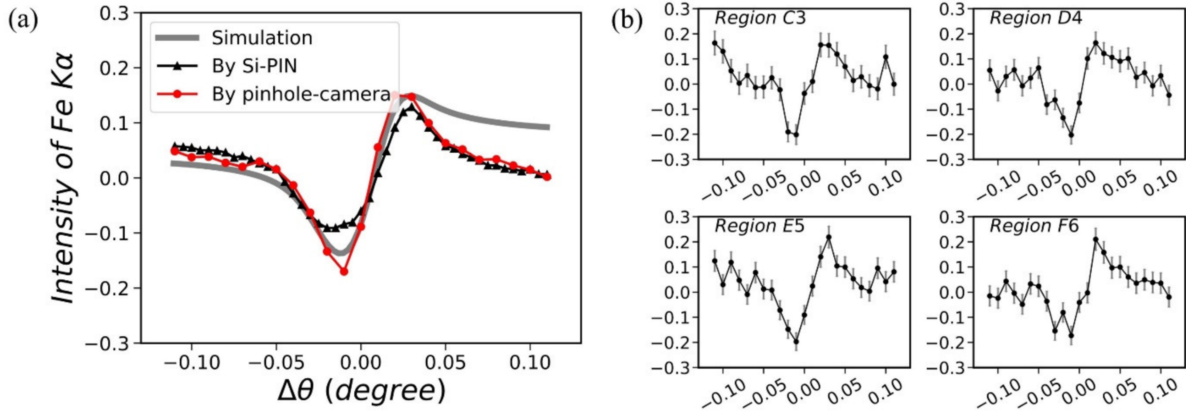


Figure 5-6. XRF intensity profiles of Fe K$\alpha$ from the iron impurity. (a) Full-field profiles of the entire probing area, measured by either the Si-PIN detector or the pinhole-camera. The experimental profiles match well with the simulated profile when the depth of the iron impurity is assumed to be at the center of each nickel layer ($Z = 7$ Å) and the vertical contrast has been reduced to 20% of the simulated profile by some experimental background. (b) Micro-region profiles of C3, D4, E5, and F6, respectively. All of these micro-regions are along the diagonal of the image. From Ref[104].

To study the distribution of the iron impurity, the intensity profiles of Fe K$\alpha$ are plotted for the entire probing area and every micro-region. The full-field profiles of the entire probing area are shown in Figure 5-6(a). They were measured by the pinhole-camera and the Si-PIN detector, respectively. The profiles of all 64 micro-regions are displayed in Figure 5-7. As an example, in Figure 5-6(b) the profiles of four micro-regions on the diagonal of the image are shown. It is noted that the two full-field intensity profiles are nearly overlapped with each other although the size of their corresponding probing area is different. This indicates that the average impurity depth distribution in the two probing areas are quite similar, and the two experimental schemes have an equivalent performance in estimating the average impurity depth distribution in a wide probing area. Moreover, the scheme of XSW imaging provides addition information independently in every micro-region.

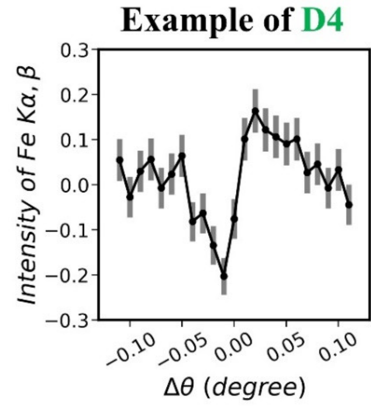


Figure 5-7. The Fe K$\alpha$ intensity profiles of all 64 micro regions. All profiles are displayed using the same ticks on the axes. The ticks are shown at the upper right corner. From Ref[104].

5.2.2.6. Analyzing the large amounts of XSW imaging data by feature map

To decode the experimental Fe K$\alpha$ intensity profiles and reveal the distribution of the iron impurity, the experimental results have been compared with simulations. In this study, we simulated the Fe K$\alpha$ intensity profile by assuming a model of the impurity depth distribution. In the model [Figure 5-8(a)], the iron impurity is dispersed in a thin slab at a depth of $Z$ Å in every Ni/C bilayer. Here, the reference plane is the top of every nickel layer and the downward direction is positive. The model of the impurity depth distribution correlates with Equation (5-2). In the model, the coherent position $z_A$, which describes the "average" position of the impurity in the depth direction, equals $Z$. The coherent fraction $f_A$, which relates to the spreading width of the impurity in the depth direction, equals one. Therefore, the present model is a good demonstration to show how the Fe K$\alpha$ intensity profile is influenced by the "average" position of the iron impurity in the depth direction, even though the model does not enumerate all the possibilities of the impurity depth distribution.

While Equation (5-2) provides the analytical expression to calculate the XRF intensity profile $Y(\theta)$ around the Bragg diffraction angle, in this simulation Parratt's recursive equations were used to calculate the depth distribution of the electric field strength $E(z)$, and then $Y(\theta)$ was simulated by

$$Y(\theta) = \int |E(\theta, z)|^2 \, \rho(z) \, dz, \tag{5-5}$$

where $\rho(z)$ denotes the impurity depth distribution. This recursive numerical method is widely adopted in much XSW research because it can calculate the XRF intensity profile in any angle region. In Equation (5-5), the absorption of Fe K$\alpha$ in the sample is omitted because the Ni/C layers are so thin that the absorption is rather weak. All the simulated Fe K$\alpha$ intensity profiles corresponding to $Z$ from 0 Å to 49 Å are shown in Figure 5-8(b).

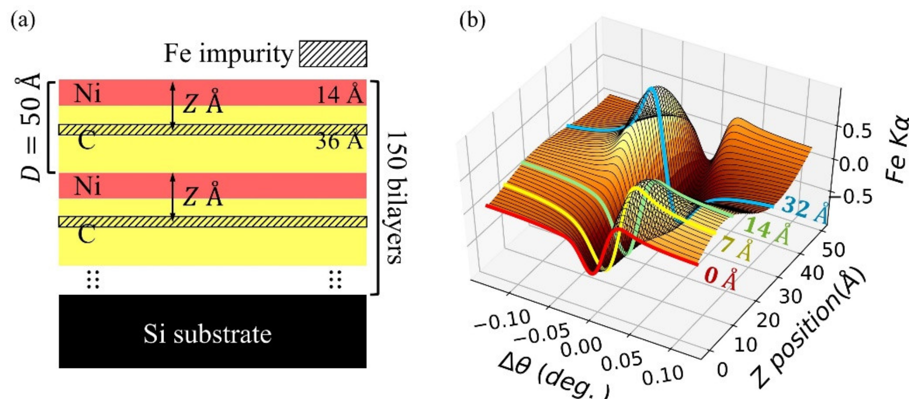


Figure 5-8. Simulation of the iron impurity depth distribution and the corresponding Fe K$\alpha$ intensity profile. (a) Model of the iron impurity depth distribution. (b) Simulated profiles. The shape of the profiles changes greatly as the depth $Z$ of the iron impurity moves from 0 Å to 49 Å. From Ref[104].

In Figure 5-8, the vertical contrast of the simulated profiles is larger than that of the experimental results. There are two reasons for this: Firstly, in the simulation model, it is assumed that the iron impurity is dispersed in a thin slab and the corresponding coherent fraction $f_A$ equals one. However, the actual iron impurity may have a spreading width in the depth direction, and in this case $f_A$ becomes smaller than one. This will reduce the amplitude of the cosine function and subsequently the vertical contrast of the XRF intensity profile. Secondly, in the actual Ni/C PML sample, the bilayer thickness $D$ may have some variation throughout the 150 repetitions. This will reduce the intensity contrast between the XSW nodal planes and antinodal planes; consequently, the vertical contrast of the XRF intensity profile will be also reduced.

In the estimation for the entire probing area, it has been found that the two full-field XRF intensity profiles have the best match with the simulated profile when the depth of the iron impurity is assumed to be at the center of every nickel layer ($Z = 7$ Å), and the vertical contrast is assumed as 20% of the simulated profile [Figure 5-7(a)]. However, in the XSW imaging analysis, an unmanageably large number of micro-region profiles were obtained. It became too cumbersome and labor-intensive to find the best match for every micro-region profile. For this reason, a new method of feature mapping has been proposed for comparing

XRF intensity profiles. In this method, each intensity profile is converted to a feature vector $(S_1, S_2, S_3)$ that describes the shape of the profile but neglects its vertical contrast. Thus, the comparison of many profiles can be simultaneously visualized by plotting their corresponding feature vectors in a feature map.

In XSW analysis, researchers mainly care about the angle region around the Bragg diffraction angle where a strong XSW field forms. In this study, the width of the Bragg region is defined as the width of the Bragg diffraction peak in the XRR pattern, which is $\pm 0.045°$ with respect to $\theta_B$. On the other hand, based on Equation (5-2), the XRF intensity profile around the Bragg diffraction angle is a distortion of half a period of a cosine function. Thus, the most important feature of one XRF intensity profile is its two extreme points in the Bragg region: the crest and the trough. For this reason, the feature vector should be strongly influenced by the two extreme points. The detailed procedure for generating the feature vector is as follows: Firstly, an intensity profile is normalized by its average intensity in the Bragg region; and, subsequently, the average intensity is taken as the baseline. Secondly, the Bragg region is divided into three parts by the two extreme points. Thirdly, for the three parts, the three variables in the feature vector $(S_1, S_2, S_3)$ describe the size of the area enclosed by the profile and the baseline, respectively. The area above the baseline is taken as positive and the area below the baseline is negative. In the final step, the three variables are normalized by the size of the absolute area of the entire Bragg region. The expressions are given by

$$S_1 = \frac{\int_{\theta_B - 0.045°}^{\theta_1} Y(\theta)\, d\theta}{S}, \qquad S_2 = \frac{\int_{\theta_1}^{\theta_2} Y(\theta)\, d\theta}{S}, \qquad S_3 = \frac{\int_{\theta_2}^{\theta_B + 0.045°} Y(\theta)\, d\theta}{S}, \tag{5-6}$$

where $\theta_1$ and $\theta_2$ denote the first and the second extreme points, respectively. The dominator $S$ denotes the absolute area size of the entire Bragg region, given by:

$$S = \int_{\theta_B - 0.045°}^{\theta_B + 0.045°} |Y(\theta_2) - Y(\theta_1)|\, d\theta \tag{5-7}$$

Two examples of calculating the feature vector are given in Figure 5-9.

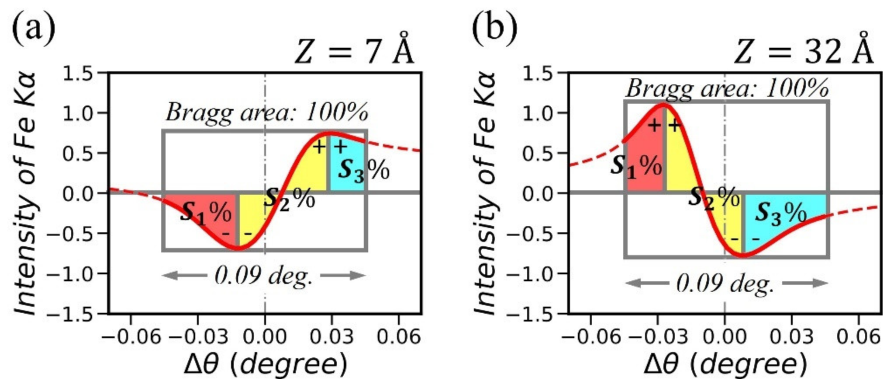


Figure 5-9. Illustration of how to convert an XRF intensity profile into a feature vector. (a) The simulated profile corresponds to the model in which the depth of the iron impurity is at the center of every nickel layer ($Z = 7$ Å). In this case, $S_1 < 0$ and $S_3 > 0$. (b) The simulated profile corresponds to the model in which the depth of the impurity is at the center of every carbon layer ($Z = 32$ Å). In this case, $S_1 > 0$ and $S_3 < 0$. From Ref[104].

Since the sum of the three variables is zero, the terminating position of a feature vector $(S_1, S_2, S_3)$ can be plotted in a ternary feature map. Figure 5-10(a) shows a feature map that has the feature points corresponding to all the simulated intensity profiles. It is noted that the feature point moves in the map while the depth distribution of the iron impurity moves from $Z = 0$ Å to $Z = 49$ Å. In detail, when the iron impurity is in the nickel layers, the corresponding feature points are gathered in the left side of the map; when the impurity is in the carbon layers, the corresponding feature points are in the right side; and when the iron impurity is at the graded interfaces between the nickel layers and carbon layers, the corresponding feature points are mostly dispersed in the center of the map. Based on this feature map, it is found that the

XSW analysis has a quite nice depth resolution and it is very sensitive to the interfaces in the nanolayer structure.

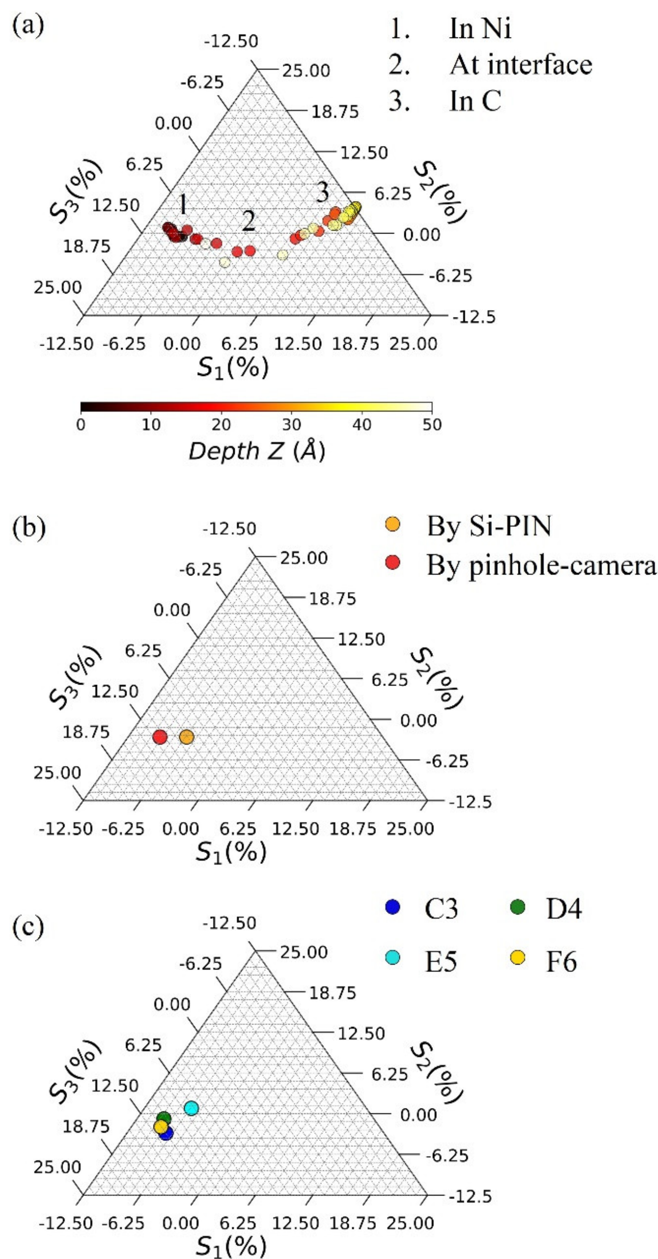


Figure 5-10. Feature map for Fe K$\alpha$ intensity profiles. (a) The feature points corresponding to all the simulated profiles. In the simulation model, the center of the iron impurity in the depth direction moves from $Z = 0$ Å to $Z = 49$ Å. (b) The two feature points corresponding to the full-field intensity profiles of the entire probing area, measured by the pinhole-camera and the Si-PIN detector, respectively. (c) The four feature points corresponding to the micro-region profiles of C3, D4, E5, and F6, respectively. From Ref[104].

A feature map that presents the result of the full-field XSW analysis is shown in Figure 5-10(b). The two feature points represent the measurement result of the pinhole-camera and the Si-PIN detector, respectively. They are quite close to each other. This agrees with the fact that the two corresponding profiles are nearly overlapped in Figure 5-6(a), indicating again the two experimental schemes have equivalent performance in estimating the average impurity depth distribution in a wide probing area. Meanwhile, the two experimental feature points are in the same region corresponding to the simulation model in which the

iron impurity is in the nickel layers. This agrees with the fact that the experimental profiles nearly overlap with the simulated profile of $Z = 7$ Å.

A feature map that shows the result of all 64 micro-region profiles is displayed in Figure 5-11. Here, as an example, the feature points corresponding to four micro-regions are shown in Figure 5-10(c). It must be noted that, although the micro-region feature points have some dispersion, they are clearly clustered in one small area of the map that corresponds to the nickel layer. In other words, none of the micro-region feature points are grouped in the region corresponding to the carbon layer or the graded interface. Consequently, it is concluded that the iron impurity in the Ni/C PML sample is always correlated with the nickel layers, and the center of the iron depth distribution never enters the carbon layers for any micro-region in the entire probing area. For this reason, it can be inferred that the iron impurity originated as a contaminant in the source material that was used to deposit the nickel layers.

In this study, using the feature map is a very efficient way to process the large number of micro-region profiles and show their relationships. Furthermore, the influence of the counting noise can be directly visualized by using the feature map. On the feature map, the position of one feature point may vibrate because of the counting noise in its corresponding XRF intensity profile. The vibration radius is proportional to the level of counting noise. In this experiment, the experimental micro-region profiles suffer from a high level of counting noise due to the weak X-ray intensity. For this reason, it is not always straightforward to use least-square fitting to find the best match between each experimental profile and the corresponding simulated profile. However, after plotting all the micro-region feature points on the feature map, the distribution of the impurity in the sample becomes apparent because it is possible to appreciate the dispersion and grouping of all the feature points simultaneously.

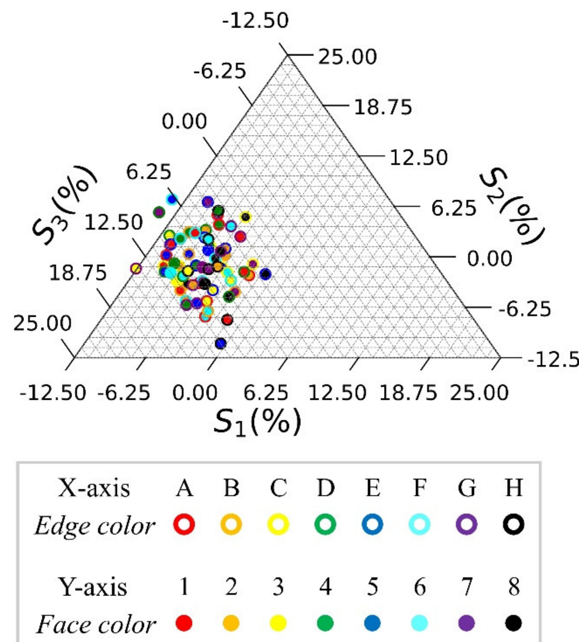


Figure 5-11. The feature points which correspond to all 64 micro-region Fe K$\alpha$ intensity profiles. The edge color of each feature point indicates the corresponding micro region's position in the X-axis and its face color indicates the position in the Y-axis. From Ref[104].

5.2.2.7. Discussion

Finding out why iron is included as the impurity is the first motivation of present work. Investigating the distribution of iron impurity in the sample can provide evidences for our inference. The more detailed we understand the distribution, the more accurate our inference will be. For example, (i) if iron impurity is found only at sample surface, it may be surface contamination due to electrostatic adsorption of iron-rich dusts or airborne particles, and the sample is likely to be contaminated during storage rather than preparation; (ii) if iron impurity is found across the sample without any feature of depth distribution, probably the vacuum chamber of DC sputtering is contaminated or iron-based components are exposed to plasma during the entire

coating process; (iii) if iron impurity is found only at interfaces, probably the exposure of iron-based components to plasma happens in the process of switching two sputtering targets of nickel and carbon. In the present work, we found the iron impurity was always associated with nickel layers. This was not only an average estimation of a wide area. Instead, we held this conclusion for every point. Therefore, we have reasons to infer the iron impurity is included in the original sputtering target of nickels.

In this study, an in-plane imaging capability was added to the conventional XSW technique. The newly-developed XSW imaging technique has a level of performance equivalent to the conventional XSW technique in the full-field analysis of a wide probing area. In addition, the XSW imaging technique provides independent information on every micro-region. Although the XSW imaging technique was mostly developed for studying non-uniform samples, in this study it is also indispensable for verifying the uniformity of the Ni/C PML sample. Using the conventional XSW technique, one can only obtain a simple estimation of the average iron impurity located in the Ni layers, but the sample can still be non-uniform and the depth distribution of the impurity may have many variations in different micro-regions. Only by using the XSW imaging technique, can the depth distribution of the impurity in all micro-regions be resolved, and the in-plane uniformity of the sample be affirmed.

In this study, the in-plane spatial resolution is around 160 μm, which is mainly limited by the diameter of the pinhole. A smaller pinhole can optimize the imaging resolution, but it decreases the detected XRF intensity. At the present stage, this spatial resolution is a compromise necessitated by the X-ray intensity during the measurement. Based on our previous study, when the incident X-ray intensity is strong enough, the spatial resolution could be optimized to ~15 μm by reducing the pinhole diameter or by replacing the pinhole aperture with a thin collimator plate. Clearly this in-plane spatial resolution is much worse than the atomic-scale depth resolution of the XSW analysis. However, many actual nanolayer structures may have a quite large area size of several square centimeters to square millimeters despite their nanoscale thickness. Consequently, the nanolayers may have macroscopic defects, patterns, and in-plane inhomogeneity that could have been introduced during the preparation process. In this case, an in-plane spatial resolution at the sub-millimeter-level to micron-level is very useful.

There is also another technique called XSW imaging[124,125]. The technique applies to a single crystal. It performs the XSW measurements twice by successively choosing two different sets of crystal planes as the reflection plane. This powerful technique is able to sketch a 3D map of the foreign atoms at a crystal surface, and its spatial resolution in all directions is atomic-scale. However, the technique also requires uniformity of the sample throughout the entire probing area so that the technique is obviously quite different from the one employed in this work.

In the experiment, the major problem is the X-ray intensity. The iron impurity in the Ni/C PML sample is only present in very small amounts; hence, its XRF intensity is not strong. The energy-dispersive XRF imager was constructed by modifying a visible-light sCMOS camera; consequently, its detection efficiency for X-rays is not high. The utilization of the micro-pinhole also sacrifices a considerable amount of the XRF intensity. For all these reasons, the detected XRF intensity was not high enough, even though the XRF imaging experiment lasted for several days. As a result, the counting noise in the micro-region XRF intensity profiles is a serious limitation. Nevertheless, this problem could be easily solved by increasing the intensity of the incident X-ray beam. In this study, the experiment was carried out with using a laboratory X-ray tube on account of its stability during the long-term measurements. However, moving the experiment to a brilliant synchrotron radiation source seems to be attractive, not only because of the high intensity, but also for the perfect beam collimation.

For more than 50 years, the XSW technique has been a powerful tool for characterizing a wide variety of nanolayers, surfaces, and interfaces[126]. In recent years, the technique has also shown its potential for investigating many new materials such as multilayer electrodes[127–130] and so on. In principle, the newly-proposed XSW imaging technique can be easily adopted to all the material systems where the conventional XSW technique works. Since the XSW imaging technique can reveal the depth distribution of the elements in every micro-region, it offers a systematic description of the impurity distribution. Thus, the relation between the impurity distribution and the performance of the sample may become clearer. In the meantime, since the XSW imaging technique does not require a uniform sample and allows the sample to have some macroscopic patterns and defects, the scope of application of XSW analysis will certainly be widened. For instance, the XSW imaging technique would make it possible to locate the contaminants, defects, and layer

distortions in Langmuir-Blodgett (LB) films[131]. Also, it would be possible to visualize the cracks or the element segregation at the buried interface when a multilayer material is fatigued.

Many techniques can do depth profiling of elements in nano thin films, including Auger electron spectroscopy (AES), X-ray photon electron spectroscopy (XPS), electron energy-loss spectroscopy (EELS), and secondary ion mass spectrometry (SIMS). These techniques are surface sensitive. They do depth profiling using ion sputtering for sample erosion. The first point to compare other techniques and our present XSW imaging technique is the precision of depth analysis and the sensitivity to buried interfaces. In other techniques, it is always essential to calibrate the ion-sputtering time to depth. However, the calibration cannot be performed or is less reliable in case certified reference samples cannot be provided. In contrast, XSW analysis does not require any reference sample. The depth information can be calculated using physical equations without relying on many instrument parameters. Moreover, in this work, the primary concern is to distinguish nickel layers, carbon layers, and interface regions. XSW analysis has shown its high sensitivity to buried interfaces in the present sample, making the analysis much more robust. The second point is being destructive or not. Using other techniques, specimens will be destroyed after ion sputtering and sample erosion, then the characterization of one specific specimen appears to be meaningless. In contrast, XSW imaging is a non-destructive technique. The specimen's properties and functions will not be altered after characterization. Also, the specimen can be tested many times to confirm the reproducibility of data. The third point is about the imaging capability. XSW imaging technique can efficiently probe a large area of about 5 mm × 5 mm with a lateral resolution, while other techniques need to destroy the same area and to scan the micro probing beam if a micro probing beam is available. In addition, XSW analysis relies on the periodicity of layer structure. Once the layer periodicity is not well preserved, abnormal features will appear in XSW experimental data. In other words, XSW imaging can also probe the perfection of periodicity across the sample, in more than one hundred bilayers, whereas other techniques are more suitable to analyze several top layers.

5.2.3. Conclusion

A new technique of XSW imaging has been proposed. It combines conventional XSW analysis with an in-plane imaging capability. The XSW imaging technique aims to visualize the in-plane variation of the impurity depth distribution in nanolayer structures. The technique has been successfully applied to study the distribution of the iron impurity in a nickel/carbon periodic multilayer sample. Moreover, a method of feature mapping has been proposed to process the large amounts of XSW imaging data efficiently. The technique is very promising for the analysis of many planar material systems as well as the visualization of the element patterns at buried interfaces.

### 5.3. Potential application to Langmuir-Blodgett films

The present XSW imaging technique could be applied to the investigation of Langmuir-Blodgett films. LB films are prepared by transferring single-molecular layers from water surface to a solid substrate. They assemble molecules and nanoparticles as bricks and build a nanoscale architecture for designed performance. The constructed nanolayers may have quantum effect and show special optical, electrical, and magnetic properties. They can make surface coatings and function surface of sensors. In recent years, it was found that the method of preparing LB films can also be utilized to prepare wafer-scale 2D materials. However, as the material properties can be significantly altered by occasional contaminants, defects, and distortions at interfaces, it is necessary to inspect such defects by the XSW imaging technique.

The model sample could be Cobalt stearate ($CoSt_2$) LB films[132]. In this work, we have prepared such samples by ourselves. One important chemical was stearic acid. It has a long tail of carbon chain and its head can connect to a cobalt ion. Generally, one cobalt ion connects with two stearic acid molecular and forms a cobalt stearate monomer. To prepare the sample [Figure 5-12 (a) – (d)], a small amount of 1 mM stearic acid (SA) / chloroform solution was dropped on the surface of 1 mM $CoCl_2$ solution. After evaporation of the chloroform and gradual surface compression, a high quality $CoSt_2$ monolayer formed on water surface. The corresponding surface pressure was 25 mN/m. Then, the monolayer was transferred to a clean hydrophilic surface of silicon wafer by repeatedly immersing and withdrawing the silicon wafer vertically in and out of the water substrate. In the final, Y-type $CoSt_2$ LB films were deposited on the silicon substrate [Figure 5-12(e)]. The long spacing of the periodic layer structure was 50 Å. As the vertical dipping repeated for 13 times, the layer repetition was 12.5. The X-ray reflectivity (small-angle X-ray diffraction)

measurement [Figure 5-12(f)] confirmed the highly ordered layer structure of the sample. Six Bragg diffraction peaks were observed in the measured pattern.

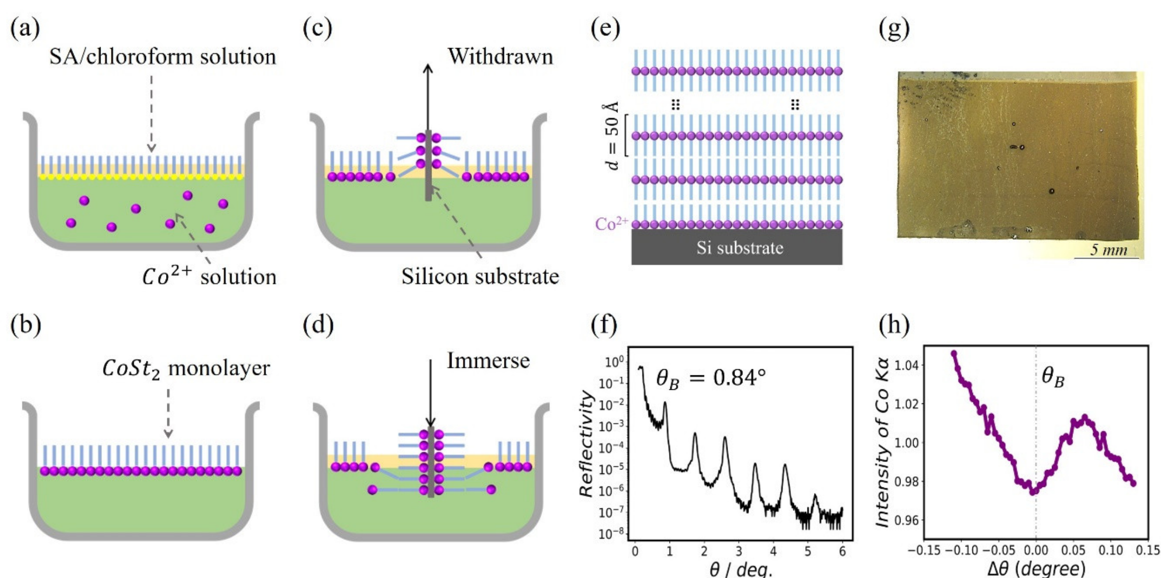


Figure 5-12. (a-d) Preparation of the cobalt stearate LB films. (e) Layer structure of the Y-type $CoSt_2$ LB films deposited on silicon substrate. (f) X-ray reflectivity (small-angle X-ray diffraction) pattern of the sample. Six Bragg diffraction peaks indicate a highly-ordered layer structure. The first Bragg diffraction angle $\theta_B$ is 0.84º. (g) Sample photo of the wafer-scale LB films. (h) Cobalt fluorescence intensity profile measured in an XSW experiment. The $\theta$ angle was scanned around $\theta_B$.

While the LB films had a highly-ordered nanoscale structure in Z direction, it might have macroscopic defect regions in the wafer-scale XY plane. For example, in one sample [Figure 5-12(g)], fine vertical patterns were observed. Such defects frequently occurred due to water drainage in the dipping process. As the visible-light microscopy photo could not reveal the layer structure at the defect regions, X-ray interface imaging techniques were recommended. For this sample, the insertion of cobalt atoms could work as an indicator of the layer structure and an asymmetric modulation of Co K$\alpha$ fluorescence intensity was observed in an XSW experiment [Figure 5-12(h)]. Therefore, XSW imaging analysis would be feasible and useful. However, frequently the layer spacing $d$ in LB films is not uniform and slightly vary from place to place. For this reason, the XSW imaging technique should be connected with XRR imaging in the characterization of LB films. The layer spacing $d$ in LB films may not be uniform in a sample of which the area size is several square centimeters. Therefore, in conventional XRR analysis of LB films, the obtained $d$ is only an average of that in the entire illumination area, and the inhomogeneity of $d$ at different points cannot be revealed effectively. In this case, the non-uniform LB films should be characterized by the newly-developed XRR imaging technique, then one would know a map of layer structure and spacing d at all points.

The interpretation of XSW imaging data relies on simulating XSW fields in the sample, which is directly determined by the local layer structure and spacing $d$. Therefore, when the sample seems to be inhomogeneous, the map of layer structure and spacing $d$ should be investigated by XRR imaging prior to the XSW imaging experiment. For the Ni/C periodic multilayer sample, this step is omitted because the sample has a high diffraction intensity as an X-ray mirror and the sample's layer structure is assumed to be uniform. For LB films, this step cannot be omitted. XRR imaging need to be performed first.

On the other hand, in cobalt stearate LB films, cobalt is not only the impurity element but also forms the main framework of the layer structure. Therefore, XSW imaging of cobalt may also be used to probe the map of layer structure. Connecting the results of XRR imaging and cobalt XSW imaging may provide much information to investigate the inhomogeneity in such LB films. This has never been realized before.

## 6. Underground survey of high-Z elements by high-energy X-ray fluorescence analysis

Ground and underground survey is important in geological, environmental, civil engineering and many other applications. So far, technologies such as ground penetration radar and ultra-sonic wave have been effectively utilized. These technologies have a great scope of exploration, up to hundreds of meters, therefore, they are mostly used in sketching large-scale underground structures such as mineral deposits, caves, tunnels and so on. However, as the trade-off, they may not be efficient enough in searching for a specific small target. For this reason, new techniques should be developed as a supplement to the present underground survey technologies.

The present chapter proposes a promising candidate technique: high-energy XRF analysis. It can penetrate thick soils and identify underground heavy metals. The terminology "heavy metal" in this chapter refers to the high-Z elements of which the atomic numbers are greater than 46. They are named as "heavy" here because their atomic weights are large. Many elements included in this class play an important role, such as toxic heavy metals, rare-earth elements and precious metals. Therefore, searching for ground and underground heavy metals is a common scenario in the modern society, while reasons for searching are various. For instance, toxic heavy metals such as cadmium, mercury and lead are detrimental to human health, therefore their contaminants must be detected and removed. Rare-earth elements can be extracted from isolated ore crystals or recycled from electronic components, therefore they should be picked out from mines or electronic wastes. Precious metals are frequently the goal in archaeological surveys, therefore locating them quickly in a wide area is necessary. In all these scenarios, techniques which can identify elements and do underground survey are useful.

As discussed in previous chapters, XRF is a powerful tool for identifying unseen elements, because X-ray can penetrate opaque samples and the emitted fluorescence X-rays' photon energy tells the element. In general, the analysis depth with a routine laboratory XRF setup is several microns to hundreds of microns, because low-energy X-rays below 20 keV are mainly used and these X-rays are easily absorbed in the sample. However, one physical fact is that, the penetration power of X-ray is proportional to the cubic of its photon energy. So far, the high penetration property of high-energy X-rays has led to many powerful techniques, including flaw detection, medical imaging, and baggage inspection. In these techniques, the investigation thickness is frequently centimeters to decimeters, and high-energy X-rays of 100 keV or more can penetrate them to make a transmission image. In a similar way, high-energy primary X-rays can also penetrate thick soils, reaching a depth of several to tens of centimeters. Meanwhile, K-shell electrons of heavy metals can be excited by the high-energy primary X-rays, and the emitted K-line XRF have high energy so that they can escape from thick soils as well. Consequently, high-energy K-line XRF analysis can be applied to detecting heavy metals buried under ground. The detection depth is much larger than common analysis depth in routine laboratory experiments. This kind of application is rarely mentioned before. In this chapter, we will examine its feasibility and figure out possible achievements in the future.

Searching underground heavy metals by high-energy X-rays should be performed by a self-driving robot to make the search work safe, efficient, and laborsaving. The robot should be powered by a battery pack. It should carry all instruments, including a CPU, a GPS, a wireless communication system, a self-driving system, and most important, a high-voltage X-ray tube as well as an XRF detector. A conceptional figure is shown in Figure 6-1.

In this work, the primary concern is the maximum detectable depth. This parameter can be roughly estimated by equations in X-ray physics. However, to make it convincible, and to fully include the influence of instrument specifications and soil compositions, the maximum detectable depth should be examined directly in experiments. In this chapter, underground survey of a gold coin is taken as an example. The maximum detectable depth in different soils are tested. Efficient data processing methods are discussed.

In the experiment, the survey target is a Vienna Philharmonic Gold Coin of 25 euros. The gold fraction inside is larger than 99.99%. Its diameter is 22 mm and its thickness is 1.2 mm. A CdTe detector (X123 from Amptek) was is used for recording XRF spectra. Its active sensor area is 25 mm$^2$ and its sensor thickness is 1 mm. Primary X-rays come from a laboratory X-ray tube with a tungsten target. The X-ray tube working power is 140 kV – 0.5 mA, only 70 watt, making it applicable to mobile setups. The focusing point in the X-ray tube is 420 mm away from soil surface. The circular beam size at soil surface is 13 mm in dia. Three types of soils are collected to test the corresponding maximum detectable depth (MDD) of the gold coin. Details are given in Table 6-1.

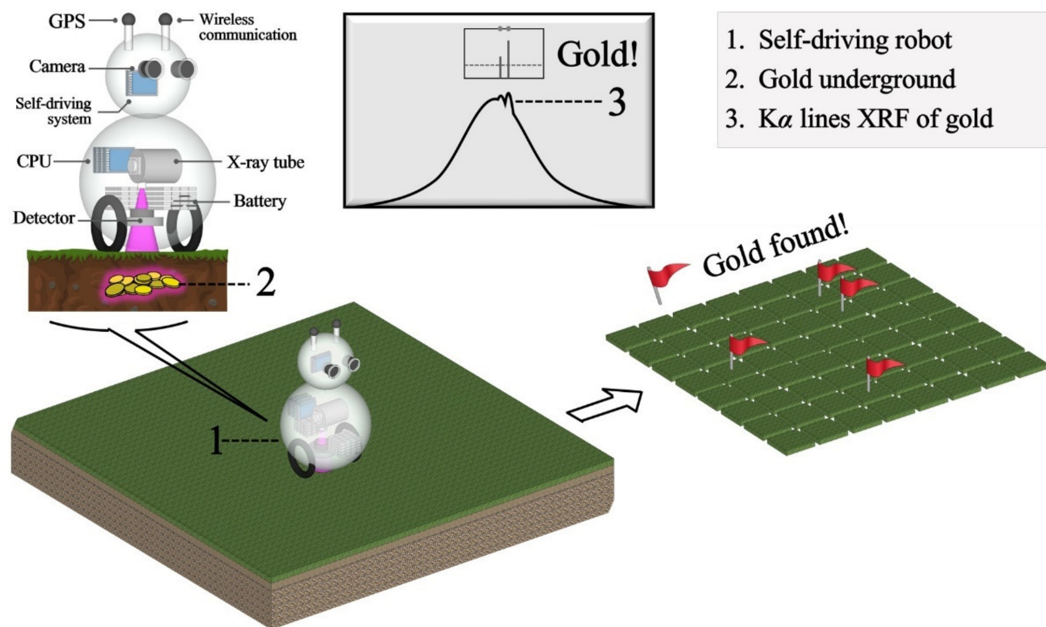


Figure 6-1. Conceptual figure of a self-driving high-energy XRF analyzer robot for underground gold survey

Table 6.1. Maximum detectable depth of different soils.

| # | Composition | Density | MDD |
|---|---|---|---|
| Soil A | Kanuma soil | 0.61 g/cm$^3$ | 19 cm |
| Soil B | Magnetism lime and | 1.60 g/cm$^3$ | 7.5 cm |
| Soil C | Soils from Matsumi Park, Tsukuba, Japan | 0.92 g/cm$^3$ | 10 cm |

Because of the high penetration power of high-energy X-rays, the gold coin buried at a shallow depth can be easily detected. Figure 6-2 shows the acquired XRF spectra of the gold coin buried at 6 cm depth in Soil C. Although the spectra have a strong background of scattering X-rays from soils, sill Au K$\alpha_1$ and K$\alpha_2$ lines can be clearly recognized.

However, when the gold coin is buried even deeper, the detected XRF intensity becomes very weak. For example, Figure 6-3(a) shows the XRF spectra without and with the gold coin buried at 10 cm depth in Soil C. Effective XRF signals are highlighted. Clearly, the gold coin makes only a small difference to the major appearance of the XRF spectra, thus the gold coin deeply buried is easily omitted.

For this reason, we use continuous wavelet transform (CWT) to process the acquired XRF spectra. Result is shown in the lower part in Figure 6-3(b). An envelope method is applied to get instantaneous amplitudes of the oscillations in the CWT result. The upper part in Figure 6-3(b) shows the obtained instantaneous amplitudes. The amplitudes at the Au K$\alpha_1$ and K$\alpha_2$ line positions, in comparison to the threshold, tell the result of detection of the gold coin. In this way, the MDDs in different soils are determined, as shown in Table 6-1. The MDD of 10 cm in Soil C represents the expected performance in most soil matrixes.

In recent years, handheld XRF spectrometers have become increasingly popular. Using them, people can do composition analysis at the original site of samples rather than bringing all samples back to lab. Therefore, sample screening and field survey become much efficient. In a similar way, searching for underground heavy metals should be performed by mobile X-ray setups as well. However, for most commercially-available handheld XRF spectrometers, their X-ray energy is below 40 keV. This is not high enough for underground survey, thus new setups are needed. On the other hand, because of the high

penetration power of high-energy X-rays, thick lead covers should be used to prevent radiation damage, and therefore high-energy XRF setups should be carried by a self-driving robot rather than manual handheld. In a practical application, the working field should be restricted to entrance at five meters away from the surveying point with a clear sign.

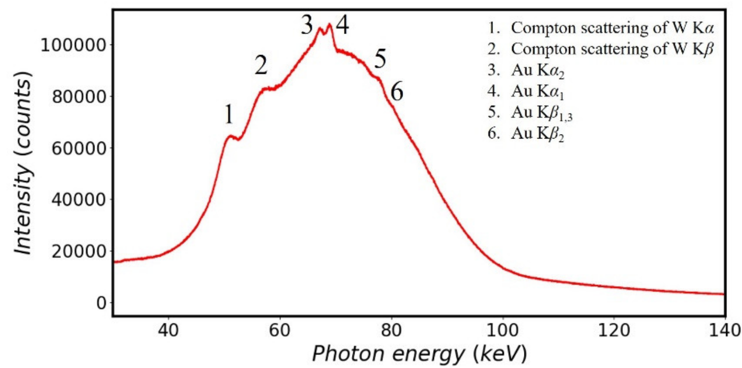


Figure 6-2. XRF spectra of the gold coin buried at 6 cm depth in Soil C

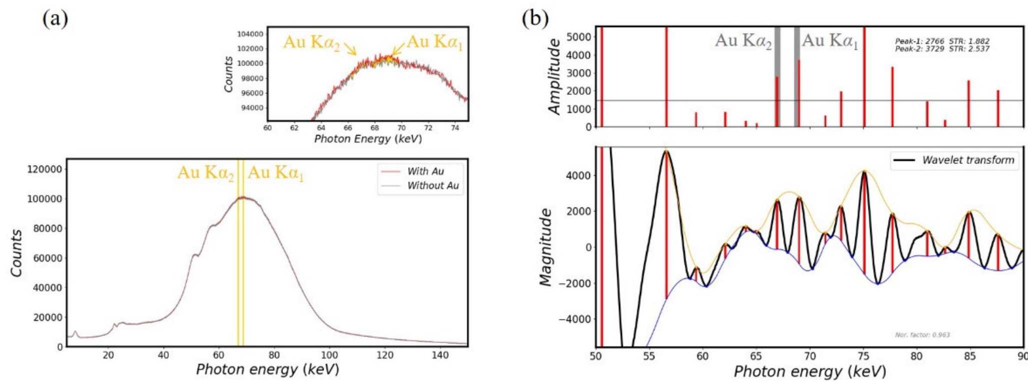


Figure 6-3. XRF spectra of the gold coin buried at 10 cm in Soil C (a) and the corresponding CWT processing results (b).

To sum up, in this chapter, the method of using high-energy XRF analysis for underground survey of heavy metals is proposed. It has been experimentally confirmed that a gold coin buried at a depth of a few centimeters can be easily detected. This technique will be quite helpful in geological, environmental, civil engineering and many other applications. Although its exploration scope is not as broad as present underground survey technologies, it is still a promising supplement because of its accuracy in identifying elements in heavy metals.

## 7. Summary

In many fields, techniques which can visualize spatial distribution, diffusion process, and interface inhomogeneity of chemical elements are of great importance. On the other hand, XRF has been a well-established technique for element identification and composition analysis. In addition to this, XRF imaging can reveal the spatial distribution of chemical elements, which is crucial for the understanding of inhomogeneous systems. Full-field XRF imaging is an efficient scheme: It utilizes a wide beam to illuminate a large field on the sample, an optical component to guide fluorescence X-rays, and a 2D X-ray energy-dispersive detector to capture colorful XRF images. As it adopts a stationary scheme measurement and is free of point-by-point microbeam positional scan, "scanning" or recording other parameters like elapsed time and incident angle during image acquisition becomes much easier. In this way, the elemental imaging can be endowed with additional sensitivities like temporal evolution and surface/interface characterization. New functions like X-ray movie imaging or X-ray interface imaging can be obtained.

In this work, I developed new methods to establish the use of commercially-available visible-light cameras as powerful 2D energy-dispersive X-ray detectors for full-field XRF imaging. Compared with existing highly sophisticated and costly detectors, advantages of the cameras include not only low cost but also large number of pixels and small pixel size. The use of a micro pinhole and a collimator plate in energy-dispersive XRF imaging experiments was also established. In this way, full-field XRF imaging technique became much cost-effective, while a high spatial resolution was available with using laboratory X-ray sources.

Visualizing the spatial distribution of trace elements and knowing their corresponding chemical states are of great importance in many fields. To obtain clear images and to make the chemical state analysis reliable, it is necessary to reduce the detected strong scattering background X-rays from the sample matrix in the measurement of weak XRF signals from the target trace elements. For this reason, linearly polarized synchrotron X-rays was used. To ensure a large viewing area in full-field imaging experiments, an asymmetric-cut crystal was utilized to expend the synchrotron beam in the direction perpendicular to polarization. In the final, XRF images with high signal-to-background ratio were obtained. The setup is possible to be extended further for full-field chemical-state imaging of trace elements.

Multi-element XRF movie imaging was developed to record the entire process of chemical diffusion in changeable samples, as the chemical diffusion process may relate to the nature of chemical reaction, materials formation, segregation/aggregation of particles, and even important physiology activities. The movie imaging was realized by taking a series of XRF images quickly and connecting all images into one continuous movie. On this basis, *in-operando* analysis became available as well. So far, two successful applications have been made. One was the observation of gradual diffusion of calcium and iron in a chemical garden reaction, and the other was for the rapid growth of zinc dendrites during electrodeposition. These two experiments have certainly verified the feasibility of seeing reactions in aqueous systems by multi-element XRF movie imaging.

While full-field XRF imaging provides 2D images which reflect the XY distribution of chemical elements, the technique itself has no sensitivity to the buried depth or Z distribution of the elements. However, in many nanolayers, it is essential to clarify the respective chemical distribution at different depths, especially at functional interfaces. On the other hand, X-ray standing wave analysis can probe the depth profile of elements in nanolayers, however, the technique has no imaging capability and the measurement neglects the inhomogeneity in XY plane. In order to visualize the inhomogeneity at buried functional interfaces and to understand the structure-property of nanolayer materials, we combined these two techniques into a new one: X-ray standing wave imaging. So far, one successful application has been made. Three-dimensional distribution of iron impurities in a nickel (thickness 1.4 nm) / carbon (thickness 3.6 nm) periodic multilayer specimen was investigated. The in-plane spatial resolution was about 160 μm; the depth resolution reached atomic scale, which was better than 1 nm and greatly sensitive to buried interfaces in the present materials system. In the future, the technique is possible to be applied to investigate defect patterns in wafer-scale Langmuir-Blodgett films and 2D materials.

To sum up, techniques of multi-functional full-field XRF imaging have been successfully developed. X-ray elemental imaging could be realized with using cost-effective instruments. For the sake of trace element analysis and imaging, the signal-to-background ratio could be significantly improved with using a size-expanded polarized synchrotron beam. Full process of chemical diffusion in aqueous systems could be

recorded by multi-element XRF movie imaging. Inhomogeneity at buried functional interfaces of nanolayers could be visualized by X-ray standing wave imaging. At present, the techniques are at the starting stage to meet practical scientific applications. In the future, much efforts are still needed to improve the techniques further to meet more real-world needs.

## References

[1] W. Zhao and K. Sakurai, Sci. Rep. **7**, 45472 (2017).

[2] W. Zhao and K. Sakurai, Rev. Sci. Instrum. **88**, 063703 (2017).

[3] B. Henrich, A. Bergamaschi, C. Broennimann, R. Dinapoli, E.F. Eikenberry, I. Johnson, M. Kobas, P. Kraft, A. Mozzanica, and B. Schmitt, Nucl. Instruments Methods Phys. Res. A **607**, 247 (2009).

[4] R. Dinapoli, A. Bergamaschi, B. Henrich, R. Horisberger, I. Johnson, A. Mozzanica, E. Schmid, B. Schmitt, A. Schreiber, X. Shi, and G. Theidel, Nucl. Instruments Methods Phys. Res. A **650**, 79 (2011).

[5] A. Bergamaschi, A. Cervellino, R. Dinapoli, F. Gozzo, B. Henrich, I. Johnson, P. Kraft, A. Mozzanica, B. Schmitt, and X. Shi, J. Synchrotron Radiat. **17**, 653 (2010).

[6] R. Ballabriga, M. Campbell, E.H.M. Heijne, X. Llopart, and L. Tlustos, IEEE Trans. Nucl. Sci. **54**, 1824 (2007).

[7] O. Scharf, S. Ihle, I. Ordavo, V. Arkadiev, A. Bjeoumikhov, S. Bjeoumikhova, G. Buzanich, R. Gubzhokov, A. Günther, R. Hartmann, M. Kühbacher, M. Lang, N. Langhoff, A. Liebel, M. Radtke, U. Reinholz, H. Riesemeier, H. Soltau, L. Strüder, A.F. Thünemann, and R. Wedell, Anal. Chem. **83**, 2532 (2011).

[8] F.P. Romano, C. Caliri, L. Cosentino, S. Gammino, L. Giuntini, D. Mascali, L. Neri, L. Pappalardo, F. Rizzo, F. Taccetti, U. Catania, and V.A. Doria, Anal. Chem. **86**, 10892 (2014).

[9] F.P. Romano, C. Caliri, L. Cosentino, S. Gammino, D. Mascali, L. Pappalardo, F. Rizzo, O. Scharf, and H.C. Santos, Anal. Chem. **88**, 9873 (2016).

[10] H. Tsunemi, J. Hiraga, K. Yoshita, E. Miyata, and M. Ohtani, Nucl. Instruments Methods Phys. Res. Sect. A Accel. Spectrometers, Detect. Assoc. Equip. **439**, 592 (2000).

[11] R.E. Griffiths, G. Polucci, A. Mak, S.S. Murray, and D.A. Schwartz, in *Solid State Imagers Astron.* (1981), pp. 62–69.

[12] L. Strüder, P. Holl, G. Lutz, and J. Kemmer, Nucl. Instruments Methods Phys. Res. Sect. A Accel. Spectrometers, Detect. Assoc. Equip. **257**, 594 (1987).

[13] L. Strüder, U. Briel, K. Dennerl, R. Hartmann, E. Kendziorra, N. Meidinger, E. Pfeffermann, C. Reppin, B. Aschenbach, and W. Bornemann, Astron. Astrophys. **365**, L18 (2001).

[14] D.H. Lumb, Nucl. Inst. Methods Phys. Res. A **290**, 559 (1990).

[15] H. Tsunemi, M. Wada, K. Hayashida, and S. Kwai, Jpn. J. Appl. Phys. **30**, 3540 (1991).

[16] L. Labate, A. Giulietti, D. Giulietti, P. Köster, T. Levato, L.A. Gizzi, F. Zamponi, A. Lübcke, T. Kämpfer, I. Uschmann, and E. Förster, Rev. Sci. Instrum. **78**, 103506 (2007).

[17] M.G. Vasin, Y. V. Ignatiev, A.E. Lakhtikov, A.P. Morovov, and V. V. Nazarov, Spectrochim. Acta - Part B At. Spectrosc. **62**, 648 (2007).

[18] J.G. Rocha, N.F. Ramos, S. Lanceros-Mendez, R.F. Wolffenbuttel, and J.H. Correia, Sensors Actuators, A Phys. **110**, 119 (2004).

[19] R. Mokso, F. Marone, S. Irvine, M. Nyvlt, D. Schwyn, K. Mader, G.K. Taylor, H.G. Krapp, M. Skeren, and M. Stampanoni, J. Phys. D. Appl. Phys. **46**, 494004 (2013).

[20] C. Hall, D. Hausermann, A. Maksimenko, A. Astolfo, K. Siu, J. Pearson, and A. Stevenson, J. Instrum. **8**, C06011 (2013).

[21] I. V. Zenyuk, D.Y. Parkinson, G. Hwang, and A.Z. Weber, Electrochem. Commun. **53**, 24 (2015).

[22] B. Fowler, C. Liu, S. Mims, J. Balicki, W. Li, H. Do, J. Appelbaum, and P. Vu, Proc. SPIE **7536**, 753607 (2010).

[23] D.H. Lumb and A.D. Holland, Nucl. Inst. Methods Phys. Res. A **273**, 696 (1988).

[24] F. Huang, T.M.P. Hartwich, F.E. Rivera-Molina, Y. Lin, W.C. Duim, J.J. Long, P.D. Uchil, J.R. Myers, M. a Baird, W. Mothes, M.W. Davidson, D. Toomre, and J. Bewersdorf, Nat. Methods **10**, 653 (2013).

[25] H. Tsunemi, K. Mizukata, and M. Hiramatsu, Jpn. J. Appl. Phys. **27**, 670 (1988).

[26] L. Strüder, H. Bräuninger, M. Meier, P. Predehl, C. Reppin, M. Sterzik, J. Trümper, P. Cattaneo, D. Hauff, K.F. Schuster, E. Kenziorra, A. Staubert, E. Gatti, M. Sampietro, V. Radeka, P. Rehak, S. Rescia, P.F. Manfredi, W. Buttler, P. Holl, J. Kemmer, U. Prechtel, T. Ziemann, J. Kemmer, U. Prechtel, and T. Ziemann, Nucl. Instruments Methods Phys. Res. Sect. A Accel. Spectrometers, Detect. Assoc. Equip. **288**, 227 (1990).

[27] E. Pinotti, H. Bräuninger, N. Findeis, H. Gorke, D. Hauff, P. Holl, J. Kemmer, P. Lechner, G. Lutz, W. Kink, N. Meidinger, G. Metzner, P. Predehl, C. Reppin, L. Strüder, J. Trümper, C. v. Zanthier, E. Kendziorra, R. Staubert, V. Radeka, P. Rehak, G. Bertuccio, E. Gatti, A. Longoni, A. Pullia, and M. Sampietro, Nucl. Instruments Methods Phys. Res. Sect. A Accel. Spectrometers, Detect. Assoc. Equip. **326**, 85 (1993).

[28] R.E. Griffiths, G. Polucci, A. Mak, S.S. Murray, and D.A. Schwartz, Proc. SPIE **244**, 57 (1981).

[29] D.H. Lumb, Nucl. Instruments Methods Phys. Res. Sect. A Accel. Spectrometers, Detect. Assoc. Equip. **288**, 219 (1990).

[30] H. Tsunemi, K. Mizukata, and M. Hiramatsu, Jpn. J. Appl. Phys. **27**, 670 (1988).

[31] H. Tsunemi, M. Wada, H. Tsunemi, J. Hiraga, C. Device, N. Tawa, K. Ikegami, J. Hiraga, H. Tsunemi, M. Lesser, H. Tsunemi, K. Yoshita, and S. Kitamoto, Jpn. J. Appl. Phys. **30**, 1299 (1991).

[32] K. Okamoto and K. Fuwa, Anal. Sci. **1**, 206 (1985).

[33] W. Zhao and K. Sakurai, J. Synchrotron Radiat. **26**, 230 (2019).

[34] M. Young, Appl. Opt. **10**, 2763 (1971).

[35] W. Zhao, K. Hirano, and K. Sakurai, J. Anal. At. Spectrom. **34**, 2273 (2019).

[36] K. Sakurai, Spectrochim. Acta, Part B At. Spectrosc. **54**, 1497 (1999).

[37] K. Sakurai and H. Eba, Anal. Chem. **75**, 355 (2003).

[38] K. Sakurai and M. Mizusawa, Anal. Chem. **82**, 3519 (2010).

[39] M. Mizusawa and K. Sakurai, J. Synchrotron Radiat. **11**, 209 (2004).

[40] H. Eba, H. Ooyama, and K. Sakurai, J. Anal. At. Spectrom. **31**, 1105 (2016).

[41] S. Matsuyama, Y. Emi, H. Kino, Y. Kohmura, M. Yabashi, T. Ishikawa, and K. Yamauchi, Opt. Express **23**, 9746 (2015).

[42] S. Matsuyama, J. Yamada, Y. Kohmura, M. Yabashi, T. Ishikawa, and K. Yamauchi, Opt. Express **27**, 18318 (2019).

[43] N. Watanabe, K. Yamamoto, H. Takano, T. Ohigashi, H. Yokosuka, T. Aota, and S. Aoki, Nucl. Instruments Methods Phys. Res. Sect. A Accel. Spectrometers, Detect. Assoc. Equip. **467–468**, 837 (2001).

[44] T. Ohigashi, N. Watanabe, H. Yokosuka, T. Aota, H. Takano, A. Takeuchi, and S. Aoki, J. Synchrotron Radiat. **9**, 128 (2002).

[45] K. Sakurai and X. Guo, Spectrochim. Acta Part B At. Spectrosc. **54**, 99 (1999).

[46] W. Zhao, K. Hirano, and K. Sakurai, Rev. Sci. Instrum. **90**, 113704 (2019).

[47] T.G. Dzubay, B. V. Jarrett, and J.M. Jaklevic, Nucl. Instruments Methods **115**, 297 (1974).

[48] L. Wielopolski, J.F. Rosen, D.N. Slatkin, R. Zhang, J.A. Kalef-Ezra, J.C. Rothman, M. Maryanski, and S.T. Jenks, Med. Phys. **16**, 521 (1989).

[49] A. Iida, K. Sakurai, T. Matsushita, and Y. Gohshi, Nucl. Inst. Methods Phys. Res. A **228**, 556 (1985).

[50] K. SAKURAI, A. IIDA, and Y. GOHSHI, Anal. Sci. **4**, 3 (2007).

[51] H. Aiginger, P. Wobrauschek, and C. Brauner, Nucl. Instruments Methods **120**, 541 (1974).

[52] P. Wobrauschek and H. Aiginger, X-Ray Spectrom. **12**, 72 (1983).

[53] W. Soller, Phys. Rev. **24**, 158 (1924).

[54] K. Huke and T. Yamakawa, Nucl. Instruments Methods **177**, 253 (1980).

[55] O.F. Beamline, P.F. Vertical, and I.T.S. Operation, Nucl. Instruments Methods Phys. Res. Sect. A Accel. Spectrometers, Detect. Assoc. Equip. **246**, 144 (1986).

[56] J. Goulon, P. Elleaume, and D. Raoux, Nucl. Instruments Methods Phys. Res. Sect. A Accel. Spectrometers, Detect. Assoc. Equip. **254**, 192 (1987).

[57] P. Elleaume, J. Synchrotron Radiat. **1**, 19 (1994).

[58] T. Hara, T. Tanaka, T. Tanabe, X.-M. Marechal, K. Kumagai, and H. Kitamura, J. Synchrotron Radiat. **5**, 426 (1998).

[59] D.M. Mills, Nucl. Instruments Methods Phys. Res. Sect. A Accel. Spectrometers, Detect. Assoc. Equip. **266**, 531 (1988).

[60] D. Laundy, Nucl. Inst. Methods Phys. Res. A **290**, 248 (1990).

[61] I.O. Olabanji, E.A. Oluyemi, and E.I. Obianjuwa, J. Environ. Chem. Ecotoxicol. **7**, 1 (2015).

[62] K. NAKANO, T. NAKAMURA, I. NAKAI, A. KAWASE, M. IMAI, M. HASEGAWA, Y. ISHIBASHI, I. INAMOTO, K. SUDOU, M. KOZAKI, A. TURUTA, H. HONMA, A. ONO, K. KAKITA, and M. SAKATA, Bunseki Kagaku **55**, 501 (2006).

[63] L. Vincze, K. Janssens, F. Adams, M.L. Rivers, and K.W. Jones, Spectrochim. Acta Part B At. Spectrosc. **50**, 127 (1995).

[64] J.H. Hubbell, W.J. Veigele, E.A. Briggs, R.T. Brown, D.T. Cromer, and R.J. Howerton, J. Phys. Chem. Ref. Data **4**, 471 (1975).

[65] T. Schoonjans, V.A. Solé, L. Vincze, M. Sanchez Del Rio, K. Appel, and C. Ferrero, Spectrochim. Acta - Part B At. Spectrosc. **82**, 36 (2013).

[66] J.M. Jaklevic, R.D. Giauque, and A.C. Thompson, Nucl. Inst. Methods Phys. Res. B **10**–**11**, 303 (1985).

[67] B. Wei and L. Yang, Microchem. J. **94**, 99 (2010).

[68] F. Zeng, W. Wei, M. Li, R. Huang, F. Yang, and Y. Duan, Int. J. Environ. Res. Public Health **12**, 15584 (2015).

[69] P.N. Williams, M. Lei, G. Sun, Q. Huang, Y. Lu, C. Deacon, A.A. Meharg, and Y.-G. Zhu, Environ. Sci. Technol. **43**, 637 (2009).

[70] P. Sivaperumal, T. V Sankar, and P.G.V. Nair, Food Chem. **102**, 612 (2007).

[71] H. Tanida, H. Yamashige, Y. Orikasa, M. Oishi, Y. Takanashi, T. Fujimoto, K. Sato, D. Takamatsu, H. Murayama, H. Arai, E. Matsubara, Y. Uchimoto, and Z. Ogumi, J. Synchrotron Radiat. **18**, 919 (2011).

[72] M. Katayama, K. Sumiwaka, R. Miyahara, H. Yamashige, H. Arai, Y. Uchimoto, T. Ohta, Y. Inada, and Z. Ogumi, J. Power Sources **269**, 994 (2014).

[73] W. Bras, B. Laforce, S. Bauters, J. Garrevoet, L. Vincze, D. Banerjee, E. Van Ranst, A. Longo, B. Vekemans, and P. Tack, Anal. Chem. **86**, 8791 (2014).

[74] W. Zhao and K. Sakurai, ACS Omega **2**, 4363 (2017).

[75] M. Traube, Arch. Anat. Physiol. Wiss. Med **87**, 129 (1867).

[76] R.D. Coatman, N.L. Thomas, and D.D. Double, J. Mater. Sci. **15**, 2017 (1980).

[77] L.M. Barge, S.S.S. Cardoso, J.H.E. Cartwright, G.J.T. Cooper, L. Cronin, A. De Wit, I.J. Doloboff, B. Escribano, R.E. Goldstein, F. Haudin, D.E.H. Jones, A.L. Mackay, J. Maselko, J.J. Pagano, J. Pantaleone, M.J. Russell, C.I. Sainz-Diaz, O. Steinbock, D.A. Stone, Y. Tanimoto, and N.L. Thomas, Chem. Rev. **115**, 8652 (2015).

[78] J.H.E. Cartwright, J.M. García-Ruiz, M.L. Novella, and F. Otálora, J. Colloid Interface Sci. **256**, 351 (2002).

[79] J.H.E. Cartwright, B. Escribano, and C.I. Sainz-Díaz, Langmuir **27**, 3286 (2011).

[80] S. Thouvenel-Romans and O. Steinbock, J. Am. Chem. Soc. **125**, 4338 (2003).

[81] J. Pantaleone, A. Toth, D. Horvath, J. Rother McMahan, R. Smith, D. Butki, J. Braden, E. Mathews, H. Geri, and J. Maselko, Phys. Rev. E - Stat. Nonlinear, Soft Matter Phys. **77**, 1 (2008).

[82] V. Kaminker, J. Maselko, and J. Pantaleone, J. Chem. Phys. **137**, 184701 (2012).

[83] B.C. Batista, P. Cruz, and O. Steinbock, Langmuir **30**, 9123 (2014).

[84] C. Collins, W. Zhou, A.L. Mackay, and J. Klinowski, Chem. Phys. Lett. **286**, 88 (1998).

[85] D. Balköse, F. Özkan, U. Köktürk, S. Ulutan, S. Ülkü, and G. Nişli, J. Sol-Gel Sci. Technol. **23**, 253 (2002).

[86] K. Parmar, H.T. Chaturvedi, M.W. Akhtar, S. Chakravarty, S.K. Das, A. Pramanik, M. Ghosh, A.K. Panda, N. Bandyopadhya, and S. Bhattacharjee, Mater. Charact. **60**, 863 (2009).

[87] L.M. Barge, I.J. Doloboff, L.M. White, G.D. Stucky, M.J. Russell, and I. Kanik, Langmuir **28**, 3714 (2012).

[88] C. Collins, W. Zhou, and J. Klinowski, Chem. Phys. Lett. **306**, 145 (1999).

[89] C. Collins, G. Mann, E. Hoppe, T. Duggal, T.L. Barr, and J. Klinowski, Phys. Chem. Chem. Phys. **1**, 3685 (1999).

[90] C. Collins, R. Mokaya, and J. Klinowski, Phys. Chem. Chem. Phys. **1**, 4669 (1999).

[91] D. Jones and U. Walter, J. Colloid Interface Sci. **203**, 286 (1998).

[92] J.H.E. Cartwright, B. Escribano, C.I. Sainz-Díaz, and L.S. Stodieck, Langmuir **27**, 3294 (2011).

[93] I. Uechi, A. Katsuki, L. Dunin-Barkovskiy, and Y. Tanimoto, J. Phys. Chem. B **108**, 2527 (2004).

[94] W. Duan, S. Kitamura, I. Uechi, A. Katsuki, and Y. Tanimoto, J. Phys. Chem. B **109**, 13445 (2005).

[95] M.J. Russell and A.J. Hall, J. Geol. Soc. **154**, 377 (1997).

[96] J.D. Birchall, a. J. Howard, and J.E. Bailey, Proc. R. Soc. A Math. Phys. Eng. Sci. **360**, 445 (1978).

[97] G. Butler and H.C.K. Ison, Nature **182**, 1229 (1958).

[98] R. Daly, O. Kotova, M. Boese, T. Gunnlaugsson, and J.J. Boland, ACS Nano **7**, 4838 (2013).

[99] L.M. Barge, Y. Abedian, M.J. Russell, I.J. Doloboff, J.H.E. Cartwright, R.D. Kidd, and I. Kanik, Angew. Chemie - Int. Ed. **54**, 8184 (2015).

[100] K. Punia, M. Bucaro, A. Mancuso, C. Cuttitta, A. Marsillo, A. Bykov, W. L'Amoreaux, and K.S. Raja, Langmuir **32**, 8748 (2016).

[101] S.S.S. Cardoso, J.H.E. Cartwright, A.G. Checa, and C.I. Sainz-Díaz, Acta Biomater. **43**, 338 (2016).

[102] F. Haudin, J.H.E. Cartwright, and A. De Wit, J. Phys. Chem. C **119**, 15067 (2015).

[103] F. Haudin, V. Brasiliense, J.H.E. Cartwright, F. Brau, and A. De Wit, Phys. Chem. Chem. Phys. **17**, 12804 (2015).

[104] W. Zhao and K. Sakurai, Phys. Rev. Mater. **3**, 023802 (2019).

[105] J. Zegenhagen and A. Kazimirov, *The X-Ray Standing Wave Technique: Principles and Applications* (World Scientific, Hackensack, NJ, 2013).

[106] B.W. Batterman, Phys. Rev. **133**, A759 (1964).

[107] B.W. Batterman, Phys. Rev. Lett. **22**, 703 (1969).

[108] P.L. Cowan, J.A. Golovchenko, and M.F. Robbins, Phys. Rev. Lett. **44**, 1680 (1980).

[109] J. Golovchenko, J. Patel, D. Kaplan, P. Cowan, and M. Bedzyk, Phys. Rev. Lett. **49**, 560 (1982).

[110] T.W. Barbee and W.K. Warburton, Mater. Lett. **3**, 17 (1984).

[111] D.K.G. De Boer, Phys. Rev. B **44**, 498 (1991).

[112] M. Bedzyk, D. Bilderback, G. Bommarito, M. Caffrey, and J. Schildkraut, Science **241**, 1788 (1988).

[113] M.J. Bedzyk, G.M. Bommarito, and J.S. Schildkraut, Phys. Rev. Lett. **62**, 1376 (1989).

[114] M. Bedzyk, G. Bommarito, M. Caffrey, and T. Penner, Science **248**, 52 (1990).

[115] P. Fenter, L. Cheng, S. Rihs, M. MacHesky, M.J. Bedzyk, and N.C. Sturchio, J. Colloid Interface Sci. **225**, 154 (2000).

[116] J.M. Bloch, M. Sansone, F. Rondelez, D.G. Peiffer, P. Pincus, M.W. Kim, and P.M. Eisenberger, Phys. Rev. Lett. **54**, 1039 (1985).

[117] N. Hertel, G. Materlik, and J. Zegenhagen, Z Phys B - Condens. Matter **204**, 199 (1985).

[118] J. Zegenhagen, Surf. Sci. Rep. **18**, 202 (1993).

[119] L.G. Parratt, Phys. Rev. **95**, 359 (1954).

[120] J. Jiang, K. Hirano, and K. Sakurai, J. Appl. Crystallogr. **50**, 712 (2017).

[121] S. Annaka, S. Kikuta, and K. Kohra, J. Phys. Soc. Japan **21**, 1559 (1966).

[122] W. Scḧlke, U. Bonse, and S. Mourikis, Phys. Rev. Lett. **47**, 1209 (1981).

[123] J.A. Golovchenko, D.R. Kaplan, B. Kincaid, R. Levesque, A. Meixner, M.F. Robbins, and J. Felsteiner, Phys. Rev. Lett. **46**, 1454 (1981).

[124] J.S. Okasinski, C.Y. Kim, D.A. Walko, and M.J. Bedzyk, Phys. Rev. B **69**, 041401 (2004).

[125] A.A. Escuadro, D.M. Goodner, J.S. Okasinski, and M.J. Bedzyk, Phys. Rev. B **70**, 235416 (2004).

[126] E. Schneck and B. Demé, Curr. Opin. Colloid Interface Sci. **20**, 244 (2015).

[127] T.T. Fister, J. Esbenshade, X. Chen, B.R. Long, B. Shi, C.M. Schlepütz, A.A. Gewirth, M.J. Bedzyk, and P. Fenter, Adv. Energy Mater. **4**, 1 (2014).

[128] G. Evmenenko, T.T. Fister, D.B. Buchholz, Q. Li, K. Chen, J. Wu, V.P. Dravid, M.C. Hersam, P. Fenter, and M.J. Bedzyk, ACS Appl. Mater. Interfaces **8**, 19979 (2016).

[129] X. Chen, T.T. Fister, J. Esbenshade, B. Shi, X. Hu, J. Wu, A.A. Gewirth, M.J. Bedzyk, and P. Fenter, ACS Appl. Mater. Interfaces **9**, 8169 (2017).

[130] G. Evmenenko, T.T. Fister, D.B. Buchholz, F.C. Castro, Q. Li, J. Wu, V.P. Dravid, P. Fenter, and M.J. Bedzyk, Phys. Chem. Chem. Phys. **19**, 20029 (2017).

[131] J.A. Zasadzinski, R. Viswanathan, L. Madsen, J. Garnae, and D.K. Schwartz, Science **263**, 1726 (1994).

[132] X. Luo, Z. Zhang, and Y. Liang, Langmuir **10**, 3213 (1994).

## List of publications


1. Zhao, W.; Sakurai, K. Multi-Element X-Ray Movie Imaging with a Visible-Light CMOS Camera. *J. Synchrotron Radiat*. 2019, 26 (1), 230–233. https://doi.org/10.1107/S1600577518014273

2. Zhao, W.; Sakurai, K. X-Ray Standing Wave Technique with Spatial Resolution: In-Plane Characterization of Surfaces and Interfaces by Full-Field x-Ray Fluorescence Imaging. *Phys. Rev. Mater.* 2019, 3 (2), 23802. https://doi.org/10.1103/PhysRevMaterials.3.023802

3. Zhao, W.; Hirano, K.; Sakurai, K. Antiscattering X-Ray Fluorescence Analysis for Large-Area Samples. *J. Anal. At. Spectrom.* 2019, 34 (11), 2273–2279. https://doi.org/10.1039/C9JA00220K

4. Zhao, W.; Hirano, K.; Sakurai, K. Expanding a Polarized Synchrotron Beam for Full-Field x-Ray Fluorescence Imaging. *Rev. Sci. Instrum.* 2019, 90 (11), 113704. https://doi.org/10.1063/1.5115421

5. Zhao, W.; Sakurai, K. Realtime Observation of Diffusing Elements in a Chemical Garden. *ACS Omega* 2017, 2 (8), 4363–4369. https://doi.org/10.1021/acsomega.7b00930

6. Zhao, W.; Sakurai, K. Seeing Elements by Visible-Light Digital Camera. *Sci. Rep.* 2017, 7 (1), 45472. https://doi.org/10.1038/srep45472

7. Zhao, W.; Sakurai, K. CCD Camera as Feasible Large-Area-Size x-Ray Detector for x-Ray Fluorescence Spectroscopy and Imaging. *Rev. Sci. Instrum.* 2017, 88 (6), 63703. https://doi.org/10.1063/1.4985149

## Acknowledgements

I want to express my gratitude to my supervisor Professor Kenji Sakurai. In these five years, including doctoral courses and pre-doctoral courses, I learnt a lot from him. It is not only about the knowledge in X-ray physics and materials science, or the skills in writing and making presentations, or the strategy of organizing research project, but also about his active attitude towards work. I believe I will never forget his slogans throughout my academic career.

I also want to acknowledge Professor Keiichi Hirano from Photon Factory, KEK. In the past three years, I visited his beamtimes many times for experiments and there I received his kind help. His work of manipulating and expanding a synchrotron beam contributed an important part in Chapter 3. Thanks to his help, my work went fluently.

I want to thank Ms. Megumi Iwamoto, who is the fist member I saw when I first came to the lab in 2014. In these five years, she has helped me so much in experiments and in my life in Tsukuba as a foreigner. Current and former members in NIMS X-ray Lab also helped me a lot over years. Thanks to Jinxing Jiang, Dan Li, Yuwei Liu, and Haruya Kobayashi. I want to say it was really an enjoyable experience to work with them.